On-Chip Planar Lens Architectures for Optical Beam Steering

by

Josué Jacob López

B.S., William Marsh Rice University (2014)
S.M., Massachusetts Institute of Technology (2017)

Submitted to the Department of Electrical Engineering and Computer Science
in partial fulfillment of the requirements for the degree of

Doctor of Philosophy in Electrical Engineering and Computer Science

at the

MASSACHUSETTS INSTITUTE OF TECHNOLOGY

May 2022

© Massachusetts Institute of Technology 2022. All rights reserved.

Author .....
Department of Electrical Engineering and Computer Science
May 13, 2022

Certified by .....
Marin Soljačić
Professor of Physics
Thesis Supervisor

Accepted by .....
Leslie A. Kolodziejski
Professor of Electrical Engineering and Computer Science
Chair, Department Committee on Graduate Students

On-Chip Planar Lens Architectures for Optical Beam Steering

by

Josué Jacob López

Submitted to the Department of Electrical Engineering and Computer Science
on May 13, 2022, in partial fulfillment of the
requirements for the degree of
Doctor of Philosophy in Electrical Engineering and Computer Science

Abstract

Free-space optical beam steering is an important technological capability because of its applications in optical communication links and sensing such as light detection and ranging (lidar). Over the past decade, there has been significant efforts to develop a beam steering architecture that can lead to solid-state lidar with lower size, weight, power consumption, and cost (SWaP-C) while still meeting a high level of sensing performance and reliability. Herein, is the experimental demonstration of two novel planar lens-based architectures for optical beam steering in two dimensions. The first experimental demonstration is an aplanatic lens designed via the paraxial ray approximation and ray tracing. The second experimental demonstration is a Luneburg lens that is designed with a gradient in the refractive index along the radius of the lens. This second system uses a circularly symmetric grating to emit the optical beam over a wide field of view. Both planar lens architectures leverage a near-infrared tunable laser, a Mach-Zehnder interferometer switch tree, the lens that collimates and steers an optical mode in-the-plane of the chip, and a wavelength dependent grating for out-of-plane coupling. Various grating designs are presented towards the improvement of the effective aperture length and optical power emitted from the grating including double-layer grating designs and apodization schemes for the grating fill-fraction. Both devices are fabricated using a wafer-scale fabrication process and pave the way for two-dimensional optical beam steering with low electronic complexity and a large field of view. Lastly, remaining architecture challenges for a high performance lidar-on-a-chip system are discussed.

Thesis Supervisor: Marin Soljačić
Title: Professor of Physics

Acknowledgments

This Ph.D. is dedicated to my family who has provided me with love and support my entire life and who has cheered me on as I pursued the highest levels of intellectual and personal growth at MIT over the past eight years. This is especially dedicated in memory of both my Abuelita Julia and Tío Jaime who passed away during my last two years at MIT. My grandmother who passed away in March at the age of 91 was a fiercely independent woman. Even though she may not have understood what I was working on, she always encouraged me and made sure that I was eating, sleeping, and taking care of myself. Her humor, laughter, and love will stay with me all of my life. My Tío Jaime who passed away due to COVID-19 in 2020, showed me what it was like to work hard from dusk to dawn and how to love his family dearly.

To my loving wife, Jessica L. Ruiz-López, M.D., thank you from the bottom of my heart for your support, love, and partnership over the last ten and a half years. I could not ask for a more understanding and loving partner. You inspire me with the great compassion and dedication you have for your pediatric patients. I look to the very long hours you put in to heal and support your patients whenever I have to dig deep and move forward.

To my parents and family: I don't know how my mother did it, but as my brother and I grew up, she worked part time, took care of the family, and after many years of shear determination obtained a bachelor's degree (all while struggling to master English as a second-language after immigrating to the U.S. from Guatemala). She did this to show us the value of education. To my father, who showed my brother and I the value of hard work, precision, and most important of all – integrity. He would have been an excellent engineer had he been offered the same opportunities my brother and I were fortunate to have. To my younger brother Ivan, your intelligence inspires and pushes me, and your humor makes me see the bright side of life. I am also so happy to now have my sister-in-law, Jennifer López, M.D., and my baby nephew Ezra as part of the family. I look forward to all the memories we will have as a family. I will work hard to continue to make you proud.

To my Tia Any, Tío Jaime, my cousins, and all my extended family in Houston, Texas who took me in as one of their own: Thank you! This journey has been so much better with you. To all of my family in Guatemala: Thank you for all of your love and support from afar. I look up to your humility and work ethic.

To my friends and teachers from Lynwood, CA who taught and pushed me to be diligent, not back down, and push farther regardless of our social or economic background (and to always give back once we made it). I am proud to say many of my friends have become leaders in the community. We are making a difference. To my dear friends, mentors, and supporters who I met at UC Berkeley (Pi Lambda Phi), East Los Angeles College (MESA), Rice University, Northwestern University, Caltech, and now MIT. Thank you. There are so many individuals to name here, you have been my family away from home and my support system in this incredible seventeen year journey from UC Berkeley, to ELAC, to Rice, and finally MIT.

MIT Acknowledgments:

First of all, thank you to my advisor, Prof. Marin Soljačić, for your guidance and unwavering support during the past eight years. You have given me the freedom to develop into a fully independent researcher and supported me regardless of the path I chose in science and entrepreneurship. Moreover, thank you to my two additional committee members, Prof. Leslie A. Kolodziejski and Prof. Karl Berggren. Leslie I consider you my academic godmother. You have supported me throughout every stage of my MIT journey. I could not have completed this Ph.D. without your guidance and support. Karl, you were probably the first MIT EECS professor I encountered. I have had the sincere pleasure of taking your nanofabrication work and discussing several of my research projects throughout the years. Additionally, thank you to Prof. John Joannopoulos (JJ), Prof. Terry Orlando, Prof. Vladimir Bulovic, Prof. Edmund Bertschinger, and Prof. Farnaz Niroui. With your combined support, I had the best set of MIT faculty advocates and supporters I could have asked for.

Thank you to Dr. Scott Skirlo, Dr. Cheri Sorace-Agaskar, Mr. Samuel Kim, Mr. Jamison Sloan, Dr. Dave Kharas, Dr. Suraj Bramhavar, and Dr. Thomas

Mahony your technical mentorship and collaboration made the results in this Ph.D. thesis possible. To Mr. Ryan Maxson and Mr. Alex Medeiros, your technical and lab support was key to my day to day success in the lab. To Dr. Jeffrey Herd and Dr. Paul Juodawlkis, thank you for your unwavering support throughout my collaboration with MIT Lincoln Laboratory and Group 89. To Prof. Steven Johnson and Prof. George Barbastathis, thank you for your insights and guidance as the team and I designed the Luneburg lens architecture.

Moreover, it has been an honor to work in the Soljačić Group. I am always in awe of the brilliance of everyone in the group and thankful for your generosity in scientific discussions and collaborations. Thanks to the Organic and Nanostructured Electronics Laboratory (ONE) Lab and all of its members, you have been my second "group" at MIT.

Thank you to my dear MIT friends and community: Rich & Lisa, Erik & Monique, Joe & Rebecca, Navid, and the rest of the MIT EECS Department. Michael & Rachel, Kushal, and the MIT Physics Department. The Academy of Courageous Minority Engineers, Black Graduate Student Association, LatinX Graduate Student Association, and Fossil Free MIT. Thank you to the staff of the University Center for Exemplary Mentorship and the Office of Graduate Education (including Dean Blanche Staton, Gloria Anglon, and Leo Savala). Thank you to the phenomenal MIT entrepreneurship programs and resources I have been able to take part of including the Sandbox Innovation Fund Program, Deshpande Center for Technological Innovation, and Martin Trust Center.

Thank you to my Funding Sources that sponsored by research at MIT including the Activate Entrepreneurial Research Fellowship, Facebook Fellowship in AR/VR Photonics and Optics, Alfred P. Sloan Foundation Graduate UCEM Scholarship, National GEM Consortium Fellowship, National Science Foundation Graduate Research Fellowship, and MIT Lemelson Presidential Graduate Fellowship.

Lastly, there are many more people to thank. Please forgive me if I did not include you. I will make sure to always give you my gratitude in person and in the moment because life is to short not to give gratitude.

Contents

List of Figures

List of Tables

Chapter 1

Introduction

1.1 Introduction to Lidar and Lidar Modalities

Free-space optical beam steering is an important technological capability because of its applications in optical communication links [1], and sensors such as light detection and ranging (lidar) [2, 3]. This is why there has been a significant effort to develop a beam steering architecture with low size, weight, power consumption, and cost (SWaP-C). In particular, the interest in low SWaP-C optical beam steering for lidar is based on its usefulness in enabling autonomous machines and vehicles to navigate the world by providing high resolution and unambiguous ranging and velocity information of surrounding objects in both daytime and nighttime conditions. This type of information is critical since it allows an autonomous system to detect objects of interest and safely navigate around obstacles [4]. More concretely, lidar sensors provide vital information by scanning an optical beam (i.e. laser) within an area of interest, typically in the wavelength range between 850 and 1550 nm, and using the reflected optical signals to build a three-dimensional map containing distance and velocity information, and other properties such as material type based on the interactions of light with the object [3].

1.1.1 Time of Flight Lidar

One of the main modalities used for lidar is Time of Flight (ToF) which is based on incoherent light sources. ToF uses an optical pulse of light, or pulse train, to directly measure the round-trip time needed for a signal to be emitted from the sensor, reflect off a target, and return to the receiver, Fig. 1-1. Since the signal power is proportional to $1/R^2$, where R is the radial distance of the object, the energy required for detection can be an issue [5]. Due to the low amount of returned power, this often requires geiger mode avalanche photodetectors (APDs). Since the precision of the range measurement is determined by the on/off edges of the pulse, high-resolution radial measurements require short nanosecond optical pulses. Therefore, the electronics needed for signal detection operate in the GHz domain [6]. One challenge in using the ToF modality is that high-gain detectors can detect light from any source, therefore they can be susceptible to ambient light, the sun, or other lidar sources [6].

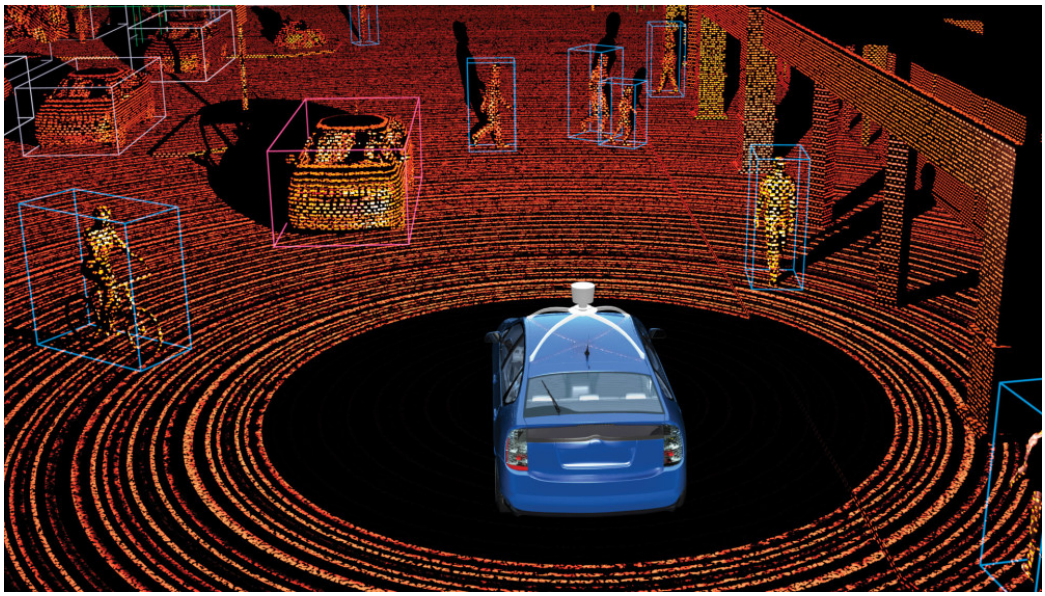

Figure 1-1: Rendered image of autonomous Waymo vehicle navigating an environment with pedestrians, cyclists, and other vehicles. The 3D point cloud is generated by a spinning Veloydne lidar unit. Adapted from original source: Popular Science/Graham Murdoch © 2013.

1.1.2 Frequency-Modulated Continous Wave (FMCW) Lidar

In contrast to ToF which uses an incoherent source, a coherent detection method that is widely used in lidar is frequency-modulated continuous wave (FMCW). FMCW is not only able to measure radial distance but also able to directly measure the velocity of an object via the Doppler effect [3]. One standard scheme uses a triangle-wave frequency modulation that is sampled both on the upward and downward slope of the local oscillator (LO). Since the LO signal and the return signal (R_x) are coherently combined, there is a frequency difference that results in a beat frequency. This beat frequency is dependent on the round-trip time delay and provides the range information for a target.

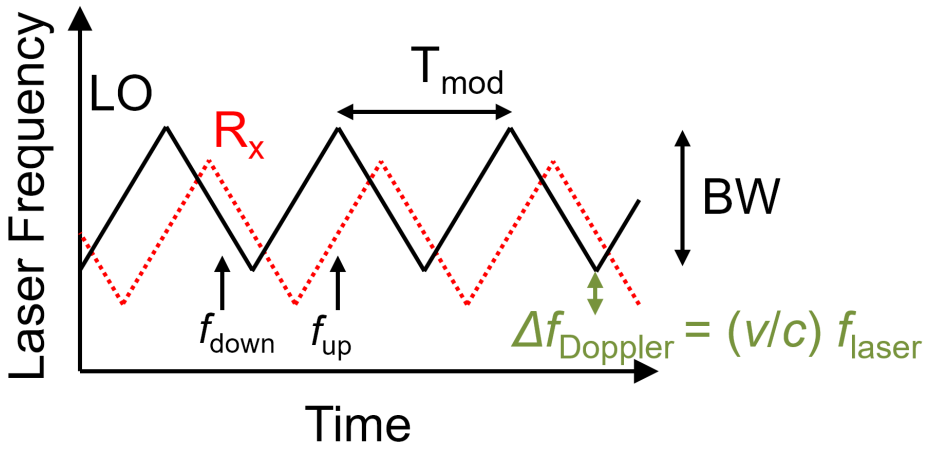

Figure 1-2: Plot demonstrating the frequency-modulated continuous wave (FMCW) signal processing scheme. The local oscillator signal, LO, is shown in black and the returned signal, R_x, is shown in red. A triangular modulation is applied over a time period, T_{mod}. The Doppler shift creates a difference between the f_{down} ramp and the f_{up} ramp of the signals. R_x is decreased by $\Delta f_{Doppler}$ and is a function of the velocity (v) of the detected object, the speed of light (c), and the frequency of the laser f_{laser}.

For an object moving towards the sensor, the beat frequency for the downward chirping period is increased by a Doppler shift ($\Delta_{f_{\text{Doppler}}}$) and the beat frequency for the upward chirping period is decreased by the same amount, Fig. 1-2. Taking the difference and the sum of the two frequencies, both the distance and radial velocity of an object can be calculated [7]. An advantage of the scheme, is that the coherent detection will only create a signal if the received light is coherent with the LO, oth-

erwise any other light source is rejected and does not contribute to the overall signal. The overall signal power is also increased before the final measurement because the received signal is mixed with the LO. Lastly, since the beat frequencies are in the MHz range, the electrical bandwidth for the modulator and receiver are significantly lower than in the ToF scheme (GHz for ToF vs MHz for FMCW) [7]. The unique strengths of FMCW lidar makes it a contender for next-generation sensors used for autonomy; however, there is complexity with the laser since FMCW requires a tunable laser that emits a wide range of wavelengths.

1.2 Industry Requirements for the Mass Adoption of Lidar

Before the benefits of lidar can be widely used by autonomous vehicles and machines, lidar units need to be manufacturable at large volumes, while having high performance sensing, and must cost two orders of magnitude less than current commercial systems [8]. The fully autonomous vehicles application space highlights the performance and development challenges facing the lidar industry (Table 2.1) [7]. These requirements include cost on the order of $100 per unit [9], ranging greater than 200 meters at 10 percent object reflectivity, a minimum field of view (FOV) of 120° horizontal by 20° vertical (Table 1) [10], 0.1° angular resolution, at least 10 frames per second for an entire field of view, and scalable manufacturing (millions of units per year). Any viable lidar solution must also demonstrate multi-year reliability under the guidelines established by the Automotive Electronics Council which is the global coalition of automotive electronics suppliers. Although there has been major progress in the industry over the past decade, there is yet to be a lidar sensor that can meet all the industry needs simultaneously.

To date, autonomous vehicles and systems have relied primarily on mechanical-based lidar that use moving components to steer an optical beam. A commonly used lidar design is comprised of an array of lasers, optics, electronics, and detectors

on a mechanically rotating stage [11]. The need to assemble and align all of these parts leads to high costs and relatively low manufacturing volumes, and the wear and tear on the mechanical components raises questions from customers about long-term reliability. While these lidar systems, produced on a scale of tens of thousands of units per year, have allowed the field of autonomous vehicles and machines to make headway, they are not suitable for the ubiquitous deployment of lidar. For these reasons, there is a big push towards eliminating mechanical components and moving towards compact designs that are more reliable and can be manufactured at larger volumes and a lower unit cost.

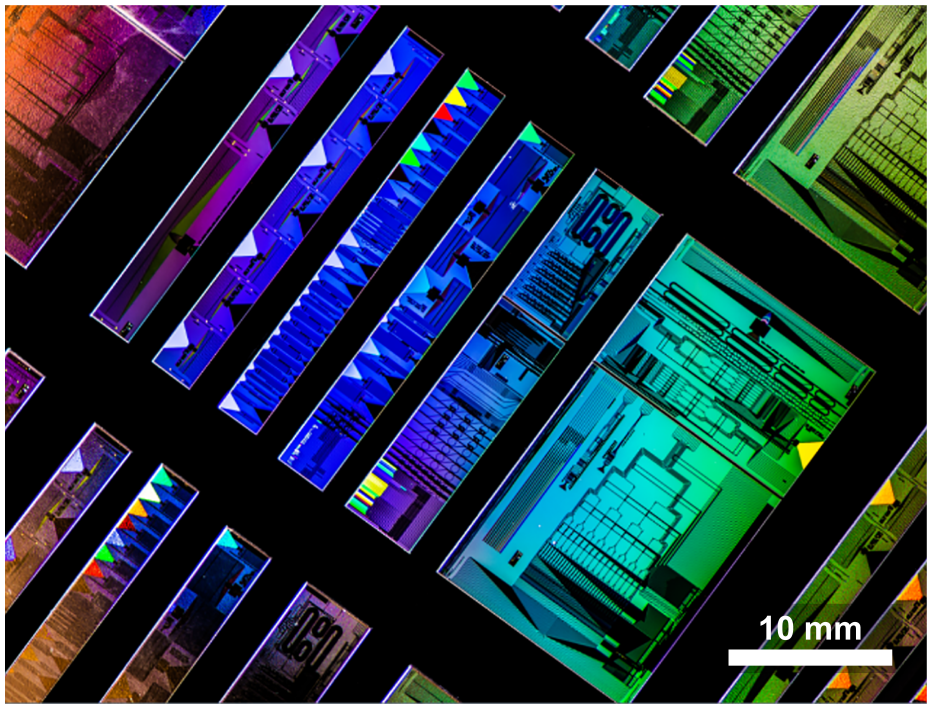

Figure 1-3: Camera image taken with an single lens reflex camera and a glancing light setup. Photonic integrated circuits for lidar fabricated using MIT Lincoln Laboratory's 90 nm silicon nitride fabrication platform. Each die has different test designs of the planar lens solid-state beam steering technology. Courtesy of Glen Cooper, MIT Lincoln Laboratory.

1.2.1 Solid-State and Lidar-on-a-Chip

There are two concepts in lidar design that address the reliability and scalability challenges for this technology. First, "solid-state" describes a lidar sensor that has

eliminated the mechanical modes of failure by using no moving parts. Second, "lidar-on-a-chip" describes a system with the lasers, electronics, detectors, and optical beam steering mechanism all integrated onto semiconductor chips. Lidar-on-a-chip systems go beyond solid-state because these designs attempt to further reduce the SWaP-C of the sensor by integrating all of the key components onto the smallest footprint possible. This system miniaturization reduces the complexity of the assembly and will enable high volume production at scale. This is all possible because lidar-on-a-chip architectures can fully leverage CMOS compatible materials and wafer-scale fabrication methods established by the semiconductor industry and more recently the integrated photonics industry [12, 13, 14]. Fig. 1-3 shows an image of novel planar lens beam steering components made via an photonic integrated circuit (PIC) platform. The PIC was fabricated on 200 mm wafers using MIT Lincoln Laboratory's 90 nm node CMOS foundry and 1550 nm silicon nitride (Si_3N_4) platform [15]. Once a final solution is proven, there is anticipation from industry experts that just like the integrated circuits inside computers and smartphones, millions of lidar units can be manufactured every year.

1.3 Current Approaches to Optical Beam Steering for Solid-State Lidar-on-a-Chip

To realize the vision of ubiquitous lidar, there have been several emerging approaches to optical beam steering under the umbrella of solid-state lidar and lidar-on-a-chip. Some of the key approaches include: microelectromechanical systems, metasurfaces, and optical phased array platforms.

1.3.1 Microelectromechanical Systems

A microelectromechanical system (MEMS) based lidar uses an assembly of optics and a millimeter-scale deflecting mirror to achieve steering of a laser or laser array [10, 16]. Although MEMS mirrors are fabricated using semiconductor wafer manufacturing,

the architecture itself is not a fully integrated lidar-on-a-chip system since optical alignment is still needed between the laser(s), MEMS mirror, and bulk optics [17]. One of the trade-offs in this design is between the scanning speed and the maximum steering angle for a particular aperture/mirror size. This is because the aperture size directly relates to the detection range. This trade-off exists because a MEMS mirror acts like a spring, so as its size and mass increases, its resonant frequency decreases and limits the possible scanning speed [16].

1.3.2 Liquid-Crystal Metasurfaces

A liquid-crystal metasurfaces (LCM) is a semi-analogous architecture to a MEMS system but with the MEMS mirror replaced by a liquid crystal surface with structured unit cells called a metasurface. LCMs use an array of subwavelength scatterers mixed with liquid crystals to impart a tunable phase front onto a reflected laser beam, which allows for beam steering [9]. These designs have large optical apertures and a wide FOV but current modules are currently limited to 150-meter ranging. Not much has been published on the limitations of current designs developed by industry. Like MEMS lidar systems, the LCM steering mechanism is built using a semiconductor wafer manufacturing process, although the system is not fully on-chip since the laser input needs to be aligned at an angle to the surface of the LCM [18, 19].

1.3.3 Optical Phased Arrays

An optical phased array (OPA) uses an array of optical antennas, each requiring phase control, to generate constructive interference patterns that form a steerable optical beam [20, 6]. However, as the size of the emitting aperture increases, the electronic complexity of the system increases and limits scaling since it requires hundreds to thousands of active phase shifters controlled simultaneously [21]. Moreover, the size of optical waveguides places practical fabrication constraints on the ideal antenna spacing (half wavelength) and therefore degrades the optical beam, an effect called aliasing, which limits the usable horizontal FOV. More recent designs use aperiodic

waveguide spacing and different waveguide cross-sections to solve these issues [22, 23, 24], but each creates trade-offs such as limitations on the vertical scanning and the reduction of optical power in the main beam.

1.4 Introduction to Planar Dielectric Lens Approaches for Beam Steering

Each one of these approaches has shown an improvement over conventional mechanical-based lidar in various metrics such as range, reliability, and cost, but it is still unclear whether they can hit all the requirements for fully autonomous vehicles. Recognizing these challenges, the Photonic and Modern Electro-Magnetics Group at MIT and MIT Lincoln Laboratory (MIT LL) researchers collaborated to develop a planar lens design for optical beam steering that could solve the remaining challenges for solid-state lidar [25].

A point of inspiration was the Rotman lens [26], invented in the 1960s at MIT LL, to enable passive beam-forming networks in the microwave regime. The Rotman lens receives microwave radiation from multiple inputs along an outer focal arc of the lens. The lens spreads the microwaves along an inner focal arc where an array of delay lines imparts a phase shift to form a collimated beam. While some of the intuition from the microwave regime translates to the optical and near-infrared domain, the length scales and available materials require a different lens design and system architecture. In fact, the Rotman lens falls within a larger family of wide-angle dielectric lenses [27] that have been used for beam steering in the microwave domain. All of these dielectric lenses are based on the principals of geometrical optics and use ray-tracing methods to determine the lens surfaces [28]. Taking inspiration from the all of the dielectric lenses mentioned above, Skirlo theoretically presented a planar lens design for two-dimensional optical beam steering in the near-infrared (IR) [29].

Herein, this thesis focuses on the experimental demonstration of two novel planar lens designs that are suitable for solid-state optical beam steering and work in the

near-infrared. The first is the experimental demonstration of the aplanatic lens design theoretically shown by Skirlo. The second is the experimental demonstration of a circularly symmetric Luneburg lens that is based on controlling the effective refractive index of the lens via nanoscale patterning [30]. This second system also uses a circularly symmetric grating for uniform emission over a wider FOV.

1.5 Overview of Thesis

1.5.1 Chapter 2: Aplanatic Lens

This chapter discusses the experimental demonstration of the aplanatic planar lens-based optical beam steering architecture. The general design architecture is based on a near-infrared tunable laser, a Mach-Zehnder interferometer (MZI) switch tree, a planar aplanatic lens that collimates and steers the optical mode in-the-plane of the chip, and a grating for out-of-plane coupling. Three separate planar lens devices are experimentally demonstrated: a planar lens device with 16 ports, 32 ports, and a third 8 port device that is operated electronically with a MZI switch tree. The device is fabricated using a wafer-scale fabrication process and allows for two-dimensional optical beam-steering with lower electronic complexity than other on-chip beam steering solutions.

1.5.2 Chapter 3: Luneburg Lens

This chapter discusses the first demonstration of a Luneburg lens and circular grating for wide field of view optical beam steering in two-dimensions. It also discusses the performance of various grating designs aimed at improving the optical beam performance. The grating variations include a single-layer non-apodized grating and several double-layer gratings with either a linear, half-Gaussian, or full Gaussian apodization scheme of the grating fill-fraction.

1.5.3 Chapter 4: Conclusion

This chapter describes several architecture challenges that need to be addressed before a planar lens architecture can be deployed in a high performance lidar system. It discusses the grating length and corresponding aperture size, the device level performance required for a high frame rate, and the laser requirements for long distance ranging and the vertical FOV.

Chapter 2

Optical Beam Steering with a Planar Lens-Based Architecture

2.1 Introduction

Free-space optical beam steering is an important technological capability because of its applications in optical communication links [1] and sensing such as light detection and ranging (lidar) [2]. Over the past decade, there has been significant efforts to develop a beam steering architecture that can lead to solid-state lidar with lower size, weight, power consumption, and cost (SWaP-C) while still meeting a high level of sensing performance and reliability. A solid-state optical beam steering architecture that meets all of these needs for lidar is highly desirable because it is considered to be an enabling technology for autonomous vehicles, robots, drones, and related intelligent systems.

Photonic integrated circuit (PIC) based approaches are especially compelling because they promise the ability to create a fully electronic based beam steering architecture that leverages the wafer scale capabilities of a growing integrated photonics industry [12, 13, 14]. Among integrated photonics approaches, optical phased arrays (OPAs) have promised a non-mechanical approach without the need for any bulk optics to steer a coherent beam bidirectionally. In this type of architecture, a 1D or 2D array of dielectric grating antennas with adjustable phase is used to emit a coherent

optical beam. The phase of each antenna can be controlled by either a thermo-optic or electro-optic phase shifter. In the 1D case, the polar angle (θ) steering is done by exploiting the dispersive properties of the grating, where different wavelengths emit at different angles. In many ways, OPAs used for lidar are the photonic counterparts of RF phased arrays used for radar. However, this direct translation brings disadvantages and challenges in the optical domain. Whereas metallic waveguides can be spaced at sub-wavelength pitches, dielectric grating antennas used in OPAs have usually been separated at a minimum of 2 μm [20, 6] due to evanescent coupling between dielectric waveguides. This spacing is larger than the ideal $\lambda/2$ pitch for a phased array and leads to aliasing (also called grating lobes) and therefore reduces the optical power in the main beam and the functional field of view (FOV). Some OPA designs have used non-uniform emitter spacing [22, 23] to avoid constructively interfering the additional grating lobes; however, this leads to the power contained in a grating lobe to be spread out over a wide range of angles and increases the background signal. Consequently, this increased background reduces the signal-to-noise ratio of the main beam. Other index-mismatched designs have shown a 180° FOV in the azimuthal (ϕ) direction, but have limited steering in the polar direction due to use of an end-fire design [24].

Moreover, since an OPA with a large aperture ($\geq$ 1mm) can require hundreds of phase shifters to coherently interfere, the power and control algorithms required for scaling the architecture can be significant, or even prohibitive. Since thermo-optic phase shifters can consume between 10-160 mW each to achieve a π phase shift [31, 32], a large OPA can consume a significant amount of power, although emerging phase shifter designs are starting to address these concerns [33]. These issues are important to address since one of the largest OPAs to date required 1024 antennas and consumed 55 Watts for just the phase shifter control [21]. Furthermore, many demonstrations to date have depended on an open-loop control method that is based on look up tables. For real world applications, the calibration methods will likely require closed-loop controls and still need improvement [34, 35]. All of these challenges create an opportunity to use novel integrated photonic designs to mitigate these problems.

Upon close inspection, the microwave literature contains a class of dielectric lens-based beam forming designs [26, 36, 37, 38, 39, 40, 41] that helped overcome the challenges of phased arrays in the RF domain and produced wider-angle scanning, narrower beams, and higher beam quality.

2.2 Introduction to Aplanatic Lens Designs

Of specific interest are aplanatic lens designs which minimize wavefront errors by reducing both spherical and coma abberation. For many standard designs, this physically allows for two aplanatic points on the axis of an optical system such that all rays emerging from one point will converge to the other point on the axis. The first issue that aplanatic lens address is spherical abberation, which is when rays from a point on the axis passing through the outer zones of the lens will focus at different distances than the rays passing through the inner zones of the lens. The second issue is coma, which is when an off-axis point source creates an asymmetric wavefront distortion that increases linearly with angle, making off-axis point sources appear like a trailing "comet". To address both issues, the Abbe sine condition is used to bend the first and second principal planes of the lens into spheres so that a ray entering the system at a certain height exits the system at the same height [42]. The rays can exit to form a collimated beam as shown in Fig. 2-1. The same principals can be used to have a point source expanded and collimated by an aplanatic lens.

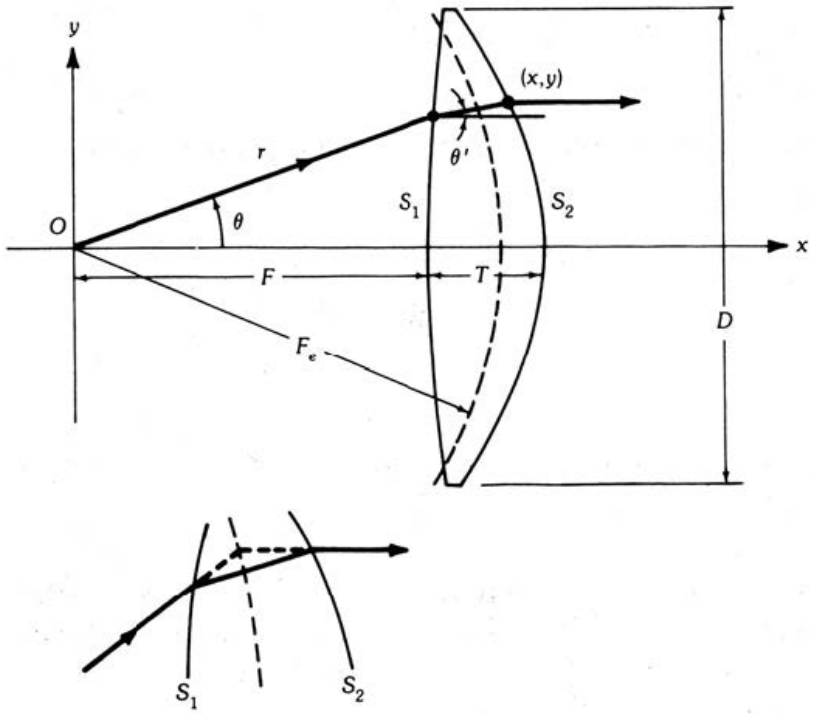

Figure 2-1: A dielectric lens that is constrained by the Abbe sine condition. For a specific focal length (F) and lens thickness (T), there is a solution for the first and second interface (S1 and S2) of the lens that provides a coma-free and spherical abberation-free design. Reprinted/adapted by permission from Springer Nature: Lens Antennas by Jar Jueh Lee © 1988.

2.3 Planar Lens Architecture for Two-Dimensional Optical Beam Steering

Herein is demonstrated a novel planar lens architecture for two-dimensional (2D) beam steering in the optical domain based on an aplanatic lens design which is fabricated on a PIC platform [43]. Three separate planar lens devices are tested, including an architecture with 16 ports, 32 ports, and a third 8 port device that is operated fully electronically with a Mach-Zehnder interferometer (MZI) switch tree controlled by silicon nitride (Si_3N_4) thermo-optic phase shifters. The general design of the planar lens-based beam steering architecture is described in Fig. 2-2: First, a near-infrared laser is fiber-coupled onto the chip via a single mode lensed fiber. The optical transverse electric (TE) mode is routed to a series of waveguides where the path is

determined by a MZI switch tree controlled by integrated phase shifters. Since the MZI tree is binary at each stage, only a few phase shifters need to be turned on to determine the optical path. The waveguide mode is converted to a slab mode as it enters the region containing the planar aplanatic lens. The lens collimates the propagating slab mode which is then scattered out-of-plane by a grating. While various materials could be used for the routing waveguides and lens, Si_3N_4 and amorphous silicon (a:Si) are chosen to form the dielectric stack used to control the effective refractive index in different regions of the photonic integrated circuit (PIC). Apart from being readily deposited via wafer-scale techniques, this combination was chosen because the a:Si[44] has a significantly higher refractive index than Si_3N_4[45] at 1.55 μm and thus could provide a significant change in the effective index of the dielectric stack.

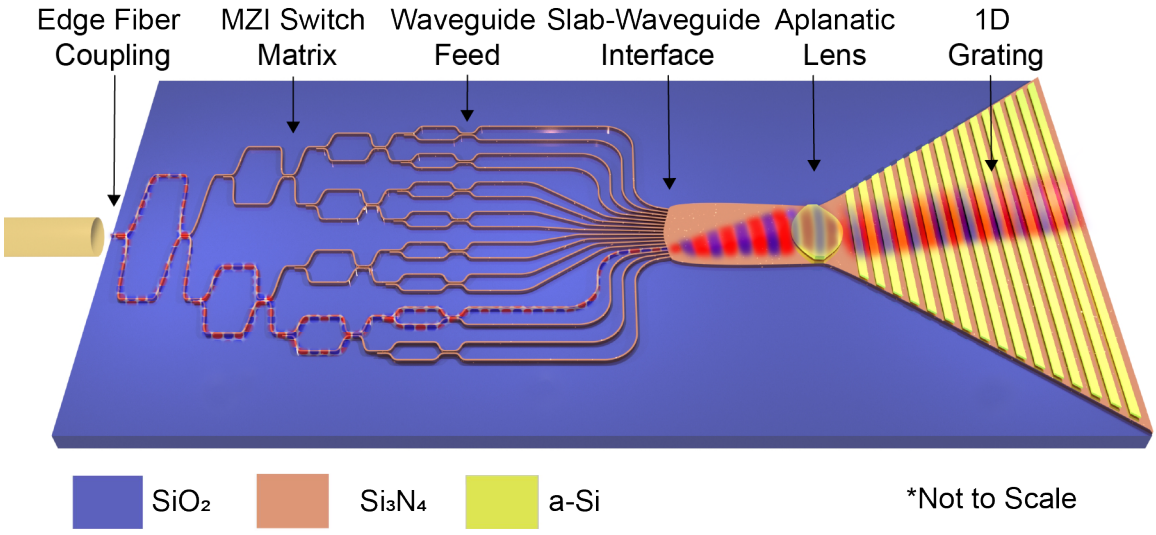

Figure 2-2: Proposed beam steering architecture. A near-infrared laser is fiber-coupled onto the chip. The laser light is routed through an optical switch matrix formed by a MZI switch tree which selects the waveguide feeding the lens, thus steering the beam in the in-plane direction. The waveguide mode is converted to a slab mode and is then fed into the aplanatic lens. The lens collimates the light and then it is scattered out-of-plane by a wavelength dependent 1D grating. Tuning the laser wavelength steers the optical beam in the out-of-plane direction.

The two mechanisms used for beam steering are further illustrated in Fig. 2-3. First as seen in Fig. 2-3 (a-c), the port switching changes the in-plane angle of propagation into the lens and consequently controls the free space azimuthal angle (ϕ). Second, by tuning the wavelength (λ) of the laser source, the free space polar

angle (θ) is controlled by designing a one-dimensional (1D) grating to scatter the slab mode into the far-field. This is the same mechanism used in 1D OPAs for steering in the polar direction and is governed by the well known grating equation where n_{eff} is the effective refractive index of the guided mode in the grating, n_c is the refractive index of the cladding, Λ is the grating period, λ is the laser wavelength, and θ_m is the angle of emission of the grating order m:

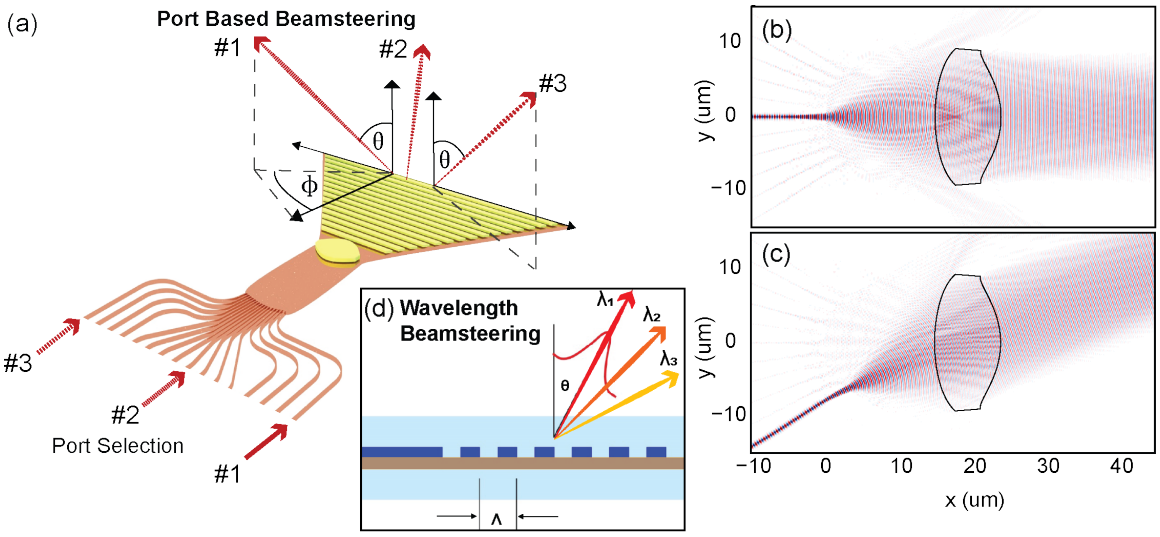

Figure 2-3: Schematic and simulations of planar lens-based beam steering. (a) Switching the port, which feeds the planar lens, controls the in-plane (azimuthal) angle. (b) Tuning the laser wavelength changes the emission of the beam in the out-of-plane (polar) angle. (c) Two-dimensional finite-difference time-domain (FDTD) simulation of on-axis port excitation and (d) off-axis port excitation of a planar lens.

$$n_{eff} - n_c \sin\theta_m = \frac{m\lambda}{\Lambda} \tag{2.1}$$

2.4 Lens and Aperture Design

There are many types of lens-based solutions invented for use in radar, including but not limited to circularly symmetric Luneburg lenses [46, 47], metallic lenses [36], and bootlace lenses [48]. Insights are taken from wide-angle dielectric lenses [49, 37, 40] since they can be readily implemented in a PIC platform. The aplanatic lens is designed by constraining the shape to satisfy the Abbe Sine condition, which

eliminates spherical and coma aberrations [49, 41]. Specifically, the surface of the lens is determined by using Snell's law and a quadratic equation that represents the phase constraints for the lens. A resulting differential is derived and then numerically integrated to solve for the surface of the lens. The algorithm also takes as inputs the aperture diameter (D), the central thickness of the lens (T), the distance of the phase center to the vertex of the lens (F), the effective focal length (F_e), and the lens refractive index, which is the ratio of the effective indices n_1/n_2 for a transverse electric (TE) mode [41]. For these designs, the region with a:Si on top of Si_3N_4 has an effective index n_1 and the region with only Si_3N_4 has an effective index n_2. After generating the lens design, the focal plane is identified via ray-tracing through the lens and the feed positions and the input angles are optimized by maximizing the 2D directivity (from the aperture pattern computed from ray-tracing). Ray-tracing is then done through the grating to compute the full 3D directivity for several optimized port locations and angles. The use of ray-tracing to describe planar integrated devices in the optical domain builds on experimental and theoretical work conducted by Ulrich et al. who directly verified its application to planar prism and lens devices [50], and Ura et al. who used ray path length arguments to design the first focusing grating couplers [51].

As originally described by Skirlo [29], the direction of the free-space beam is characterized by $u_x = \sin(\theta)\cos(\phi)$ and $u_y = \sin(\theta)\sin(\phi)$ and can be calculated by tracking the phase accumulated by the collimated rays emitted from the lens and discretely sampling them at the grating teeth. As shown in the Appendix, the momentum conservation in the grating can be written as:

$$\begin{aligned} u_y =& n_2 \sin(\phi_{in}) \\ u_x =& \frac{k_{x,avg}(\phi_{in})}{k_0} - \frac{\frac{2\pi m}{\Lambda}}{k_0} \end{aligned} \tag{2.2}$$

where $k_{x,avg}$ is the average momentum in the x-direction. The grating allows the phase matching between the slab waveguide mode and free-space radiated modes

through the 1D crystal momentum $\frac{2\pi m}{\Lambda}$. The in-plane angle coming out of the lens and into the grating determines the wave vector components k_x and k_y which are normal and parallel to the grating teeth respectively and thus affect the emission from the aperture. By making the approximation $k_{x,avg} \approx n_{eff} k_0 cos(\phi_{in})$ where $n_{eff} = n_1 d + n_2(1-d)$ is the effective index of the grating and d is the grating duty cycle, the emission u_{x0} and u_{y0} can satisfy an elliptical equation (more details in the Appendix):

$$((u_x + \frac{m\lambda}{\Lambda})/n_{\text{eff}})^2 + (u_y/n_2)^2 = 1 \tag{2.3}$$

Thus, switching ports in-plane takes a path along an elliptical arc in u_x and u_y space, while tuning λ moves the arc forward and backwards. This analytical form can be compared to experimental results as will be shown below.

2.4.1 Planar Lens Fabrication and Dielectric Layer Stack

The photonic integraed circuits (PICs) were fabricated on 200 mm wafers using MIT Lincoln Laboratory's 90 nm node CMOS foundry and 1550 nm Si_3N_4 PIC platform, shown in Fig. 2-4. The Si_3N_4 waveguides and slab were fabricated by low pressure chemical vapor deposition (LPCVD) deposited on top of a 5 μm bottom silicon dioxide (SiO_2) layer. An oxide filler was then deposited on top of the Si_3N_4 and chemical mechanical polishing was used to polish back to the top of the Si_3N_4 waveguides and create a planarized surface for subsequent depositions. The apalantic lens and gratings were created by depositing and patterning a thin film of amorphous silicon (a:Si) directly on top of the Si_3N_4. A top cladding oxide of 2 μm was deposited over the entire structure. For the active devices, heaters for the thermo-optics phase shifters were then fabricated on top of this stack (more details are provided on the electronically controlled 8 port MZI device below). The thickness of each dielectric layer was measured via spectroscopic ellipsometry on reference films deposited on monitor wafers. A range of PICs were fabricated using this dielectric stack, including those with and without MZIs.

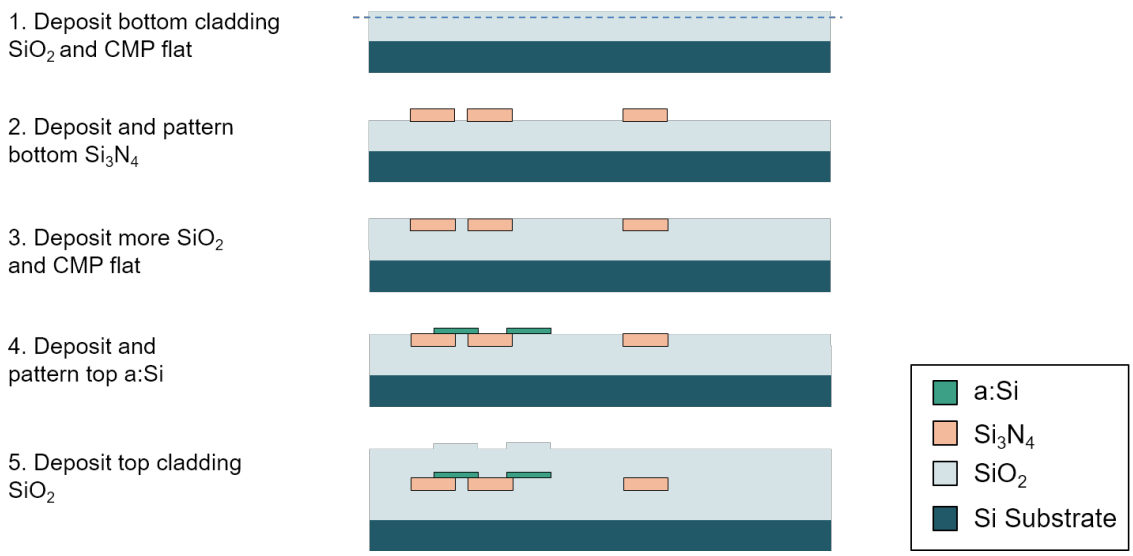

Figure 2-4: Schematic of the wafer scale deposition process. This schematic excludes the deposition of the heating elements for the thermo-optic phase shifters. (1) Bottom oxide cladding is deposited on top of a silicon wafer with preexisting native oxide. (2) Approximately 200 nm of Si_3N_4 is deposited. (3) Additional oxide is deposited and flattened via chemical mechanical polishing planarization. (4) Approximately 10-30 nm of a:Si is deposited on top of the Si_3N_4. (5) An additional top oxide cladding is deposited.

2.5 Experimental Results: Optical Beam Steering

Demonstrating the beam steering performance and the quality of the optical beams emitted from the planar lens design is important for evaluating the viability of the architecture for use in lidar applications. First, the angular range for the in-plane (a.k.a. azimuthal) and out-of-plane (a.k.a. polar) directions determines the usable field of view (FOV) for a lidar sensor. Second, the beam divergence of the emitted optical beam determines the resolution of the 3D spatial map generated by lidar. One method of determining the beam divergence is using a camera to record the emitted beams that are subsequently reflected by an infrared Lambertian screen. Using the recorded images, the full width at half maximum (FWHM) can then be measured by using the major and minor axes of individual beams. Lastly, the optical losses of the lens and grating are relevant since long distance measurements require enough optical power being emitted and then detected by the lidar sensor. The influence of the FOV, beam divergence, and optical losses are further discussed in Chapter 4.

2.5.1 16 Port Planar Lens: Evaluated Using a Cartesian Coordinate System

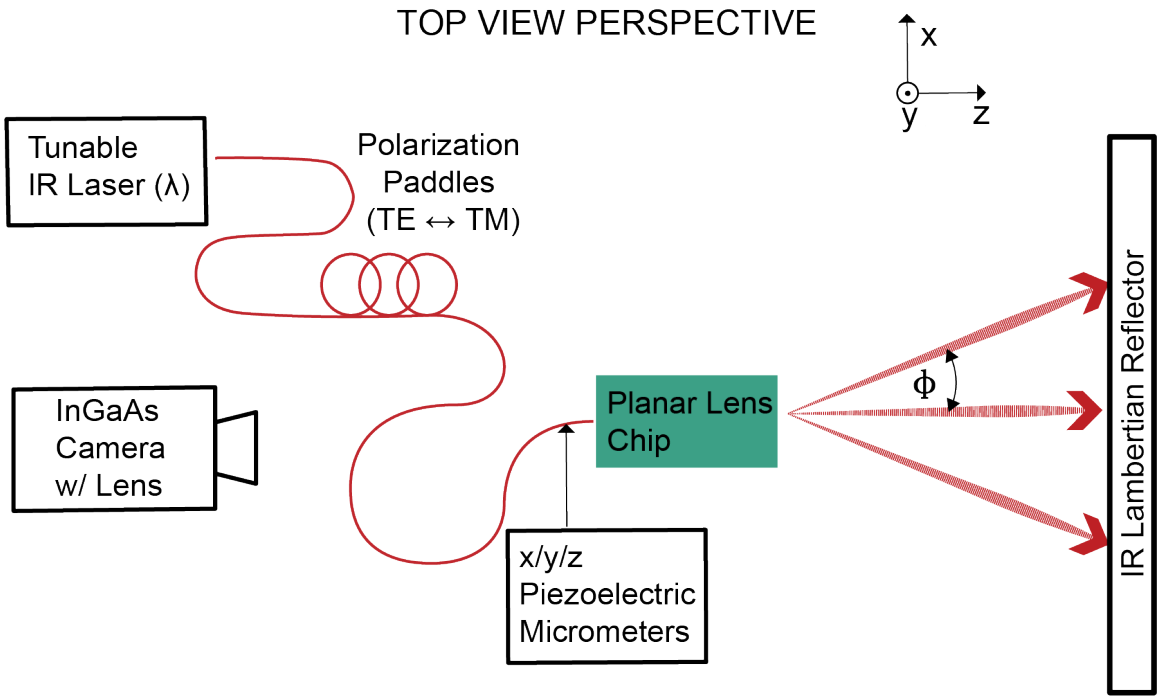

Figure 2-5: Experimental Setup: The tunable laser is coupled into the devices using a tapered lensed fiber. Polarization paddles are used to optimize the TE polarization of the light propagating in the device. Far-field emission from the grating is reflected by a short-wave infrared Lambertian screen and recorded with an InGaAs camera using a high transmission SWIR lens.

For all measurements, the far-field emission was measured by coupling into each individual port via a tapered lensed fiber and recording the emission from the grating. Each beam is reflected by a short-wave infrared Lambertian screen and recorded with an InGaAs camera and a high transmission SWIR lens. The diagram of the setup is in Fig. 2-5.

For the initial proof of concept, a 16 port device was measured. The dielectric stack of the device included a Si_3N_4 slab = 197 nm, and a:Si = 24.5 nm. The grating coupler had a pitch of Λ = 714 nm and a fill-fraction = 0.79. Far-field measurements are shown in Fig. 2-6. Using a Cartesian coordinate system, the azimuthal angle range is ϕ_{range} = 38.8° from ϕ = (21.0° to -17.8°) with a mean angle step increment of $\overline{\Delta\phi}$ = 2.58° via port switching. The polar angle range is θ_{range} = 12.0° from θ =

(22.6° to 34.6°) with a mean angle step increment of $\overline{\Delta\theta} = 0.12°/\text{nm}$ via λ tuning from 1500 nm to 1600 nm.

Since this was the first demonstration, there were several issues with the setup and the approach to the beam characterization. First, the tunable laser (Santec TSL-210) provided slightly varying amounts of power over the wavelength range making it challenging to make a systematic study. Second, the IR camera being used had several dead pixels across the array and low dynamic range. Moreover, the images captured of the emitted optical beams contained several saturated pictures due to the exposure time. This made it impractical to extract conclusive data about both power distribution and beam profile from the images. Therefore, to capture data sets with more useful data the measurement setup was improved by switching to the following equipment: an InGaAs camera with a 320 × 256 pixel array (Goldeye G008 TEX1), a high transmission SWIR lens (KOWA LM16HC-SW) and a Keysight Tunable Laser Source with both very high wavelength and power precision. Both the camera and laser is controlled simultaneously via a LabVIEW control loop.

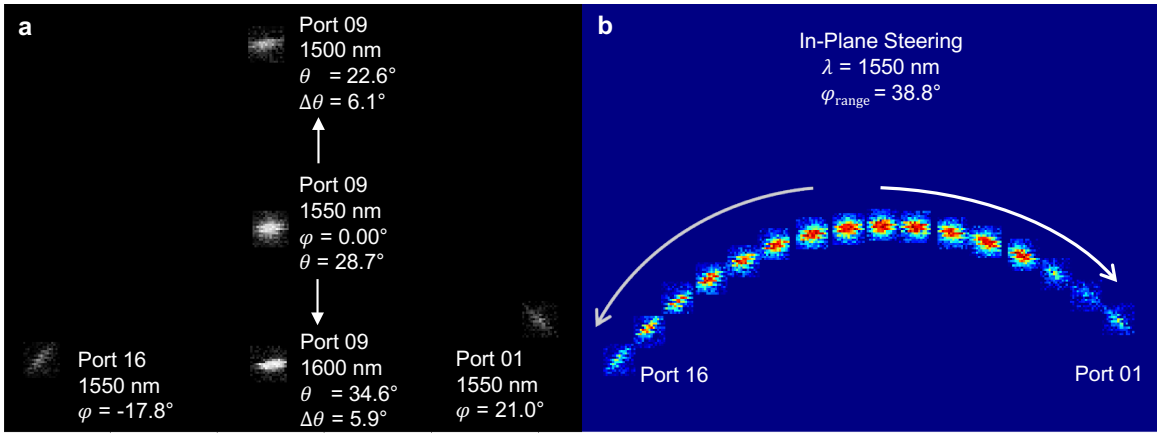

Figure 2-6: (a) Experimental far-field measurements of five distinct beams emitted from the 16 port device. The images of the individual beams were superimposed. Switching λ translates the beam up and down. Switching ports translates the beam right to left. (b) Superposition of sweep in port number (1-16), $\phi_{range} = 38.8°$. The curved path for the port sweep comes from the change of the in-plane and out-plane momentum provided by the linear grating. The change in the brightness of the off-center beams is mostly due to sub-optimal alignment of the lensed-fiber to the facet of each waveguide at the edge of the PIC.

Lastly, it was determined that to correctly characterize the optical beams emitted

from the planar lens devices, the beam profiles needed to be extracted along the major and minor axes of each individual beam. This required the images to be transformed from a Cartesian to a Spherical coordinate system and interpolating to a uniform grid in the polar direction ϕ and azimuthal direction θ.

2.5.2 32 Port Planar Lens: Evaluated Using a Spherical Coordinate System

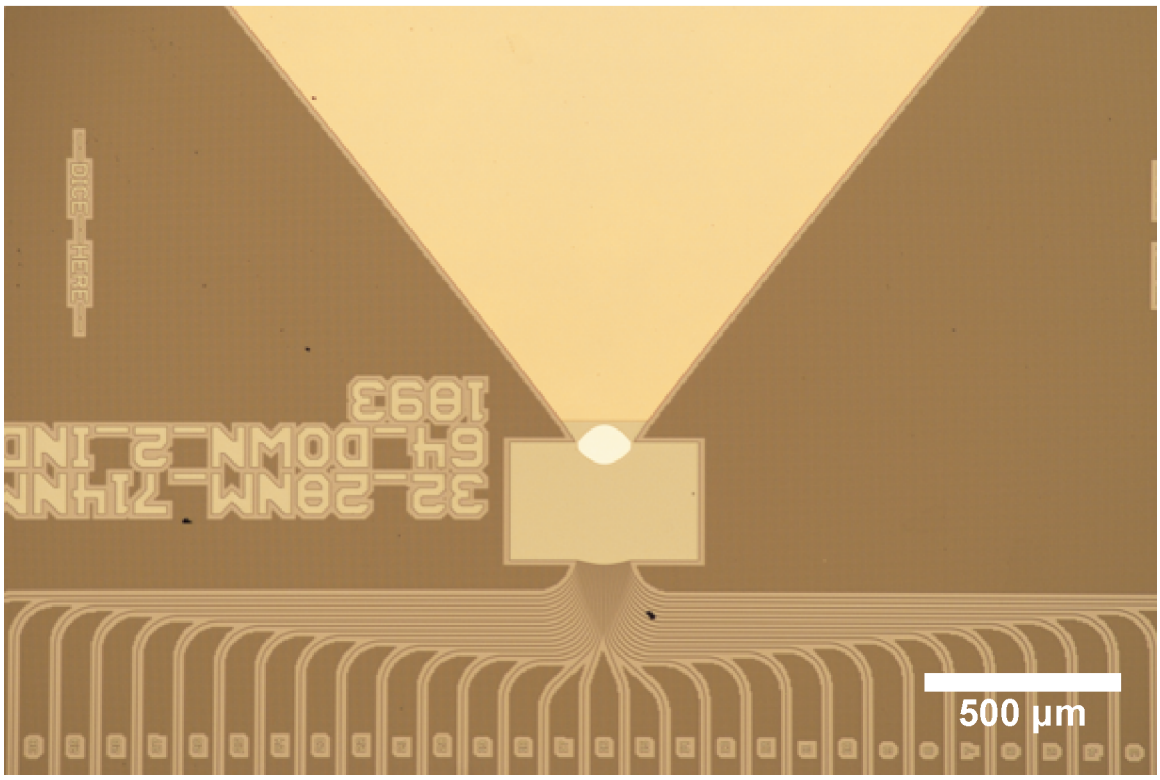

Figure 2-7: Optical microscope image of a 32 port device. An array of 32 Si_3N_4 waveguides feed into a single aplanatic planar lens. The grating coupler has a pitch of $\Lambda = 714$ nm and a duty cycle $d = 0.79$. The lens was designed with a normalized effective index ratio of $n_1/n_2 = 1.093$. A maximum lens diameter of 133 μm was chosen so that it could take inputs from 32 waveguides at a 4 μm spacing along the focal arc.

Next, the lens and grating parameters for the 32 port planar lens device are described below. The 32 port device had dielectric layers estimated to be Si_3N_4 slab = 197 nm and a:Si = 24.5 nm. The device had effective indices $n_1 = 1.73$ and $n_2 = 1.58$ which were modeled via a Finite-Difference Eigenmode (FDE) solver. The

target thickness of the Si_3N_4 slab was chosen to be 200 nm to align with the previously developed fabrication processes and component libraries [15]. The target thickness of the a:Si layer was chosen to be 20 nm to create a higher effective refractive index for region n_2. The final measured thickness of the a:Si was 25 nm. The lens was, thus, designed with a normalized effective index ratio of $n_1/n_2 = 1.093$, Fig. 2-7. A maximum lens diameter of 133 μm was chosen so that it could take inputs from 32 waveguides at a 4 μm spacing along the focal arc of the lens. The 4μm spacing was used to avoid any evanescent coupling between the waveguides. The grating coupler had a pitch of $\Lambda = 714$ nm, duty cycle $d = 0.79$ for region n_1, and a physical length of 1150 μm to ensure full decay of the slab mode.

Cartesian to Spherical Coordinate Transformation and Scaling of the Image Pixels

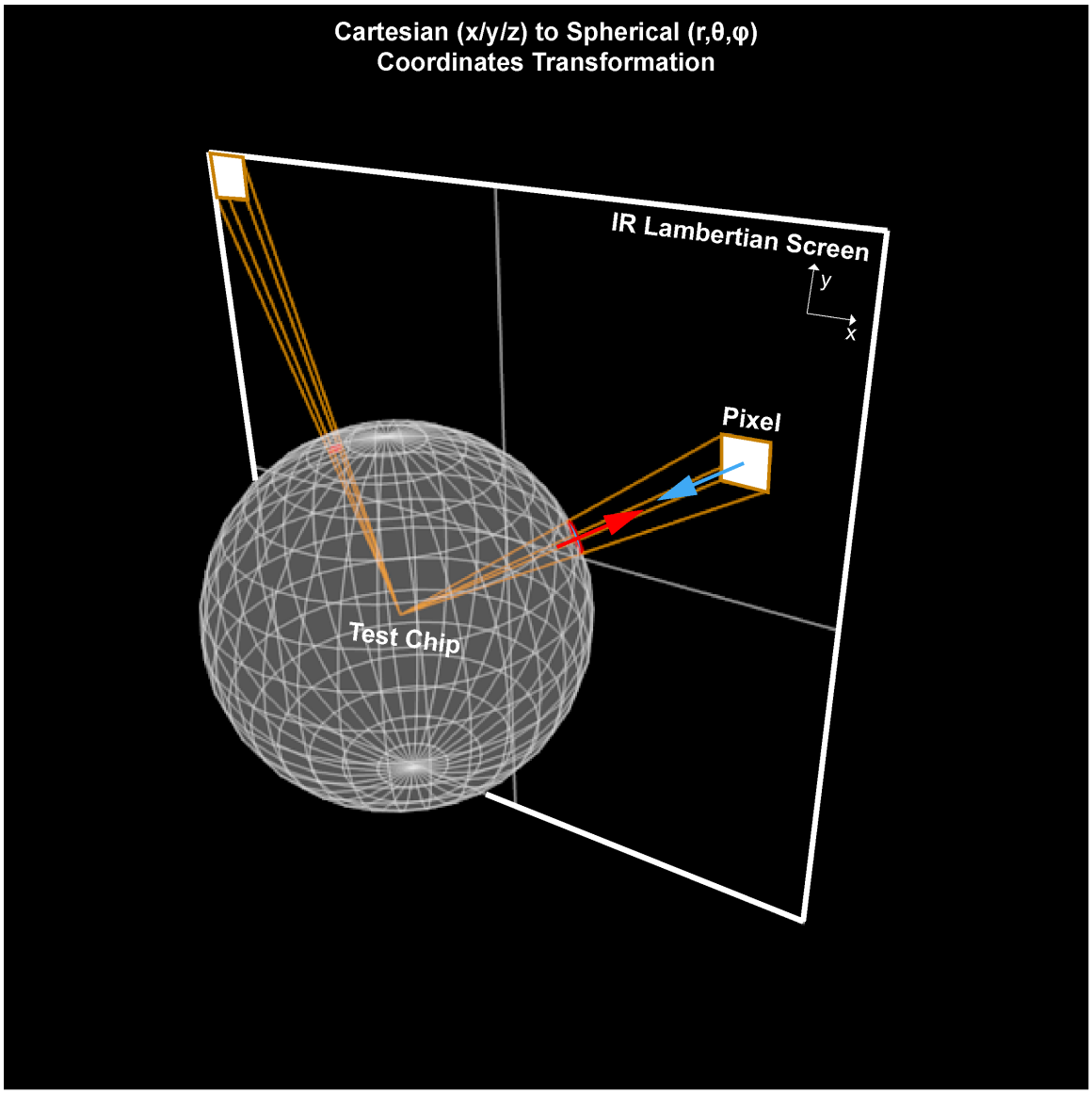

Figure 2-8: Schematic showing a solid angle of a square where θ is the polar angle and ϕ is the azimutal angle, the sphere has a normalized radius r = 1, and the minimum distance of the plane from the center of the sphere is equal to r. The pixel of the image can be projected onto the sphere. The normal to the plane in which the pixels lie is $\hat{n}$. The directional vector from the center of the sphere is $\hat{x} = \frac{\mathbf{x}}{\|\mathbf{x}\|}$. The pixel projected onto the sphere is represented by $\hat{x} \cdot \hat{n}$. The area of the projected pixel onto the sphere is reduced by $\frac{r^2}{\|\mathbf{x}\|^2}$. Adapted from "How do I compute the solid angle of a square in space in spherical coordinates?", by StackOverflow, 2017, Mathematics Stack Exchange.

To obtain the azimuthal (a.k.a. out-of-plane) and polar (a.k.a. in-plane) range of each planar lens device, a coordinate transformation from cartesian to spherical coordinates was performed to calculate the angles corresponding to the projection onto the Lambertian screen. To accomplish the transformation from Cartesian (x,y,z) to Spherical (r, θ, ϕ) coordinates, the intensity values of each pixel imaged on the IR Lambertian screen should be scaled accordingly. This can be done by projecting the pixels with area A recorded on the screen onto a sphere of radius r, where r is the Lambertian screen's minimum distance from the center of the sphere, Fig. 2-8. In this case, the center of the sphere is collocated with the grating aperture of each test device. The standard physics convention is used where, θ is the polar angle and ϕ is the azimuthal angle. The projected area of the pixel on the sphere is approximated via the area of the plane tangent to the sphere. The normal vector to the plane in which the pixels lie on the Lambertian screen is $\hat{n}$ and the vector from the center of a sphere to the center of the pixel on the Lambertian screen is $\mathbf{x}$. Thus, the directional vector from the center of the sphere is $\hat{x} = \frac{\mathbf{x}}{\|\mathbf{x}\|}$. Upon mapping the pixel onto the sphere, the area is scaled by two factors. First is the inner product of the directional vectors $\hat{x}$ and $\hat{n}$ where the normal vector $\hat{n}$ is also the directional vector of the pixel projected onto the Lambertian screen. Since the pixel is projected onto the sphere, the area is also multiplied by the square of the ratio of the distances $\frac{r^2}{\|\mathbf{x}\|^2}$. The original pixel with area A is then scaled in the following way: $\hat{x} \cdot \hat{n} \frac{r^2}{\|\mathbf{x}\|^2} A$. This scaling is used to adjust the intensity of the pixels once they are interpolated in the spherical coordinate system with the desired grid [52]. In this case the linear grid has a 0.1° resolution along both axes.

Two-Dimensional Gaussian Fitting

The 2D Gaussian fitting script is a modified version of the programs written by Nootz [53] and Diaz [54]. The code fits the data using the MATLAB function 'lsqcurvefit' to find the position, orientation, and width of a 2D Gaussian. The fit uses an initial guess for the seven coefficients (A) of the guassian where they are the following collection of terms: [Amplitude of the Gaussian (Amplitude), x-center (x0), standard

deviation (σ_x), y-center (y0), standard deviation y-Width (σ_y), angle of rotation (angle), average of the background noise (Bckg)]. The script is written two perform two Gaussian fittings. It takes the initial guess and fits to an initial Gaussian and then uses the coefficients of the first solution to fit to a second Gaussian curve. The full width half maximum (FWHM) of the Gaussian in either the x- or y-direction is defined by $2\sqrt{2\ ln(2)}\ \sigma$ where σ is the standard deviation of a Gaussian distribution [55]. The cross-sections were fitted to a Gaussian peak because of the broader peak shape.

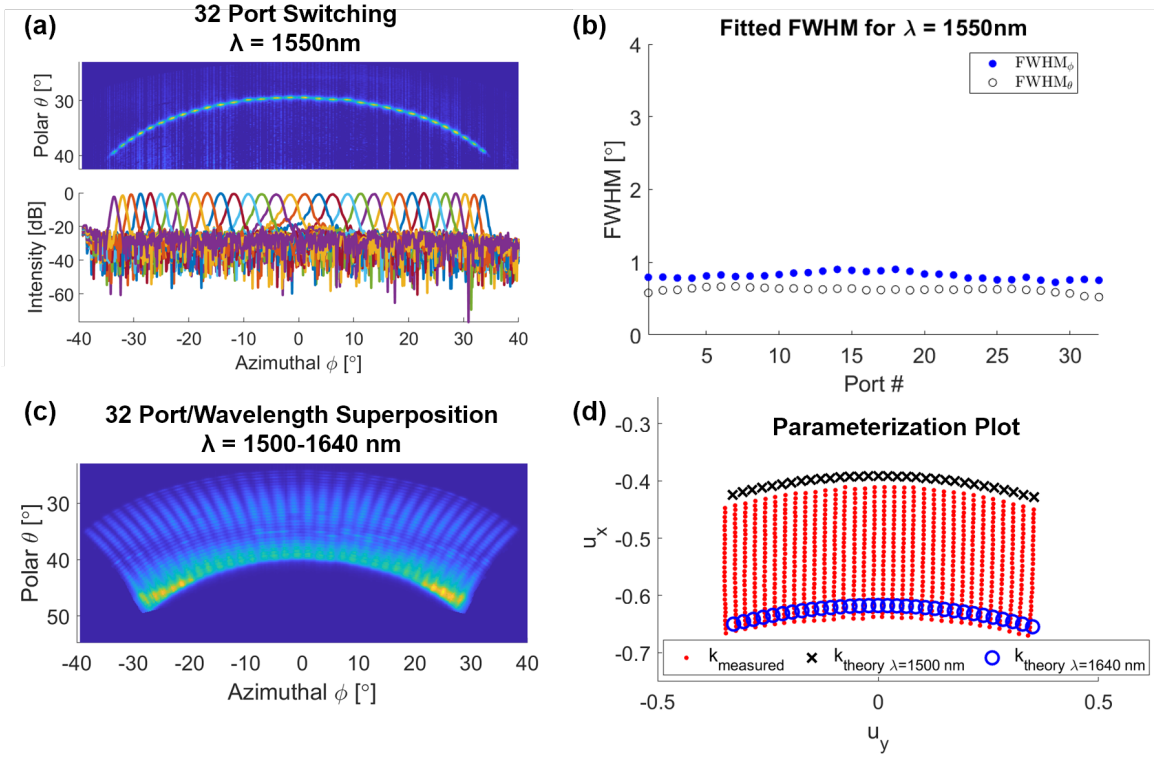

Figure 2-9: Experimental far-field beam emission, cross-sections, and FWHM of 32 beam planar lens device. Port switching is conducted by mechanically moving a tapered lensed fiber from port to port and optimizing the output via a micrometer and piezo controller. (a) Azimuthal scanning range for all of the ports with accompanying far-field beam cross-sections plotted in dB at λ = 1550 nm. All sidelobes and noise are below -15.0 dB. These sidelobes are consistent with the fourier transform of a 1D aperture of finite length. (b) Plot of the FWHM in both the azimuthal (ϕ) and polar (θ) direction for all 32 ports, the wavelength is held constant at λ = 1550 nm. (c) Digital superposition of the images recording the optical beams emitted from all 32 ports (using a range λ = 1500-1640 nm at an interval of 5 nm). (d) Comparison of theory to experiment using the ellipsoid parameterization based on u_x and u_y.

Using the Spherical Coordinate System, the azimuthal scanning range for the 32 port device is 67.1° from ϕ = (33.5° to -33.6°) with a mean angle step increment of $\overline{\Delta\phi}$ = 2.16° via port switching. The polar angle range is 15.3° from θ = (24.3° to 39.6°) with a mean angle step increment of $\overline{\Delta\theta}$ = 0.546 ° every 5 nm using wavelength tuning from 1500-1640 nm, with emission of 29.5° at λ = 1550 nm. The full width at half max (FWHM) of the beams shown in Fig. 2-9(b) was fitted in both the azimuthal (ϕ) and polar (θ) direction for all 32 ports while keeping λ = 1550 nm (that is, the FWHM of each beam was taken along the major and minor axis of the beam).

It must be noted that the angular range in the spherical coordinate system is not a practical FOV for a scanning system used for lidar. The practical FOV is provided by the geodesic which is the shortest possible line between two points located on a sphere and its corresponding angle. The angle that corresponds to the geodesic can determined by calculating the dot product of the two vectors, $\vec{a}$ and $\vec{b}$, that describe the optical beams at the extreme points of the FOV, $cos(\theta) = \frac{\vec{a}\cdot\vec{b}}{|\vec{a}||\vec{b}|}$. Using this framework, a FOV of 40.9° by 15.3° in the in-plane and out-of-plane direction is calculated.

Using the rotated Gaussian fitting, the average measured FWHM of the major axis of the 32 beams is 0.82°, which is the same order of magnitude as the approximation λ/D = $\frac{1.550\mu m}{133\mu m}$ = 0.67°. The average measured FWHM of the minor axis is 0.621°, which is also acceptable considering that the power of the slab mode decays as 1/e at an effective grating length of 68 μm (simulated via FDTD).

A superposition of emitted beams for all 32 ports and several measured wavelengths is shown in Fig. 2-9(c). A comparison of theory to experiment using the ellipsoid parameterization (u_x, u_y), Fig. 2-9(d), shows agreement between the experimental values and the analytical solution based on the parameterization. The differences in u_y are most likely attributed to the error between the actual and estimated dielectric thicknesses and resulting refractive indices n_1 and n_2 used in the analytical solution.

The power of the steered optical beams was measured by placing an InGaAs integrating sphere directly in the path of the beam. The sphere was placed at most 5

Table 2.1: Power measurements for several ports of the 32 port device, after taking into account setup loss.

Port #	**Output (µW)**	**Output (dBm)**
1	55.8	-7.920
2	70.6	-6.898
3	82.1	-6.242
4	89.3	-5.877
5	95.2	-5.600
6	100.6	-5.360
7	100.4	-5.369
8	103.1	-5.253
16	104.2	-5.207
17	88.9	-5.897
-	-	-
30	72.0	-6.813
31	58.5	-7.714
32	46.6	-8.702
Average (dBm)		-6.373

cm away to ensure that the power emitted from the aperture was completely captured by the detector. The input power from the laser (Keysight Tunable Laser Source) was 0.000 dBm (1.000 mW), the loss from the laser propagating up to and through the lensed fiber used for edge coupling was -2.232 dBm, while the edge coupling loss into the chip through one of the facets was measured to be -2.383 dBm. This resulted in a total setup and edge coupling loss of -4.614 dBm. The power from several of the ports was measured, shown in Table 2.1. The highest recorded power, 104.2 μW, was emitted from one of the two central ports, specifically port 16. The power from port 17 was likely reduced due to a small piece of dust near one of the waveguides. As can been seen from the table, there is a $\sim$ 20-55% dropoff in optical power for the three waveguides at both ends of the focal arc. This is possibly due to some misalignment of the port to the lens and could also be due to some coma and spherical abberations present as the off-axis light sources enter the lens.

2.5.3 8 Port Planar Lens:

All Electronic Beam Steering

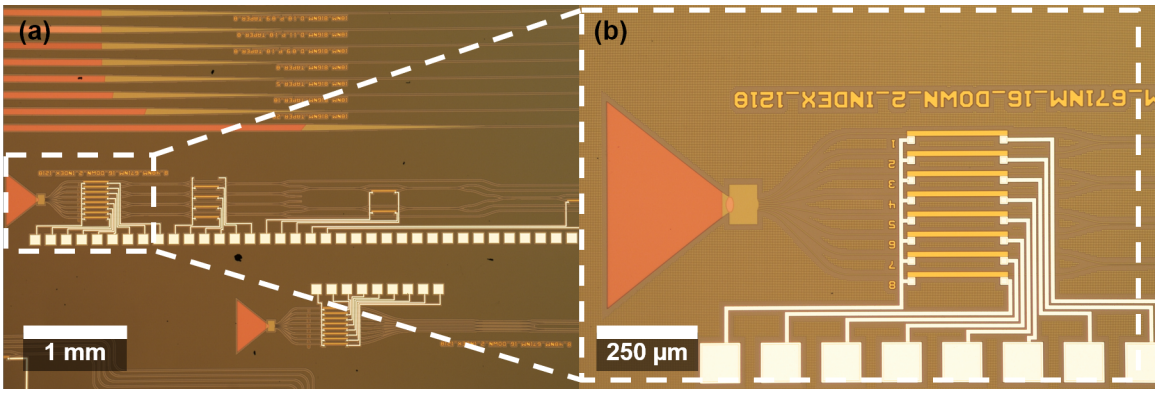

Figure 2-10: Optical microscope image of a 8 port device with an MZI tree. (a) The MZI tree has thermo-optic heaters using TiN resisitive heater elements. The average power required for a π phase shift was 193 mW. (b) Zoom-in of the lens and grating. An array of 8 Si_3N_4 waveguides feed into a single aplanatic planar lens. The grating coupler has a pitch of $\Lambda = 671$ nm and duty cycle $d = 0.776$. The lens was designed with a normalized effective index ratio of $n_1/n_2 = 1.210$. A maximum lens diameter of 37 μm was chosen so that it could take inputs from the 8 waveguides at a 4 μm spacing along the focal arc.

An 8 port device with a MZI-based tree for port selection was also tested. The thermo-optic heaters were fabricated on top of the previously mentioned dielectric stack using TiN resisitive heater elements with Ti/Al interconnect metals, Fig. 2-10(a). For more information of this platform see [15]. The average power required for a π phase shift and consequently switching from one port to the other was 6.2 V x 31.18 mA = 193 mW. This device had dielectric layers estimated to be Si_3N_4 slab = 210 nm and a:Si = 51.9 nm (with an additional 9 nm of SiO_2 overcladding sandwiched in-between the two layers due to an inadvertently shortened chemical mechanical polishing process). The effective indices $n_1 = 1.94$ and $n_2 = 1.59$ were modeled via a Finite-Difference Eigenmode (FDE) solver. The lens was designed with a maximum diameter of 37 μm to accommodate the 8 waveguides feeding the lens along the focal arc. Due to the shorter focal distance, the lens was designed with a target normalized effective index ratio of $n_1/n_2 = 1.210$, Fig. 2-10(b). The higher index ratio allows for the greater accumulation of phase inside the lens and leads to the desired refraction through the

lens. The grating had a length of 282 μm, pitch Λ = 671 nm, and duty cycle d = 0.776 for region n_1.

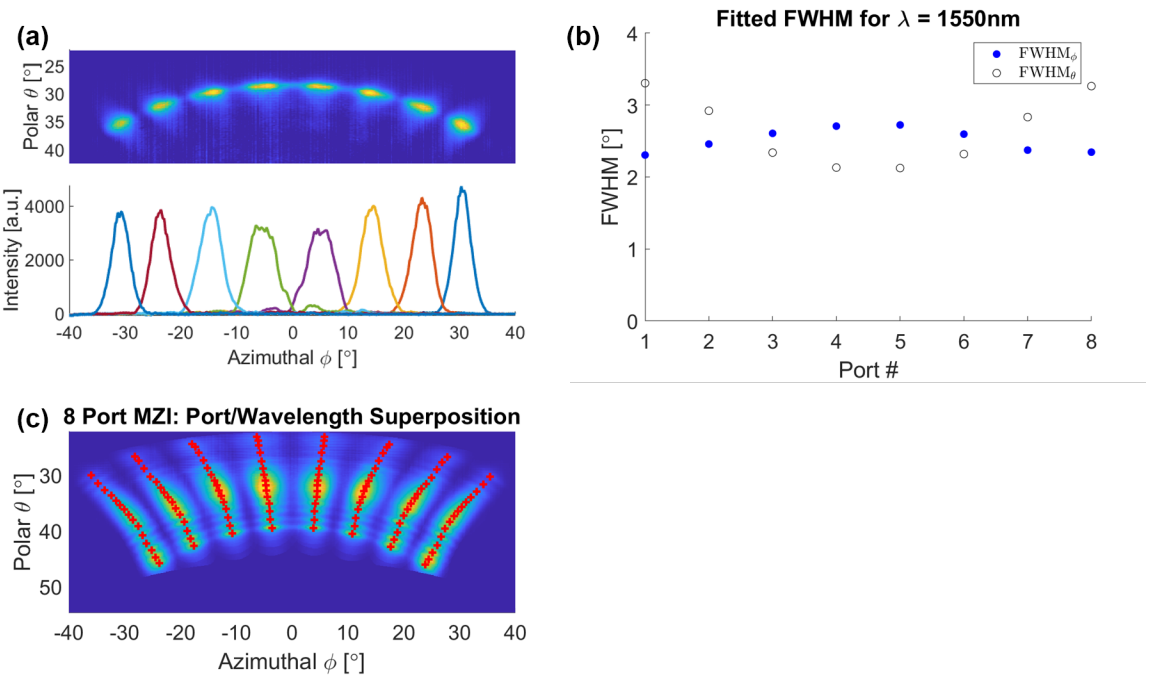

Figure 2-11: Experimental results from the fully integrated 8 port MZI beam-steering architecture. (a) Azimuthal scanning range and far-field beam cross-sections for the 8 port device. (b) FWHM of the far-field beams shown in (a), wavelength is held constant at λ = 1550 nm. (c) Digital superposition of the images recording the 8 far-field beams emitted from the planar lens architecture (using a range λ = 1500-1640 nm at an interval of 10 nm). The centers of each beam are designated with a red cross. Port switching is conducted via phase shifters that control the MZI tree and consequently selects the waveguide feeding the planar lens.

The azimuthal scanning range is 61.3 ° from ϕ = (30.4° to -30.8°) with a mean angle step increment of $\overline{\Delta\phi}$ = 8.74° via port switching, Fig. 2-11. The polar angle range is 16.3° from θ = (23.2° to 39.5°) with a mean angle step increment of $\overline{\Delta\theta}$ = 0.582 ° every 5 nm using wavelength tuning from 1500-1640 nm. Using the geodesic framework, the FOV is 34.1° by 16.3° in the in-plane and out-of-plane directions respectively.

The full width at half max (FWHM) of the beams shown in Fig. 2-11(b) was fitted in both the azimuthal (ϕ) and polar (θ) direction for all the ports (λ = 1550 nm). Since the 8 port device has a larger beam divergence and spreads the optical power

of the beam over a larger cross-section, an input power P_0 of 6.990 dBm (5 mW) was used for the beam steering demonstration and the FWHM analysis. Superposition of the optical beams emitted from all 8 ports is shown in Fig. 2-11(c). The average measured FWHM of the major axis of the 8 beams is 2.51°, which is the same order of magnitude as the approximation $\lambda/\mathrm{D} = \frac{1.550\mu m}{37\mu m} = 2.40°$ where D is the diameter of the lens. The average measured FWHM of the minor axis is 2.65°, compared to the $\lambda/\mathrm{D} = \frac{1.550\mu m}{26\mu m} = 3.42°$. The beams have a larger FWHM than the 32 port device since the lens diameter was ~ 4 times smaller and the effective grating length of 26 μm (simulated via FDTD) was ~ 3 times smaller as well. The optical power emitted from all 8 ports was also measured. To compare the output power values to the 32 port device, an input power of 0.000 dBm (1 mW) was used for the measurements in Table 2.2. The lowest power recorded, 14.08 μW for port 5, was no more than 30.54% less than the maximum power recorded, 20.27 μW for port 2. As opposed to the 32 port device, in this case, the central ports of the 8 port device provided less power in the far-field. The most likely contributors to lower power emission were sub-optimal port placement and lens curvature during the design phase.

Table 2.2: Power measurements for 8 port MZI device, after taking into account setup loss.

Port #	**Output (μW)**	**Output (dBm)**
1	18.39	-12.74
2	20.27	-12.32
3	16.93	-13.10
4	14.54	-13.76
5	14.08	-13.90
6	16.60	-13.18
7	18.02	-12.83
8	19.40	-12.51
Average (dBm)		-13.04

2.6 Planar Lens Architecture Advantages

This planar lens architecture has several benefits. First, although the current system is restricted to using a thermo-optic phase shifter to operate the MZI switch tree, only a sub-set of the switches are used simultaneously to steer the optical beam. This is important because as shown in the literature, using thermo-optic phase shifters exacerbates the power budget and electronics required to operate an OPA. Since the power required to operate a phase shifter is $\frac{dT}{dn}\sigma$, where $\frac{dn}{dT}$ is the thermo-optic coefficient and σ is the conductivity, the thermo-optic coefficients of Si_3N_4 and Si, 2.45 x 10^{-5} K^{-1} and 1.86 x 10^{-4} K^{-1} respectively, become important factors [56, 57, 58]. This lens-based architecture only requires $\log_2(N)$ phase shifters to be on at any given time, where N is the number of ports and equivalent number of resolvable points in the far-field. To accomplish a 45° field of view with a 0.05° beam width in the azimuthal direction (comparable to the OPA systems summarized in Chung et al. [21]), a lens-based architecture will require on the order of 1000 waveguides to feed the lens and consequently will have 1000 resolvable points in the far field. For a similar aperture size, this planar lens-based architecture will require $\sim$ 10 times less power compared to a standard OPA based approach. Second, this approach does not need to actively control hundreds to thousands of elements at the same. Instead, the binary switching of the MZI is used to route the light to the appropriate port and does not require a closed-loop algorithim to steer the beam. Moreover, by reducing the number of active thermo-optic phase shifters, the thermal cross-talk and heat dissipation issues can also be reduced. Lastly, another benefit that arises from our architecture is the ability to handle higher amounts of optical power. Since the maximum IR power a single Si waveguide can handle is limited due to non-linear absorption [59], Si_3N_4 becomes an interesting alternative since it has been reported to sustain $\geq$1 W through a single waveguide, as recently demonstrated [60]. Using Si_3N_4 could lead to lens-based architectures where high power handling is required at every stage of the device.

2.7 Experimental Results: Photonic Loss

When designing a photonic device, it is desirable to reduce on-chip photonic losses as much as possible so that the overall optical power required of the input laser is kept to below 100 mW since this is the range for available lasers [61, 62]. Moreover, as will be discussed in Chapter 4, for a lidar system the free space loss at 200 m is significant and unavoidable, and requires the mitigation of the on-chip photonic losses. The first set of losses that must be measured is the material loss for Si_3N_4 and a:Si, irrespective of the photonic structure. Lastly, the losses due to edge coupling the laser to the chip are also determined so that those values can be distinguished and separated from the loss due to either the intrinsic material or the design of the device.

2.7.1 Silicon Nitride

The optical loss of the Si_3N_4 was determined by using a linear-regression-based loss-extraction model for an all-pass ring resonator demonstrated by Deng el al. [63]. The linear regression is done to enhance the reliability of the extracted losses since alternative methods such as the extinction-ratio-based model and the finesse-based model are susceptible to experimental setups. They are especially susceptible during critical coupling conditions for a ring resonator [63]. The model works by transforming the transmission spectrum of the ring into a linear relationship without any additional approximations so that a linear regression can be performed to accurately extract the loss coefficients and calculate the propagation loss. The variables used for the linear regression are the incident optical power (P_0), the self-coupling coefficient (r) for a ring resonator, the cross-coupling coefficient (κ) for a ring resonator, and the round trip loss of the optical field (α) within the ring [64]. The round trip loss of the field is directly related to the round trip loss of the optical power via the equation Loss (dB) = -10 $log_{10}(\alpha^2)$. The round trip phase change θ can be expressed as

$$\theta = 2\pi \frac{n_{eff}(\lambda)L}{\lambda} = 2\pi m \tag{2.4}$$

where n_{eff} is the effective refractive index, L is the round-trip path length, λ is the wavelength of operation, and m is an integer. Moreover, the derivative of m with respect to λ is $dm/d\lambda = -n_g L/\lambda^2$, where $n_g = n_{eff}(\lambda) - \lambda \partial n_{eff}/\partial\lambda$ is the group refractive index. When m is an integer, λ is a resonance wavelength for the ring. Assuming an integer corresponds to each resonance wavelength λ_n then a linear regression can be performed using the linear relationship

$$n = n_g L \left(\frac{1}{\lambda} - \frac{1}{\lambda_0} \right) \tag{2.5}$$

For the all-pass ring used herein, the linear relationship above can be used to extract the constants $r \cdot \alpha$. Additional relationships between r and α are used to determine two roots (S_1) and (S_2) which directly correspond to both r and α. The two roots and thus coefficients can be distinguished by testing multiple devices with slightly different coupling states such that during under-coupling of the ring ($r > \alpha, \alpha = S_2$ and during over-coupling ($r < \alpha, \alpha = S_1$). The final step of the procedure is the following:

1. Set the initial power $P_0 = T_{max}$ which is the max transmission out of resonance.
2. Calculate S_1 and S_2.
3. Update P_0 according to the equation

$$P_0 = T_{max} \left| \frac{1 + S_1 S_2}{S_1 + S_2} \right|^2 \tag{2.6}$$

for the next iteration of the linear regression.

For these particular devices, a ring resonator with 13 resonance peaks was measured within the λ range 1536-1564 nm, Fig. 2-12. Using the linear regression above, the extracted loss coefficient of the ring, α, was averaged to be 0.998. This provides a loss of 0.278 dB/cm at $\lambda = 1550$ nm, Fig. 2-13.

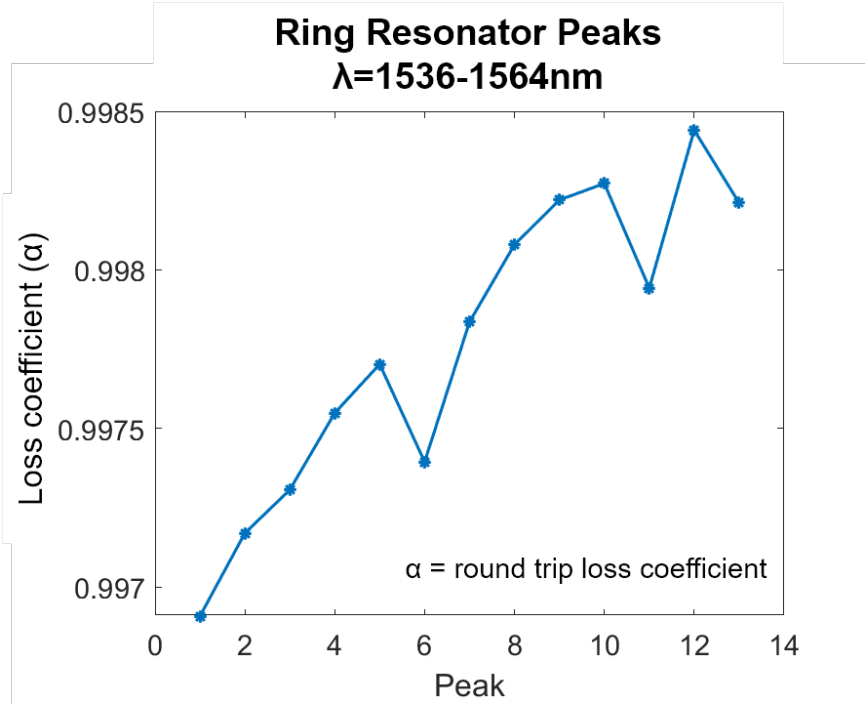

Figure 2-12: Plot of the extracted loss coefficients for 13 individual resonances determined via the linear-regression loss-extraction model.

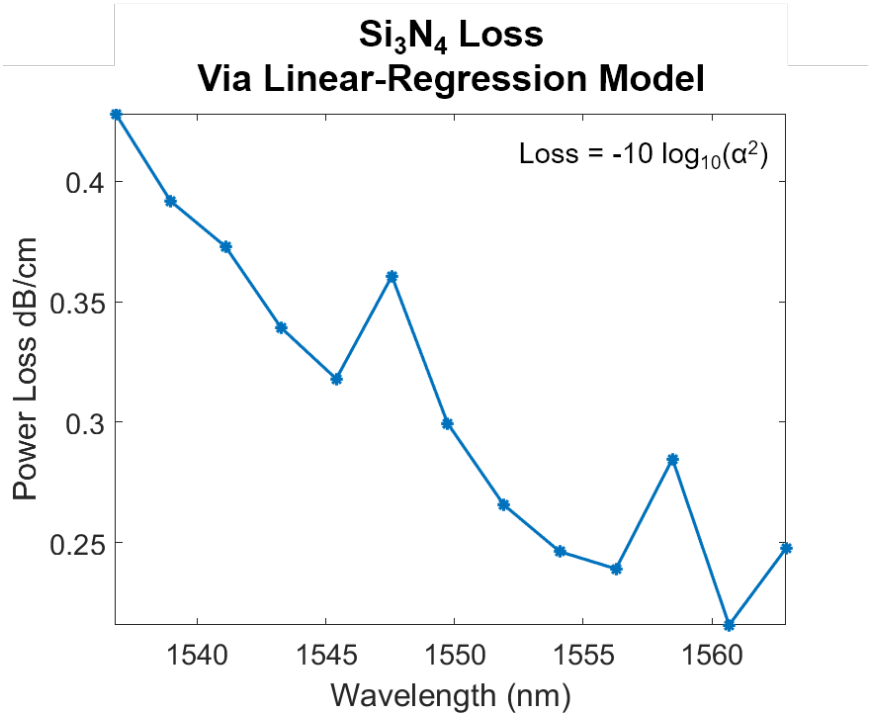

Figure 2-13: Plot of extracted loss (dB/cm) determined via the linear-regression loss-extraction model. A loss of 0.278 dB/cm is calculated at $\lambda = 1550$ nm (using an input laser Power $P_0 = 0.000$ dBm).

2.7.2 Amorphous Silicon

The optical loss in the amorphous silicon was determined by measuring a series of paperclip structures of increasing total length, from 1 to 4 cm. Each paperclip has an identical number of bends and a minimum bend diameter of 300 μm was set such that the radiation loss is negligible. The loss was extracted from the slope of the linear fit of the output power, in dBm, versus waveguide length [65], providing a loss for the 24.5 nm a:Si of 0.779 dB/cm at $\lambda = 1550$ nm (and $P_0 = 0.000$ dBm), Fig. 2-14, and a loss for the 51.9 nm a:Si of 4.427 dB/cm at $\lambda = 1550$ nm (and $P_0 = 0.000$ dBm).

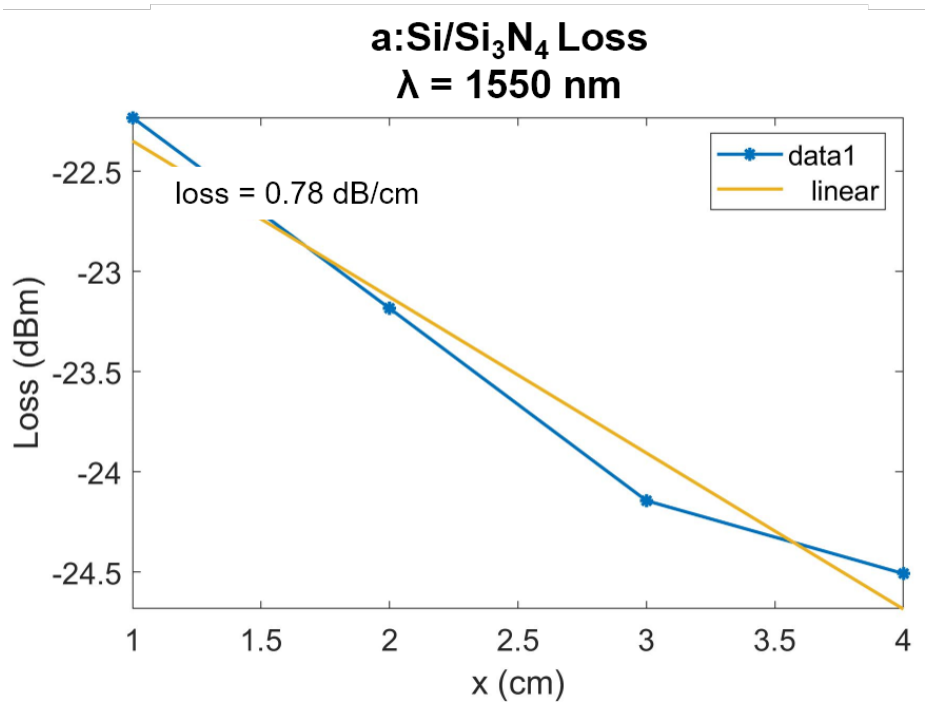

Figure 2-14: Plot of the a:Si loss based on paperclip measurements. The slope of the linear regression is the estimated loss 0.779 dB/cm for $\lambda = 1550$ nm.

2.7.3 Coupling Losses

The TE polarization in the waveguide was set through a three paddle fiber polarization controller. The loss of edge coupling through one facet was determined to be -2.383 dB (after taking into account material/device and setup losses).

2.8 Comment on Simulating a Linearly Apodized One-Dimensional Grating and Estimating the FWHM

Theoretical analysis of the expected optical beam emitted from a 1D grating can be done by using a FDTD simulation and placing a power and electric field monitor that records the electromagnetic fields emitted from the grating [66, 67]. The monitor can record the near-field profile of the electric field propagating and decaying along the grating and then project it into the far-field via a Fourier Transform. The emission from a standard linear apodized grating will have an exponential decay profile proportional to e^{-ax} where a is decay constant and defined as $a = 1/L$ where L is the decay length.

The following Fourier Transform can be shown for the following exponential function, which is the known form of a Lorentzian Function where Γ is by definition the FWHM of the Lorentzian centered at $x_0 = 0$.

$$\mathcal{F}_x[e^{-\pi\Gamma|x|}](k) = \frac{1}{\pi}\frac{\frac{\Gamma}{2}}{(x-x_0)^2 + (\frac{\Gamma}{2})^2}, \text{where } x_0 = 0 \tag{2.7}$$

Jain et al. [68] have also shown that a Lorentzian curve can be fitted to a linearly scaled version written as

$$\frac{1}{\pi}\frac{A\Gamma}{2}\frac{\frac{\Gamma}{2}}{(x-x_0)^2 + (\frac{\Gamma}{2})^2}, \text{where } x_0 = \text{center of the peak} \tag{2.8}$$

and A is the max amplitude at the center of the peak. Using the MATLAB function 'lorentzfit' written by Jered Wells [69], a Lorentzian curve and thus the FWHM for each optical beam in the far-field can be estimated. Using this fitting procedure, the following are the estimates for the FWHM of the minor-axis of the optical beams (which is dependent on the grating). The 32 port device has an estimate of 0.2351 degrees. The 8 port device has an estimate of 0.6738 degrees. These values are consistent with the effective length estimated from the 1/e decay of each simulation. However, they are at least ~ 3.5 times smaller than the experimental values extracted

from the IR images. This leads to believe that the FWHM along the major and minor axes of each beam are likely not independent of each other and that the grating and lens both have an effect on the overall beam profile and far-field cross-sections. Note that it would be necessary to use 3D simulations to understand the combined effect of the grating and lens on the optical beam since the electromagnetic waves propagating through the chip would also need to be simulated being emitted and propagating in free-space.

2.9 Future Work and Improvements

There are two design choices that can improve the performance of the planar-lens based architecture. One alternate realization of this system is to eliminate most or all of the thermo-optic phase shifters and parallelize the feeding of the light source to multiple ports at the same time. By exciting several ports simultaneously, the lens could steer multiple beams. This configuration is commonly used in commercial lidars to increase the scanning rate.

Future work on this optical beam-steering platform can include exploring the literature of planar lens solutions, such as Luneburg lenses [70, 71]. Additional work can be done to address the curved raster lines and rotating optical beams by designing a curved grating that can appear the same to the propagating slab mode regardless of the angle of the waveguides feeding the lens as recently demonstrated by Doerr et al. [72]. In conclusion, this chapter has experimentally demonstrated the first optical planar-lens-enabled beam steering PIC which opens up new avenues for wide-field-of-view optical beam steering applications such as lidar and optical communication links.

Chapter 3

Planar Luneburg Lens Architecture for Optical Beam Steering

Although the planar lens architecture reduces the electronic complexity required for beam steering, the aplanatic lens is based on the paraxial ray approximation and has a field of view (FOV) limit of +/- 20° [27]. To address the FOV limits of the aplanatic lens design, inspiration can be drawn from gradient refractive index (GRIN) lenses which use an index of refraction that varies smoothly along the lens. Of specific interest is a Luneburg lens which is radially symmetric and has a gradient in the refractive index that decreases radially from the center to the edge of the lens, Fig. 3-1(a). The simplest solution was shown by Luneburg and allowed for two conjugate foci at the outside edge of the lens and demonstrated an abberation-free and coma-free lens [73]. Over the years, different variations of Luneburg lenses have been theoretically proposed [74, 75, 76]. Falco et al. [75] and Takahashi et al. [77] experimentally demonstrated a Luneburg lens using e-beam lithography, Fig. 3-1(b). Even though all of these reports demonstrated the potential of a Luneburg lens for the on-chip steering of light, none of them had been demonstrated using a scalable fabrication process. Moreover, no one had yet proposed a Luneburg lens architecture for two-dimensional optical beam steering over a wide field of view.

In this chapter, a planar Luneburg lens architecture for two-dimensional optical beam steering is experimentally demonstrated. The Luneburg lens replaces the apla-

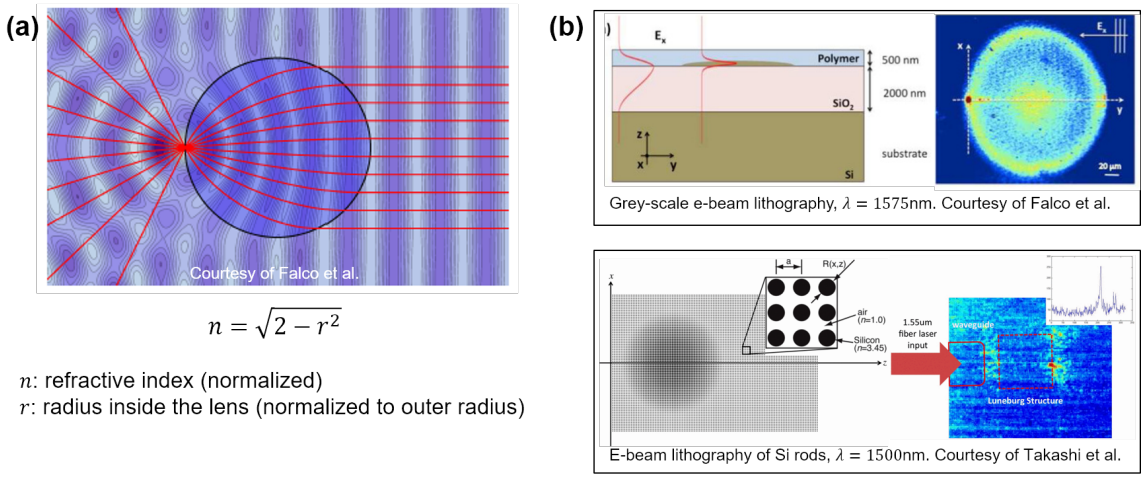

Figure 3-1: Prior theoretical and experimental demonstrations of Luneburg lenses operating at 1550 nm. (a) A Luneburg lens is a circularly symmetric design with a gradually varying refractive index that is a function of the radius. The simplest design was presented by Luneburg where a collimated wavefront is focused on a point at the surface of the lens. (b) Prior Luneburg lenses were fabricated using e-beam lithography. Adapted from Falco et al. [75] and Takahashi et al. [77].
© 2011 Optical Society of America. © 2010 IEEE.

natic lens in the previous chapter and overcomes the FOV limitations, Fig. 3-2(a). The radially symmetric lens is paired with a radially concentric grating for coupling into free-space. As previously shown, light from a tunable laser is fiber-coupled into a Si_3N_4 waveguide which feeds into a switch matrix. The switch matrix routes the beam to one of N waveguides by actively using only $\log_2 N$ phase shifters. The N waveguides are placed on an arc concentric with the lens. The routed beam then feeds into the planar Luneburg lens, which collimates the beam, Fig. 3-2(b). The collimated light is then scattered out-of-plane by a circular grating coupler. Switching the waveguide determines the angle at which the slab mode enters the lens, steering the in-plane beam angle ϕ. Tuning the wavelength steers the out-of-plane beam angle θ via the wavelength dependent (a.k.a. dispersive) properties of the grating.

To achieve the necessary gradient index, a photonic crystal consisting of 30 nm thick amorphous silicon (a:Si) patterned with a triangular lattice of holes and is deposited on top of a 200 nm thick silicon nitride (Si_3N_4) layer [78]. By slowly varying the hole size across the lens, the effective index n_{eff} of the photonic crystal is varied and realizes the gradient index of the Luneburg lens, Fig. 3-3(a). The lattice

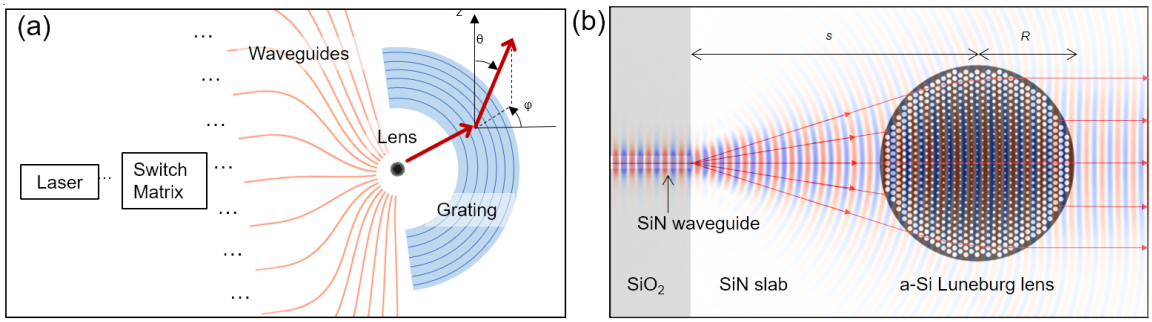

Figure 3-2: Schematic of planar lens architecture with a Luneburg lens and concentric circular grating. (a) A laser is fiber-coupled onto the chip. An MZI switch tree selects the waveguide that feeds the propagating optical mode to the lens. The Luneburg lens collimates the slab mode diverging from the waveguide-slab interface. The circular grating couples the light into free-space. (b) FDTD simulation of Luneburg lens collimating the slab mode. R is the radius of the lens and s is the focal distance. Adapted from Kim, López, et al. [30]

spacing of the hexagonal lattice is a = 400 nm and the hole diameter, d, is allowed to range from 100 nm to 300 nm to ensure compatibility with optical lithography. Choosing an a:Si thickness of 30 nm and a focal distance of three times the radius (R), $s = 3R$, allows the photonic crystal to achieve most of the desired index profile.

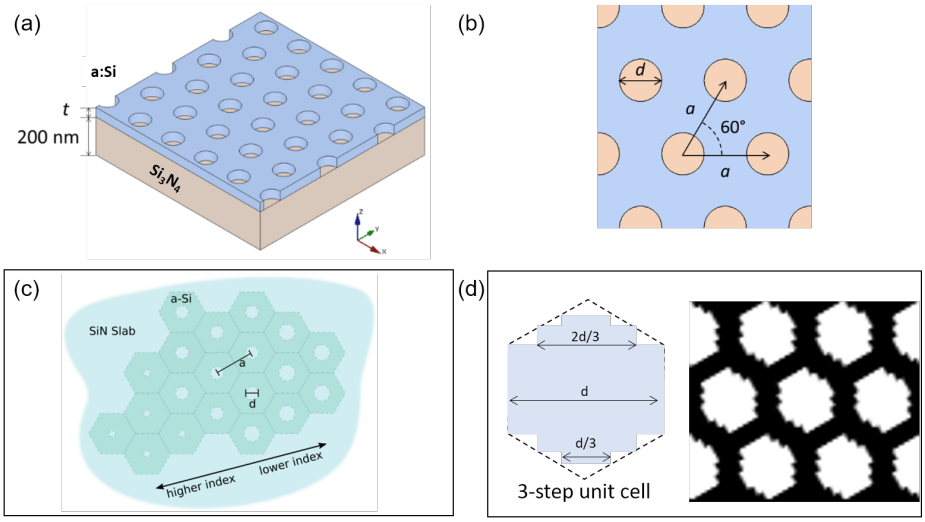

Figure 3-3: (a) Cross-section of the Luneburg lens, 30 nm of a:Si is deposited on top of 200 nm of Si_3N_4. (b) Luneburg lens uses a triangular lattice. The refractive index is controlled via the center to center distance, a, of each unit cell and the diameter of the nanoscale hole, d. (c) Schematic of index of refraction as a function of d. (d) To fabricate the lens using a wafer-scale lithography process, the lithography mask required the holes in the CAD layout to be designed using only 12 vertices and a 3-step unit cell. Adapted from Kim [78]

3.0.1 Single-Layer Grating

One of the metrics used for an optical beam steering system is the beam divergence of the emitted far-field. The smaller the beam divergence measured via the full width at half maximum (FWHM), the higher spatial resolution a lidar system can achieve. To reduce the beam divergence, the effective aperture emitting the beam must be increased. There are several grating designs that have achieved a large effective aperture via apodization of the grating fill-fraction [79, 80, 81, 82, 83].

In general, a grating is a periodic structure that scatters light into free-space by adding/subtracting momentum to the wave vector of light [84]. Fig. 3-4 demonstrates a standard grating design where the fill-fraction (ff), also known as the duty cycle, is defined as $ff = W/\Lambda$, where (W) is the width of a single tooth of the grating and Λ is the pitch of the grating. For all of the designs considered herein, the waveguide consists of a top cladding of silicon dioxide, a core consisting of a thin layer of a:Si (less than 50 nm) on top of a layer of Si_3N_4 ($\sim$ 200 nm), a 5 μm bottom cladding made of silicon dioxide, and a silicon substrate. The simplest design for this type of grating is a piecewise rectangular grating etched into the a:Si while keeping the Si_3N_4 slab planar waveguide unetched. The a:Si is etched because it is (i) easier to etch the thinner film and (ii) it has a higher refractive index than Si_3N_4 and will act as a perturbation to the local refractive index.

The scattering strength of a grating is determined by the difference between the effective index of the local background environment and the average effective index of the grating. Using a perturbative method, a.k.a. volume current method (VCM), the scattered radiation due to refractive index inhomogeneities can be calculated from the dielectric perturbation $\delta\epsilon\left(\overrightarrow{r'}\right) = -(\epsilon_1 - \epsilon_2) f(\overrightarrow{r'})$ which is used to determine an induced polarization current $J_p = -\omega\left(\epsilon_1 - \epsilon_2\right) f\left(\overrightarrow{r'}\right) E\left(\overrightarrow{r'}\right)$ and consequently the radiated field emitted in the far-field, where $f(\overrightarrow{r'})$ equals 1 in the volume and 0 otherwise [85]. This allows the individual teeth of the grating to be interpreted as elements of an antenna array.

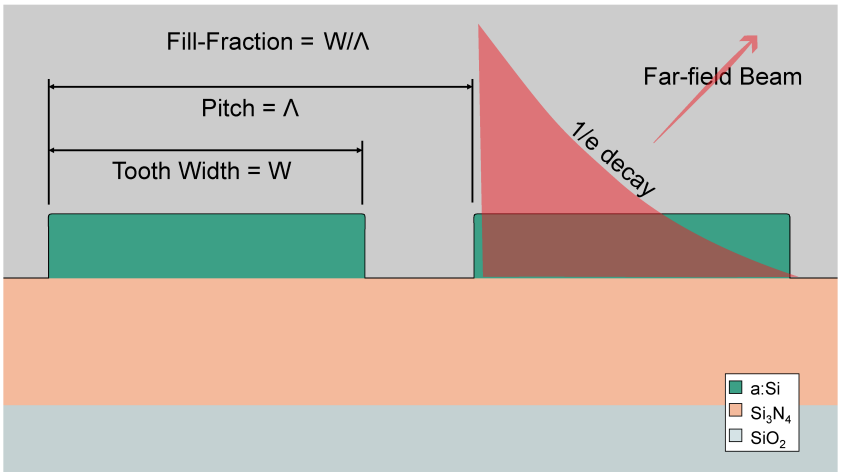

Figure 3-4: Cross-section of the grating showing the dielectric stack: top silicon dioxide cladding, a core consisting of a:Si on top of Si_3N_4, a 5 μm bottom silicon dioxide cladding. The silicon substrate is not shown. The width of the grating tooth is (W), the pitch (Λ), and the fill-fraction (ff) is the ratio W/Λ. The fill-fraction of the grating can vary between 0 and 1 and is limited by the feature limits. In this case, the largest height to width etching that can be maintained in either the a:Si and the Si_3N_4 layer is a 1:1 ratio.

The simplest method to creating a large optical aperture is by creating a grating with a weak perturbation to the slab mode propagating along the cross-section of the grating. Using the dielectric layer stack shown above in Fig. 3-4, the weak perturbation can be achieved by reducing the thickness and/or the fill-fraction of the grating. The lower limit to the ff is determined by the smallest feature size possible during the fabrication process. Using the 90 nm node lithography process at MIT Lincoln Laboratory (MIT LL), the smallest feature size is $\sim$ 100 nm [15]. It must be noted that the height to width ratio of the resulting structures also adds a constraint to the feature size. For the MIT LL process, the patterning limit of the Si_3N_4 layer is a 1:1 (height:width) ratio. For a 200 nm thick Si_3N_4 layer, this creates a lower limit feature size of 200 nm. To avoid hitting the physical limit and having any fabrication issues, a feature size of 220 nm was imposed for the Si_3N_4 layer. In contrast, the top a:Si film had a patterning limit of 100 nm since the thickness was $<$ 50 nm.

Grating: Fill-fraction and Thickness

Depending on the design, each layer of the grating can contain a fill-fraction that is constant or apodized throughout the length of the grating. For the initial phase of the grating design and exploration, a grating with a 660 nm pitch was simulated while choosing different values for the fill-fraction (ff) in the top a:Si layer ($\sim$ 30 nm thick). The Si_3N_4 layer was not patterned in this case. A wide range of fill-fractions was explored, ranging from $ff = 0.16$ to 0.84 which corresponded to a tooth width (W) ranging from 105 to 555 nm. Here a buffer of 5 nm was added to the 100 nm feature limit to avoid hitting the absolute limit of the lithography and etching process. In general, grating couplers with a constant grating fill-fraction will have an exponentially decaying emission profile. The goal of reducing the fill-fraction is to create the smallest index contrast relative to the local environment and engineer an overall weaker grating. A finite difference time domain (FDTD) simulation can include a power monitor at the top of the grating to measure the power emitted (proportional to E^2) into the far-field. Using the emission profile, the exponential decay constant and effective aperture can be estimated. The smallest ff possible for the a:Si, using the 100 nm feature limit, was $ff = 0.16$. By plotting E^2, the grating had a 1/e decay length of 175 μm, Fig. 3-5(a). The grating with $ff = 0.50$ had a decay length of 36 μm, Fig. 3-5(b). The grating with $ff = 0.789$ had a decay length of 96 μm, Fig. 3-5(c). Lastly, the grating with $ff = 0.84$, had a decay length of 147 μm, Fig. 3-5(d). As expected from the E^2 decay plots, the $ff = 0.16$ allowed for the largest effective aperture.

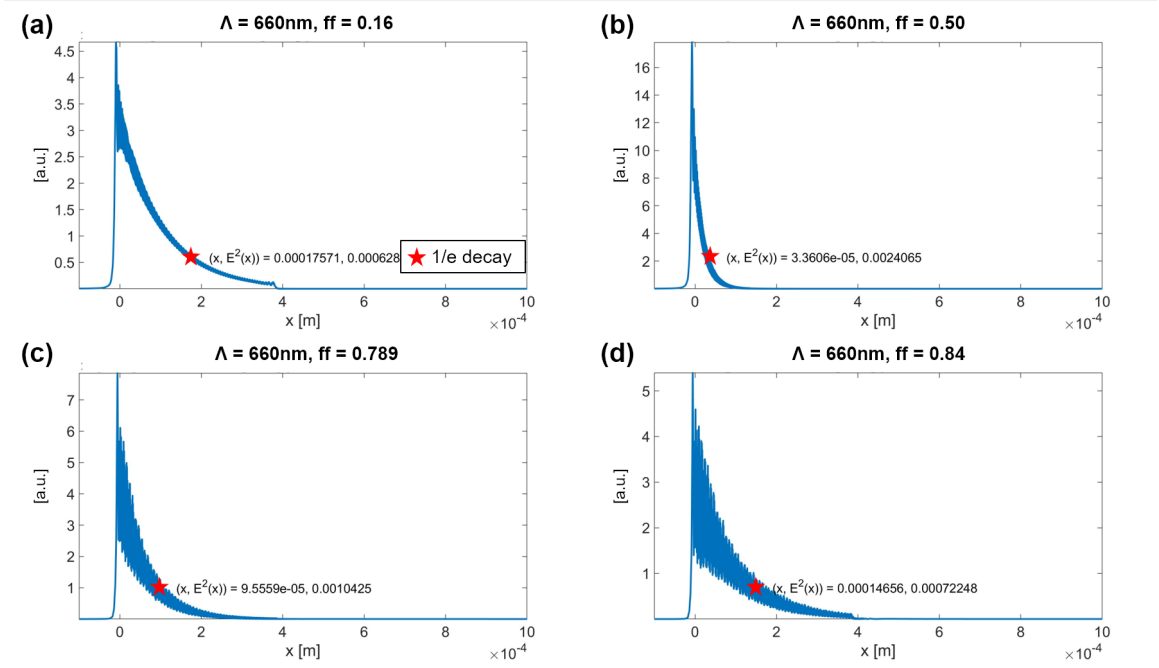

Figure 3-5: Plots of the simulated power emission profile, electric field squared (E^2), of the gratings as a function of distinct fill-fractions: $ff = 0.16, 0.50, 0.789, 0.84$. All gratings have a physical length of 400 μm, $\Lambda = 660$ nm, and an a:Si thickness of 30 nm. The red star marks the 1/e decay for the power. (a) $ff = 0.16$ has a decay length of 176 μm. (b) $ff = 0.50$ has a decay length of 36 μm. (c) $ff = 0.789$ has a decay length of 96 μm. (d) $ff = 0.84$ has a decay length of 147 μm.

Taking the results from the simulated fill-fraction study, the impact of grating thickness was explored to try to design the longest effective aperture. The set of designs explored were based on a 1 mm long grating with a:Si 10 nm thick and a fill-fraction ranging from $ff = 0.16$ to 0.84. For comparison, the difference between a grating that has $ff = 0.16$ and $ff = 0.50$ is shown next. As seen from Fig. 3-6(a), the grating with $ff = 0.16$, results in a 1/e decay length of well over a 1 mm and a resulting beam divergence angle of 0.1° as shown in Fig. 3-6(c). This is expected since the lowest fill-fraction allows for the least amount of perturbation in the permittivity (ϵ) and thus the lowest perturbation of the refractive index. The grating with $ff = 0.50$ results in a 1/e decay length of 362 μm and a beam divergence angle of 0.15°, Fig. 3-6(d). Both these gratings provide beam divergences that start reaching practical effective aperture lengths. It must be noted that the 10 nm thickness is hard to control because the deposition process can have variability of well over 1 nm (10%).

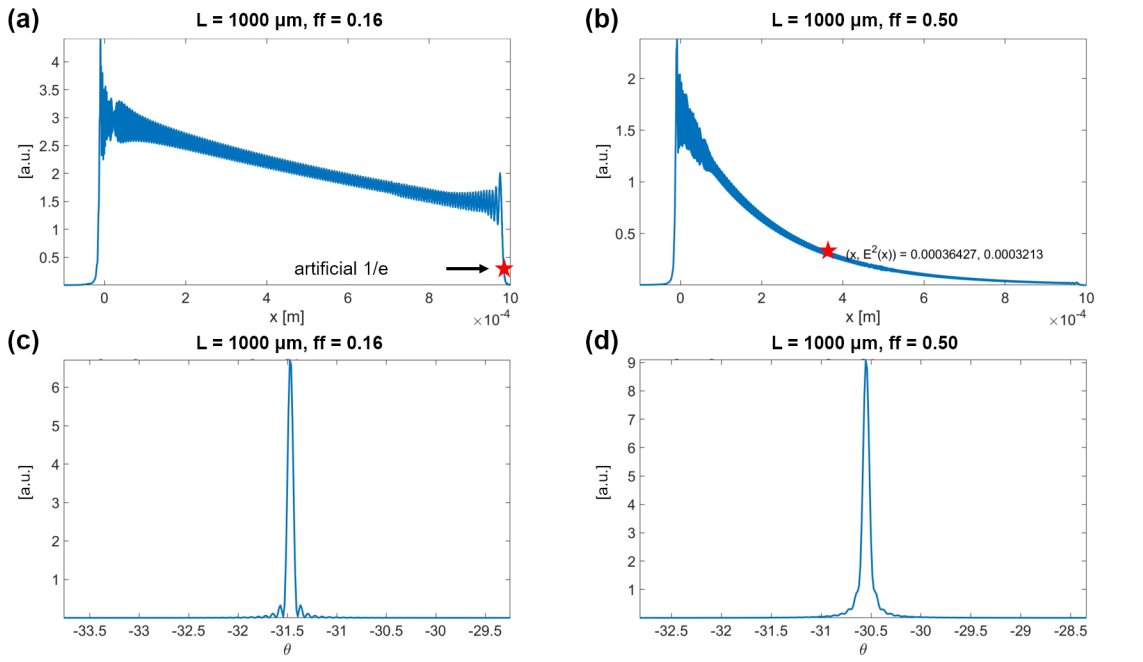

Figure 3-6: Simulated emission profile and beam divergence plots of gratings with $ff = 0.16$ vs $ff = 0.50$. The gratings are a single-layer with patterned a:Si on top of Si_3N_4. The length (L) of the grating is 1000 μm, $\Lambda = 660$ nm, and uses an a:Si thickness of 10 nm. The red star marks the 1/e decay for the power. (a) Emission profile for $ff = 0.16$. The 1/e marker is artificial in this case since the simulation dimension was not long enough to capture decay over the entire length of the grating. (b) Plot of the beam divergence in the far-field, showing a 0.1° FWHM. The center of the emitted beam is ∼ -31.6°. (c) Emission profile for $ff = 0.50$. (d) Plot of the beam divergence in the far-field, showing a 0.15° FWHM. The center of the emitted beam is ∼ -30.4°.

3.0.2 Double-Layer Grating

Normally a standard grating with no broken symmetry will emit downward radiation that is equal in power to the upward emission. In a grating design with a reflective substrate, in this case silicon, the downward emission will undergo multiple reflections between the bottom of the grating and the substrate. This effect can be understood as a Fabry-Perot cavity with a transmission response that varies with angle and also wavelength. A grating design that breaks the vertical symmetry in a grating structure can change the emission profile. Recent demonstrations have shown that a $\lambda/4$ displacement in both the horizontal and vertical direction is effective at unidirectional

emission since it achieves constructive interference on one side of the grating and deconstructive interference on the opposite side [82, 83].

Using both the $\lambda/4$ and apodization literature as inspiration, the approach used in this study was to break the symmetry of the grating by using two different grating layers with a $\lambda/4$ offset along the direction of propagation. The top and bottom layers are composed of different materials (a:Si and Si_3N_4) and cannot have a gap implemented between them because of the difficulty of controlling a SiO_2 gap during the fabrication process. Moreover, the gratings are apodized by either changing the ff linearly throughout the length of the grating or using a non-linear ff distribution. In this case, the non-linear distribution follows either a half or full Gaussian distribution function.

3.0.3 Grating Apodization

The goal of the apodization is to create a smoother transition in the effective index between the region with only Si_3N_4 and the region with a:Si on top. All the test gratings had a physical length of 100 μm, and unless otherwise noted, had a:Si 30 nm thick and a Si_3N_4 200 nm thick. Both the linear and half-Gaussian apodized gratings had a $\text{ff}_{\text{start}} = 0.38$ and $\text{ff}_{\text{end}} = 0.62$ while the full Gaussian distribution grating layers had $\text{ff}_{\text{start}} = 0.38$, $\text{ff}_{\text{middle}} = 0.62$, and $\text{ff}_{\text{end}} = 0.38$

Linear Apodization

A linearly increasing or decreasing apodization function can be applied to the layers of the grating. Fig. 3-7(a) shows the cross-section of a double-layer linearly apodized grating with the top layer shifted with respect to the bottom layer. To create the smoothest transition, the linear apodization for the Si_3N_4 layer decreases from the highest to lowest fill-fraction value. In contrast, the linear apodization for the top a:Si layer increases from the lowest to highest fill-fraction to create the smoothest transition in the refractive index. The increase in $ff(x)$ for the a:Si also increases the strength of the grating over its length. This double-layer structure with linear

apodization results in a simulated average transmission of 91.5% in the upward direction, as shown in Fig. 3-7(b).

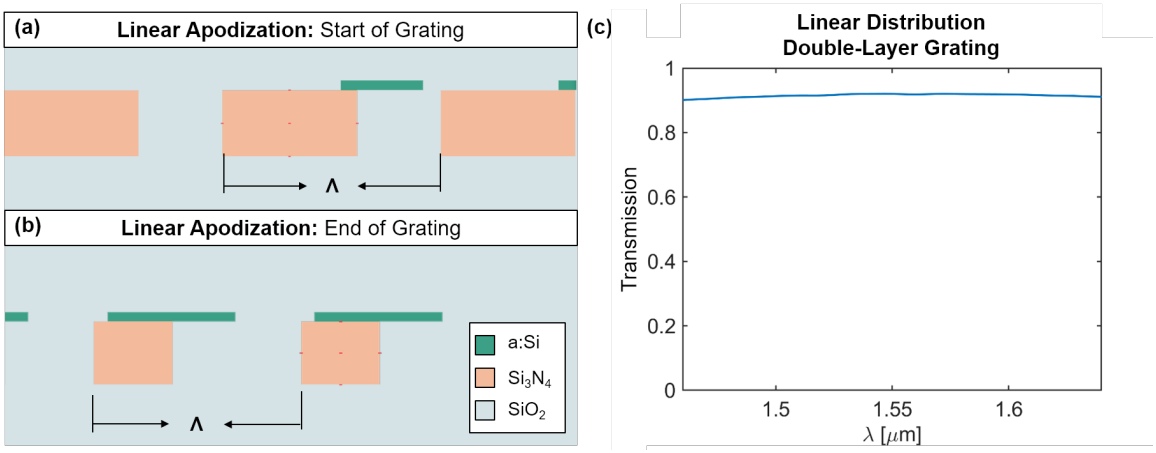

Figure 3-7: Simulation for linearly apodized double-layer grating with the top layer a:Si offset by $\sim \lambda/4$. (a) Cross-sections of the start and end of the grating. The top (a:Si) layer is increasing linearly in fill-fraction while the bottom (Si_3N_4) layer is decreasing linearly in fill-fraction. (b) The linearly apodized double-layer grating creates constructive interference in the upward direction and destructive interference in the downward direction. The grating has a simulated average simulated transmission in the upward direction of 91.5%.

Half and Full Gaussian Apodization

A second approach took inspiration from the Gaussian apodization by Waldhäusl [86]. To avoid the more intricate feedback loop algorithm, the design process was simplified by implementing a Gaussian apodization without an integration term. This simplified apodization was due to time constraints placed on the design process. A Gaussian distribution can be implemented by using either a half or full Gaussian distribution of the fill-fraction along the length of the grating. The general equation of a Gaussian distribution is shown below. The limits of the Gaussian function are set by determining the highest and lowest fill-fractions possible in either of the grating layers: $ff\,(x) = f_{start} + \{f_{end} - f_{start}\}\, e^{\frac{-(x-\mu)^2}{2\sigma^2}}$. The mean is $\mu = 0$ and the normalized distribution of the input x ranges from -3 to 3. This provides a theoretical range between 0.0 and 1.0 for the fill-fraction. The fill-fraction distribution can be discretized for any number of grating teeth. This discretization provides the fill-fraction for each

tooth of the grating. In addition, by holding all other variables constant and varying the σ^2, the apodization of the grating can be further engineered by either broadening or sharpening the Gaussian distribution. In this case σ^2 was equal to 1 for all designs. The practical low and high limit for the fill-fraction are determined by the fabrication constraints used in the lithography process. For the MIT LL process, it is constrained to 220 nm for the Si_3N_4 slab and 100 nm for the a:Si. To keep things simple during the parameter sweep, a lower limit of $ff = 0.38$ and upper limit of $ff = 0.62$ was implemented for the fill-fraction of both layers.

Here is an example plot of the fill-fraction distribution where $ff(x)$ is the function that determines the ff along the grating, where x is the axis along the length of the grating. Fig. 3-8(a) shows a half-Gaussian distribution function that is increasing while Fig. 3-8(b) shows a full Gaussian distribution that is symmetric. For the full Gaussian, the lowest fill-fraction value is used at the start and end of the grating. The highest fill-fraction value is used in the middle.

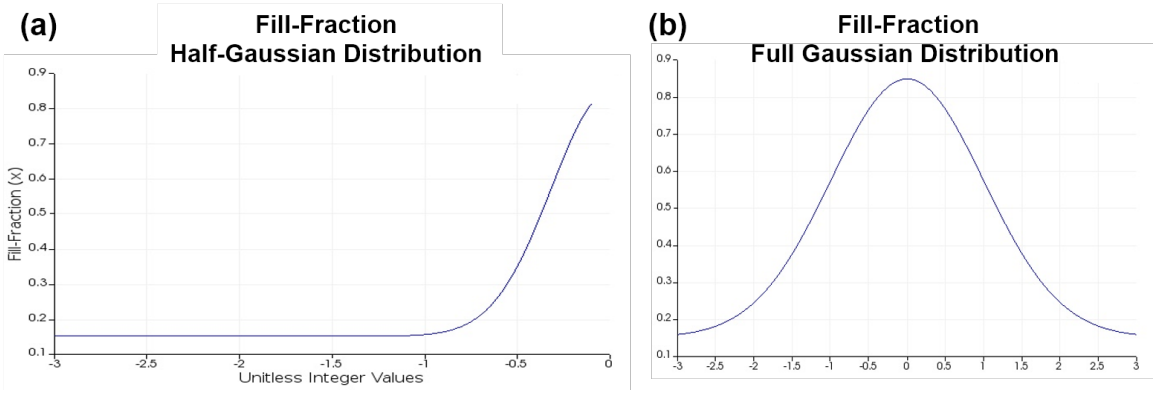

Figure 3-8: Plots of two different Gaussian apodization profiles. (a) Half-Gaussian distribution function that is increasing in amplitude from $ff = 0.16$ to $ff = 0.84$. (b) Full Gaussian distribution that is symmetric along the length of the grating. The lowest fill-fraction value is used at the start and end of the grating. The highest fill-fraction value is used in the middle. The x-axis has unitless integer values which are mapped to the physical start and end of the grating (start = -3 and end = 3).

Fig. 3-9(a) shows a half-Gaussian apodization for the bottom Si_3N_4 layer that decreases from high to low fill-fraction in the refractive index. The half-Gaussian apodization for the top a:Si layer increases from low to high fill-fraction in the refractive index. This double-layer structure with linear apodization results in a simulated

average transmission of 91.7% in the upward direction, as shown in Fig. 3-9(b).

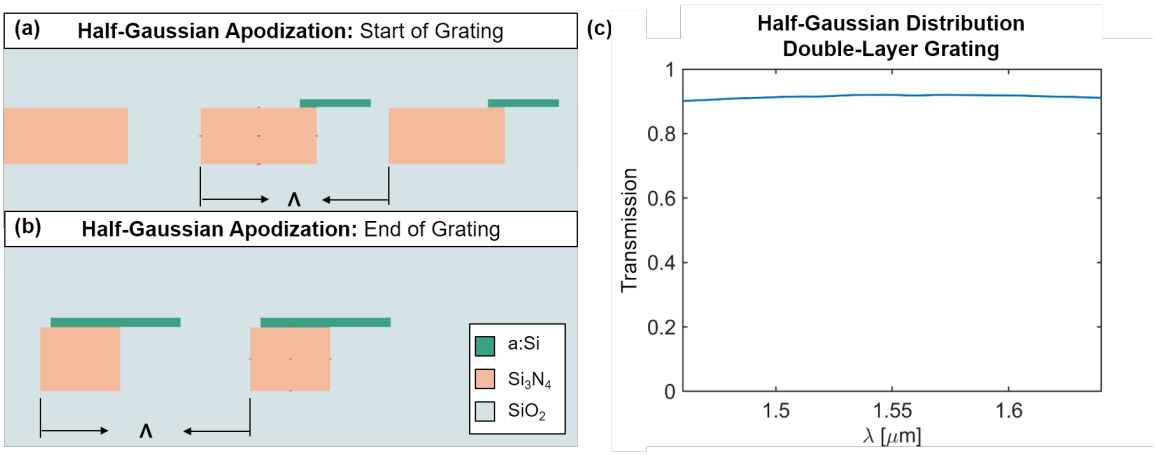

Figure 3-9: Simulation for half-Gaussian apodized double-layer grating with the top layer a:Si offset by $\sim \lambda/4n$. (a) Cross-sections of the start and end of the grating. The top a:Si grating is increasing in fill-fraction using a half-Gaussian distribution while the bottom Si_3N_4 grating is decreasing in fill-fraction using a half-Gaussian distribution. (b) The half-Gaussian apodized double-layer grating creates constructive interference in the upward direction and destructive in the downward direction. The grating has an average simulated transmission in the upward direction of 91.7%.

Apodization Type	Pitch Λ (nm)	Start Radius (μm)	FWHM (°)	Upward Transmission (%)	Effective Aperture (μm)
Linear 1	660	196	0.91	89.2	37.0
Linear 2	660	104	0.99	91.5	42.1
Half-Gaussian 1	660	104	1.29	91.7	37.0
Half-Gaussian 2	660	196	0.99	87.5	28.8
Full Gaussian	660	196	2.12	77.5	24.1

Figure 3-10: Table with the parameters and simulated performance for five double-layer grating designs. Includes the apodization type, pitch start radius, and resulting beam divergence, upward transmission, and effective aperture.

Fig. 3-10 contains the parameters and results for the final grating designs simulated. The table shows the type of apodization (linear, half-Gaussian, or full Gaussian). There was more than one linear and half-Gaussian apodization design fabricated and tested. They were named as Linear 1 or 2 and Half-Gaussian 1 and 2 respectively. The grating design parameters considered were the pitch (Λ), grating length (L), the start radius of the grating (R_g), and the fill-fraction (ff) start and stop values of both layers. The resulting performance metrics for the grating listed in

Fig. 3-10 are the FWHM at 1550 nm, average transmission in the upward direction, and effective aperture length. Additional details are in subsection 3.0.4.

Once a particular apodization was chosen, the design sweep is done by holding all grating features constant except for the relative shift between the two layers. The relative position of the top a:Si layer to the bottom Si_3N_4 layer was incremented by 10 nm during the sweep. Both the 1/e decay length and the resulting FWHM of the far-field beam were used to evaluate the grating design. The linearly apodized gratings had a decay length of $\sim$ 40 μm. The half-Gaussian gratings had a decay length of between $\sim$ 30-40 μm. Interestingly, the grating with a full Gaussian apodization had a decay length of $\sim 25\mu$m, which is the shortest decay length. This can be attributed to a faster variation of the ff over the same length, creating stronger perturbations for the refractive index and consequently stronger scattering into the far-field. The average transmission in the upward direction for both the linearly and half-Gaussian apodized gratings all averaged around 90 percent at $\lambda = 1550$ nm.

As can be seen in Fig. 3-11(a)-(d), the FWHM of the simulated emitted beam for both the linearly and half-Gaussian apodized gratings ranged between 0.91-1.29°. The shape of the far-field beam produced by the full Gaussian apodization was broader than the others and translated to a FWHM of 2.12°, Fig. 3-11(e).

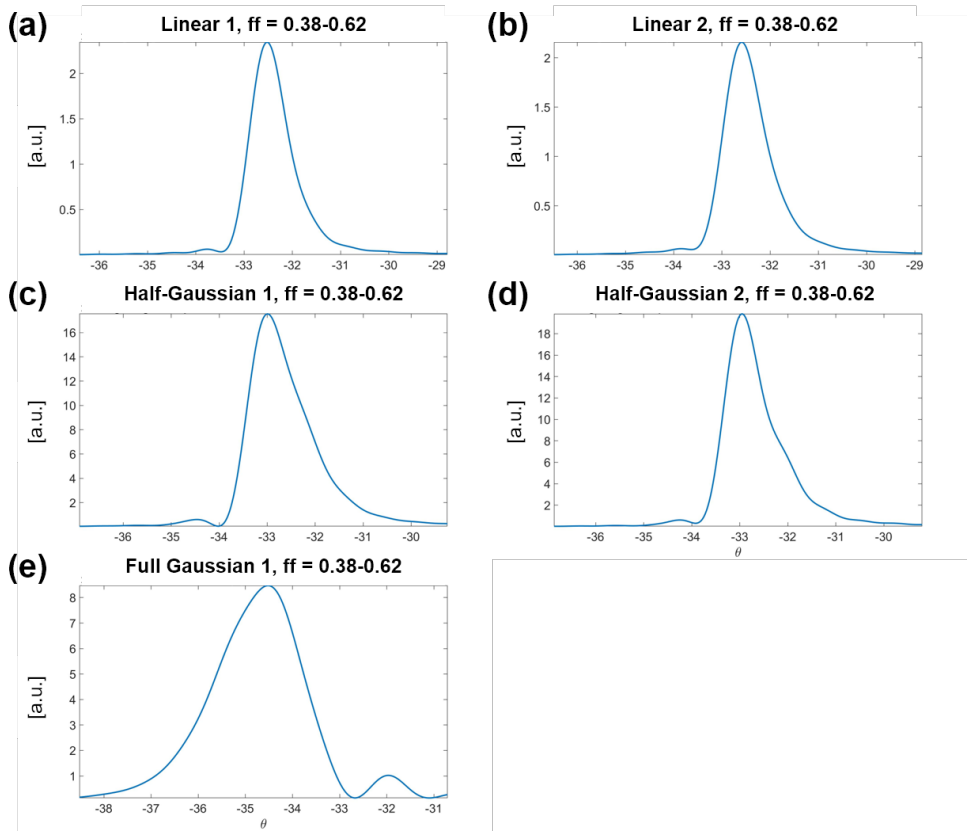

Figure 3-11: Simulated FWHM of optical beam emitted from the apodized gratings. The peak cross-sections are in arbitrary units [a.u.]. (a) Linear design 1, FWHM = 0.91°; (b) Linear design 2, FWHM = 0.99°; (c) Half-Gaussian design 1, FWHM = 1.29°; (d) Half-Gaussian design 2, FWHM = 0.99°; (e) Full Gaussian design, FWHM = 2.12°.

3.0.4 Device Layout

Below the design layout of the input waveguides, lens, and grating design are described in detail. The waveguides act as point sources and are placed in a circularly symmetric distribution at a radial distance from the Luneburg lens. In this case, the lens was designed to take input waveguides at a distance 3 times the radius (R) of the lens. The Luneburg lens can collimate the optical mode diverging from any of the waveguides. Selecting the input waveguide allows the optical beam to be steered in the plane of the device (azimuthal direction) as shown in Fig. 3-12. The waveguides are spaced 4 μm apart to reduce coupling between each waveguide. Moreover, the curvature of the waveguides was designed to reduce bend losses.

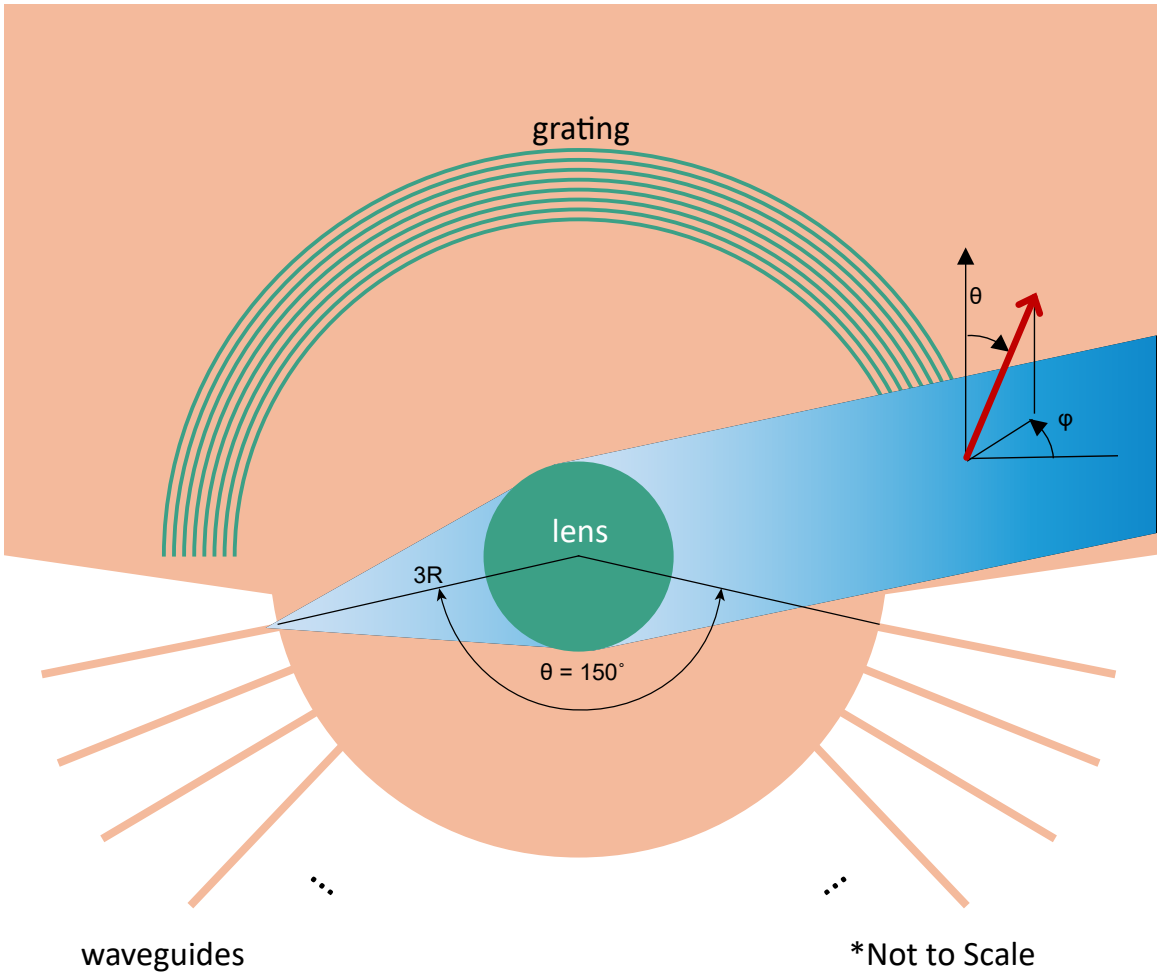

Figure 3-12: Top view schematic of waveguides controlling the angle of incidence of the slab mode into the Luneburg lens and the subsequent phase front collimated within the plane of the chip. The azimuthal field of view of the system is approximately 150°. Choice of the waveguide determines the in-plane beam steering. The waveguides are placed at a focal distance that is three times the radius (R) of the lens. The circular grating is used to couple the collimated beam into the far-field. The grating design can be varied with respect to geometric features such as pitch, ff, and apodization to control the emission profile and far-field beam divergence.

After collimation, a circularly symmetric grating coupler is used for coupling light out of the plane of the device (in the polar direction), Fig. 3-12. The grating was designed to allow uniform emission from the circularly symmetric Luneburg lens and

used the following constraints: The Luneberg lens is placed at the origin of the $\hat{x}$ and $\hat{y}$ coordinate system that describes the plane of the chip. The lens has a finite width which corresponds to the size of the aperture along the $\hat{x}$ dimension. To first order, it is assumed that the Luneburg lens collimates the slab mode that originates from the interface between the waveguide and the slab that contains the Luneburg lens. Since the lens collimates the propagating slab mode, it is also assumed that the only portion of the grating that couples out the slab mode is the region with a width equal to the lens diameter (D), Fig. 3-13. Moreover, to ensure that the grating performed well, a constraint was placed such that there was no more than a 1 percent deviation between the grating start radius (R_g) that intersects with the middle of the collimated slab mode versus the distance from the edge of the collimated slab mode (L_g). Assuming that for $L_g = 0.99R_g$, the R_g for the circular grating can be determined as shown in Eqn. 3.1:

$$\begin{aligned}
\left(\frac{L_g}{R_g}\right)^2 + \left(\frac{D}{2R_g}\right)^2 &= 1 \\
(L_g)^2 + \left(\frac{D}{2}\right)^2 &= R_g^2 \\
0.99^2 R_g^2 + \left(\frac{D}{2}\right)^2 &= R_g^2 \\
\left(\frac{D}{2}\right)^2 &= R_g^2(1 - 0.99^2) \\
R_g^2 &= \left(\frac{D}{2}\right)^2 \frac{1}{(1 - 0.99^2)} \\
R_g &= \sqrt{\left(\frac{D}{2}\right)^2 \frac{1}{(1 - 0.99^2)}}
\end{aligned} \tag{3.1}$$

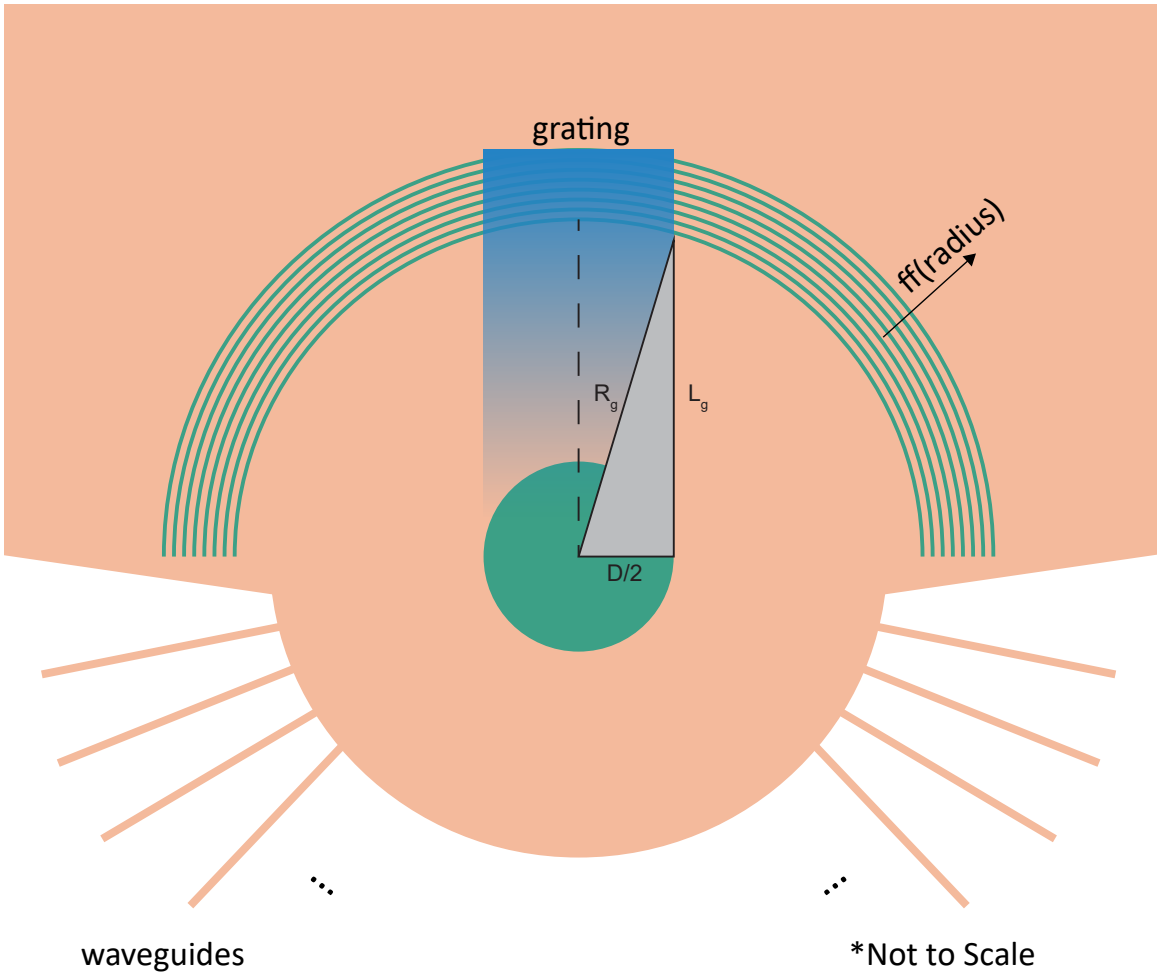

Figure 3-13: Top view schematic of the Luneburg lens with the concentric grating. L_g is the distance from the edge of the lens to the point where the grating intersects the outer edge of the collimated slab mode. The slab mode has a width equivalent to the lens diameter (D). A constraint of $L_g = 0.99R_g$ is implemented for the start radius (R_g) of the circular grating. R_g is measured from the center of the lens. The fill-fraction apodization can vary as a function of the distance from the center of the lens.

3.1 Experimental Results

As discussed in Chapter 2, determining the field of view and the beam divergence of the emitted optical beams from the Luneburg lens devices provides some assessment of the potential that the Luneburg lens architecture has for lidar applications. Using the same experimental setup, 2D Gaussian Fitting, FWHM extraction, and optical power measurement, the performance of the aplanatic and Luneburg devices can be directly compared. These measurements can also be compared to the FDTD simulations of the lens and the grating and provide information about any additional design factors that need to be considered for future designs. All of the devices measured had a Luneburg lens with a diameter between 18.2 and 20.9 μm.

The main difference between each device was based on the grating design. In total, there were four different lens and grating pairings. To measure the functionality of a standard lens and grating, the first two devices used the same lens and a single-layer non-apodized grating with a different grating pitch, $\Lambda = 660$ nm vs $\Lambda = 714$ nm. The primary function of the different Λ was to confirm its effect on the angle of emission. The second two devices paired the same lens and a double-layer apodized grating where each one used a distinct fill-fraction distribution (Half-Gaussian vs Gaussian). The primary function of these two latter devices was to test whether apodization could create greater emission in the upward direction and therefore emit greater power compared to the non-apodized gratings.

As in the previous experiments, the far-field emission was measured by fiber coupling a tunable laser into each individual port via a lensed fiber. The emission from the grating is reflected by a SWIR Lambertian screen. Images of the returned beams are recorded with an InGaAs camera with a mounted high transmission SWIR lens.

3.1.1 Beam Steering Results: $\Lambda = 660$ nm Grating

The analytical solution to the grating equation was used as a guide for choosing the grating pitch which controls the angle of emission and the polar field of view. Specifically, a grating with $\Lambda = 660$ nm was designed to have an emission that is

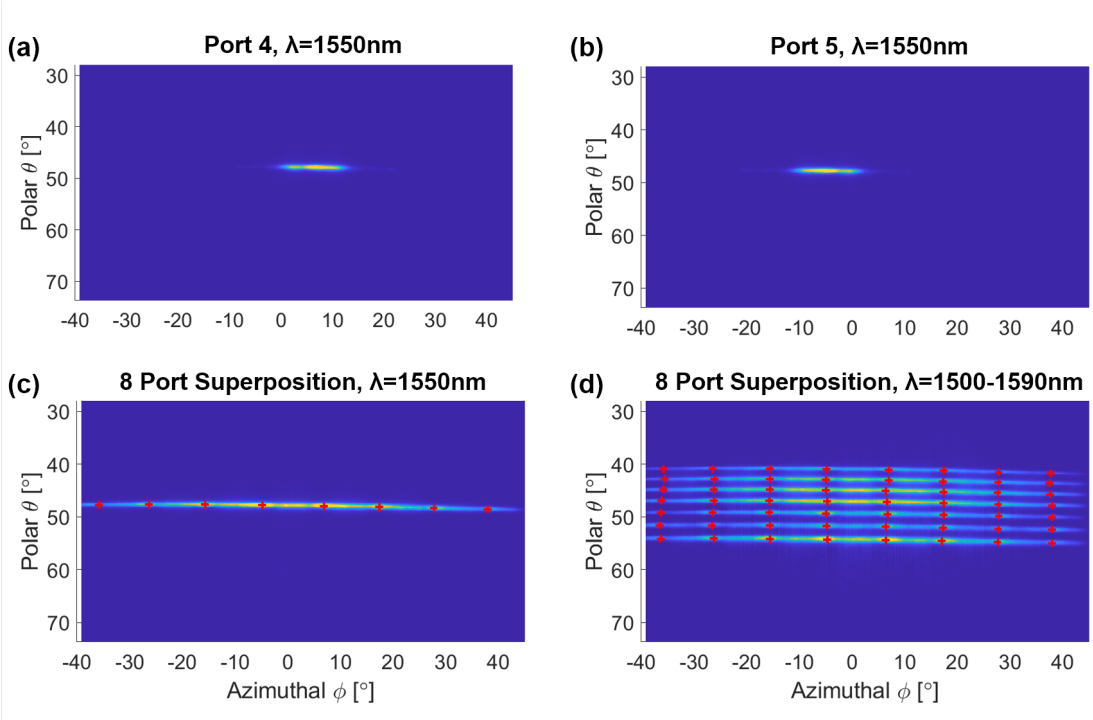

Figure 3-14: Experimental far-field beam emission from a 16 port Luneburg lens device. Grating $\Lambda = 660$ nm and $ff = 0.16$. Only eight ports could be measured due to the screen size and camera field of view. A red cross represents the center of each optical beam. (a) Farfield emission from Port 4 at $\lambda = 1550$ nm. (b) Far-field emission from Port 5 at $\lambda = 1550$ nm. (c) Digital superposition of the optical beams emitted from 8 out of the 16 ports at $\lambda = 1550$ nm. (d) Digital superposition of several line scans at $\lambda = 1500$-1590 nm, with intervals of 15 nm shown for easier visualization.

closer to the plane of the chip compared to $\Lambda = 714$ nm. In addition, $ff = 0.16$ was also chosen to create a weaker perturbation of the permittivity and therefore a weaker emission profile. All beam steering results are represented using the spherical coordinate system as used for the aplanatic lens results described in Chapter 2.

The emission from port 4 and port 5 are shown in Fig. 3-14(a) and (b) respectively where the center of the beams are represented by red crosses. The beams have a Gaussian shape with a wide distribution in the azimuthal direction. Due to the circularly symmetric design of the Luneburg lens and grating, a spherical coordinate system was used to map the far-field optical beams. Fig. 3-14(c-d) shows that switching ports emits a relatively flat line scan and proves that the Luneburg lens performs in a circularly symmetric fashion. It can also be seen in Fig. 3-14(a) and

(b) that there are small hotspots at the outer edges of each optical beam. It is the overlap of the hotspots and their corresponding pixels that creates the bright (and artificial) image artifacts in between each optical beam as the eight far-field beams are superimposed on top of each other. Fig. 3-14(c-d) shows the azimuthal scanning range for the 8 ports was measured to be 73.9° from ϕ = (38.0° to -35.9°) with a mean angle step increment of $\Delta\phi = 10.6°$ via port switching. The polar angle range is 22.8° from θ = (41.0° to 63.8°) using wavelength tuning from 1500-1640 nm. A digital superposition of emitted beams for all 8 ports and several measured wavelengths is shown in Fig. 3-14(d). Only every third line scan between 1500-1590 nm is shown for easier visualization of the line scans.

As described in Chapter 2, the field of view for the system can be calculated using the geodesic between two points and can determined by calculating the dot product of the two vectors that describe the optical beams at the extreme points of the FOV, $cos(\theta) = \frac{\vec{a}\cdot\vec{b}}{|\vec{a}||\vec{b}|}$. We use the results of the 8 measured ports and linearly extrapolate to the FOV for the 16 ports since the system is circularly symmetric and there should be no difference in performance between the central 8 ports and the additional 4 ports on each side. This provides a FOV of 110.2° by 22.8° in the in-plane and out-of-plane directions respectively.

Since only one of each device was tested, there is an insufficient sample size to explain the origin of the hotspots observed in the optical beams. Testing a greater number of devices and further simulations are required to fully understand the experimental results. This would include 1D FDTD simulations of the grating (with the silicon substrate underneath) and ideally 3D simulations that include both the mode propagating through the Luneburg lens and subsequently being emitted from the grating. However, the computational power and memory required for a 3D simulation is at least one order of magnitude greater and is a function of the mesh dimensions, mesh resolution, and the run time.

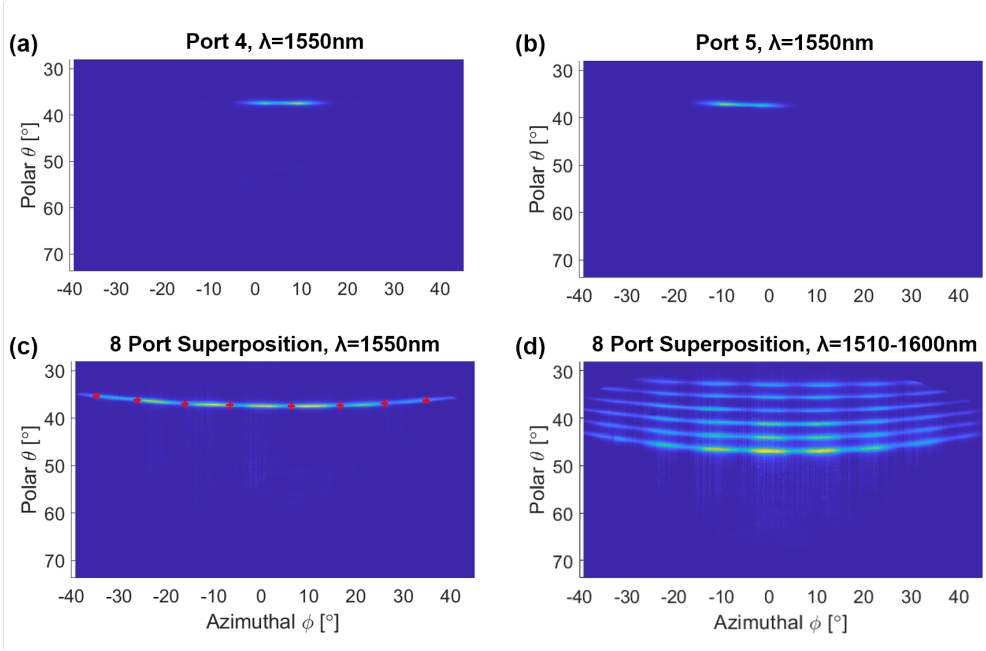

Figure 3-15: Experimental far-field beam emission from a 16 port Luneburg lens device. Grating $\Lambda = 714$ nm, $ff = 0.789$. Only eight ports could be measured due to screen size and camera field of view. A red cross represents the center of each beam. (a) Far-field emission from Port 4 at $\lambda = 1550$ nm. (b) Far-field emission from Port 5 at $\lambda = 1550$ nm. (c) Digital superposition of the optical beams emitted from 8 out of the 16 ports at $\lambda = 1550$ nm. (d) Digital superposition of several line scans emitted at $\lambda = 1510$-1600 nm, with intervals of 15 nm shown for easier visualization.

3.1.2 Beam Steering Results: $\Lambda = 714$ nm Grating

As a standard of comparison, the grating design implemented for the aplanatic lens design was also used here, with $\Lambda = 714$ nm and $ff = 0.789$. The far-field beam steering results are shown in Fig. 3-15. Fig. 3-15(c-d) shows the azimuthal scanning range for the 8 ports and was measured to be 69.7° from $\phi = (34.9°$ to -34.8°) with a mean angle step increment of $\Delta\phi = 9.96°$ via port switching. The polar angle range is 25.9° from $\theta = (29.2°$ to 55.1°) using wavelength tuning from 1500-1640 nm. A digital superposition of emitted beams for all 8 ports and several measured wavelengths is shown in Fig. 3-15(d). Only every third line scan between 1500-1590 nm is shown for easier visualization of the line scans.

As can be seen from Fig. 3-15(d), the optical beams started to go past the outer edges of the 12" x 12" Lambertian screen and could no longer be captured by the IR

camera. Therefore, the FOV of the Luneburg lens and $\Lambda = 714$ nm grating could not be accurateley determined. Regardless, it can be seen that the Luneburg lens was able to steer over a wide range of azimuthal (ϕ) angles. Having a larger Lambertian screen and placing the camera at a larger distance away from the Lambertian screen would have permitted the measurement of the complete FOV of this particular lens and grating.

3.1.3 Beam Steering Results: $\Lambda = 660$ nm Double-Layer Gratings

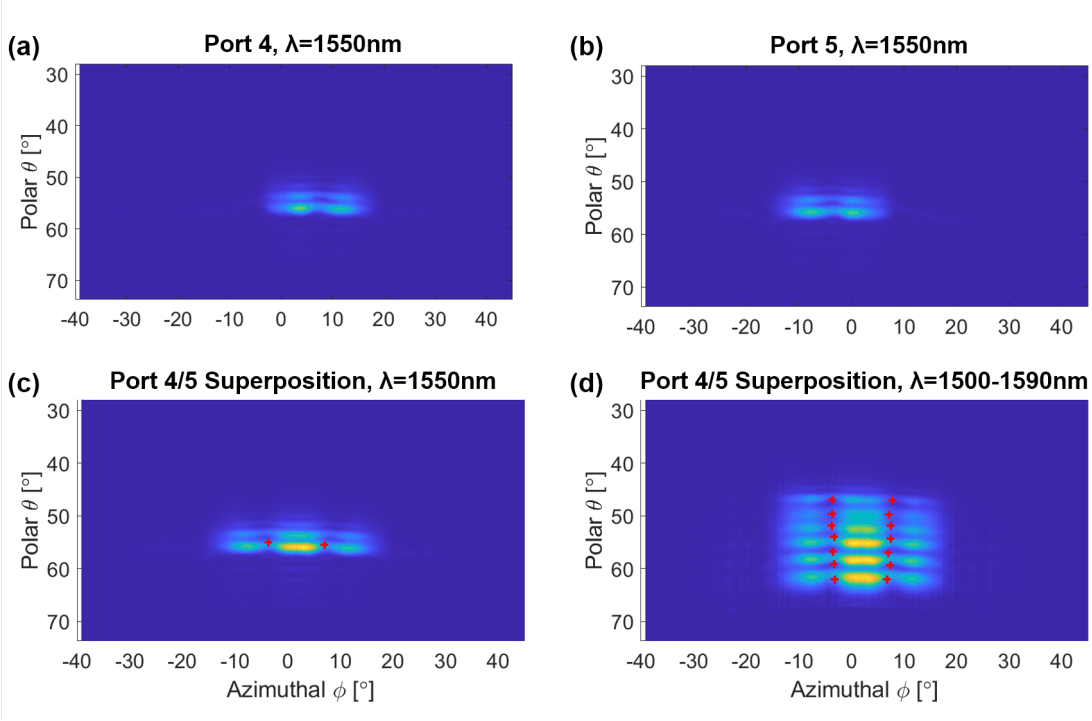

Figure 3-16: Experimental far-field beam emission from a 16 port Luneburg lens device (testing the eight central ports). Apodized grating GC1 with a half-Gaussian fill-fraction distribution and $\Lambda = 660$ nm. Only two ports were measured. A red cross represents the center of each beam. (a) Far-field emission from Port 4 at $\lambda = 1550$ nm. (b) Far-field emission from Port 5 at $\lambda = 1550$ nm. (c) Digital superposition of the optical beams emitted from Ports 4 and 5. (d) Digital superposition of optical beams emitted at $\lambda = 1500$-1590 nm, intervals of 15 nm shown for easier visualization.

Using the results of the simulation study, two distinct double-layer apodized grating designs were chosen in an effort to create unidirectional emission. The grating

layers were designed with a target lateral shift of $\sim \frac{\lambda}{4n_{eff}}$ in the direction of propagation. We label two distinct gratings, GC1 and GC2. GC1 is the double-layer grating with a half-Gaussian apodization with the top layer being shifted by 348 nm. GC2 is the double-layer grating with linear apodization with the top layer being shifted by 358 nm. Even though the shape and power of the optical beam emitted from GC1 and GC2 are similar they are two distinct designs. The resulting optical beams in the far-field are shown in Fig. 3-16 and 3-17. It can be reasoned that the complicated interference between layers creates the multiple interference fringes observed in the far-field. Due to the roughness and variability of the (i) chemical mechanical polishing and (ii) thin film deposition of SiO_2, the ideal $\lambda/4$ spacing in the vertical dimension could not be implemented between the two layers. The lack of the gap in the vertical direction could have created a suboptimal phase difference between the scattering elements (grating teeth) of each layer. Since the propagating slab mode is being scattered by every tooth of the grating, and the width of the teeth is changing due to the ff apodization, the constructive interference between scattering elements is challenging to solve analytically. Therefore, both the FDTD and the experimental results need to be used to adequately evaluate designs. Inspecting the individual beam shapes for either the half-Gaussian Fig. 3-16(a-b) or linear apodization Fig. 3-17(a-b), it can be seen that the "dumbbell" shape of the optical beam as seen for the 660 nm and 714 nm gratings, in Fig. 3-16 and 3-17, is preserved but spread out in the vertical direction with multiple fringes.

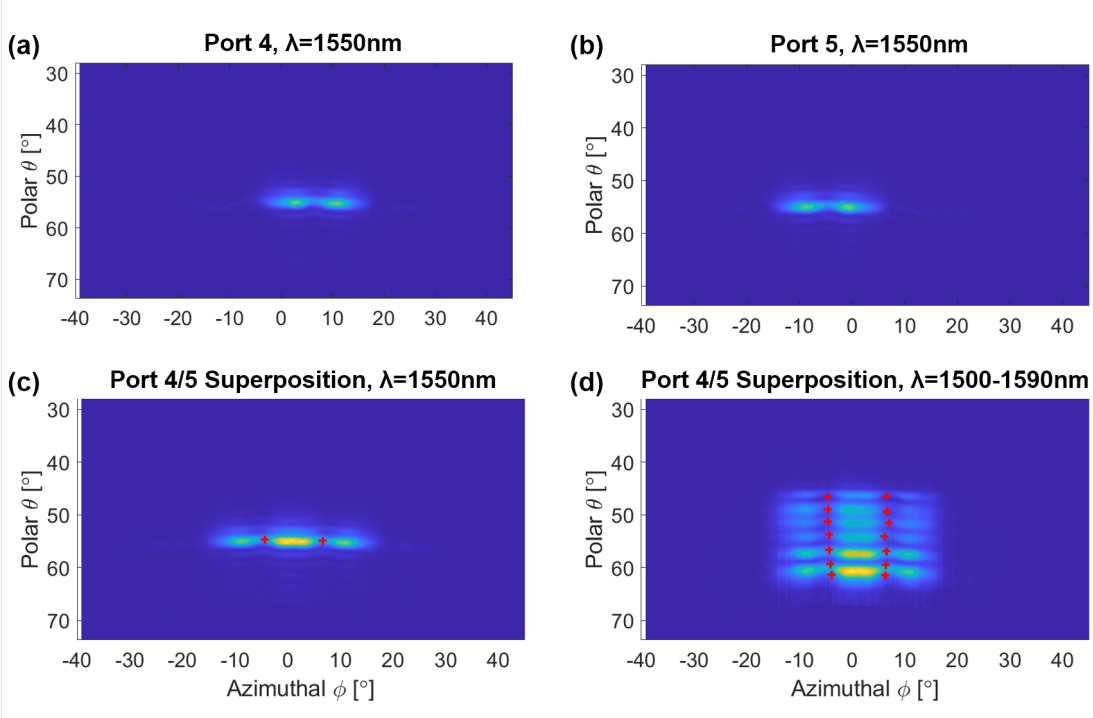

Figure 3-17: Experimental far-field beam emission from a 16 port Luneburg lens device (testing the eight central ports). Apodized grating GC2 with a linear fill-fraction distribution and $\Lambda = 660$ nm. Only two ports were measured. (a) Far-field emission from Port 4 at $\lambda = 1550$ nm. (b) Far-field emission from Port 5 at $\lambda = 1550$ nm. (c) Digital superposition of the optical beams emitted from Ports 4 and 5 at $\lambda = 1550$ nm. (d) Digital superposition of the optical beams emitted at $\lambda = 1500$-1590 nm, intervals of 15 nm shown for easier visualization.

3.1.4 FWHM of the Single-Layer Gratings: $\Lambda = 660$ nm and $\Lambda = 714$ nm

Two-Dimensional Gaussian Fitting Function

A two-dimensional Gaussian fitting was used to fit the cross-sections of the far-field beams. This 2D Guassian fitting was then used to reduce the recorded image data to the corresponding FWHM of each individual optical beam emitted from a particular device. A script adapted from the MATLAB function 'lsqcurvefit' written by Nootz [53] and Diaz [54] finds the position, orientation, and width of a two-dimensional Gaussian. The optical beams for the grating $\Lambda = 660$ nm and the ports 1, 2, 7, and 8 are shown in Fig. 3-18. The optical beams for the grating $\Lambda = 714$ nm and the ports

1, 2, 6, and 7 are shown in Fig. 3-19. The center image shows the 2D interpolated image of an optical beam where the green and red lines shows the data points used for the Gaussian fit in the azimuthal and polar direction respectively. The top plot shows the image data (red) and the Gaussian fit (black) for the azimuthal cross-section.

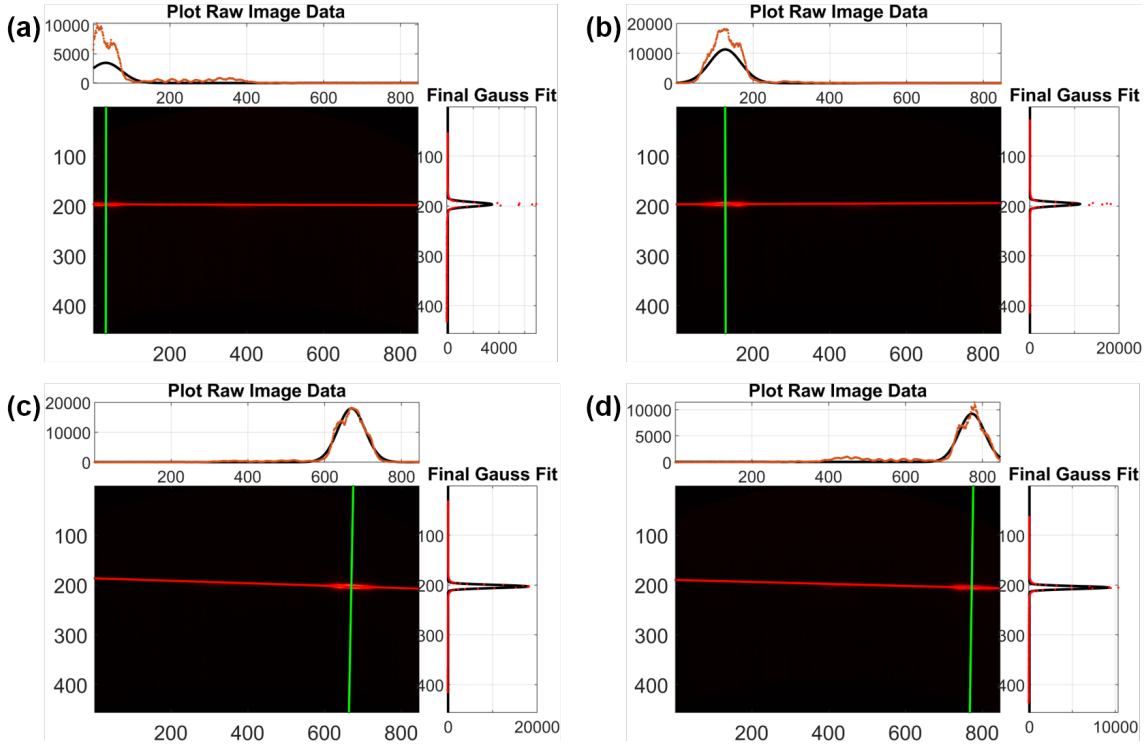

Figure 3-18: Grating with $\Lambda = 660$ nm and $ff = 0.16$. Examples of least squares fits to a two-dimensional Gaussian for (a) Port 1, (b) Port 2, (c) Port 7, and (d) Port 8. Port 1 and Port 2 display multi-peak characteristics, and the Gaussian fitting has a harder time fitting a curve that matches the multi-peak shape of the cross-section as seen in (a) and (b).

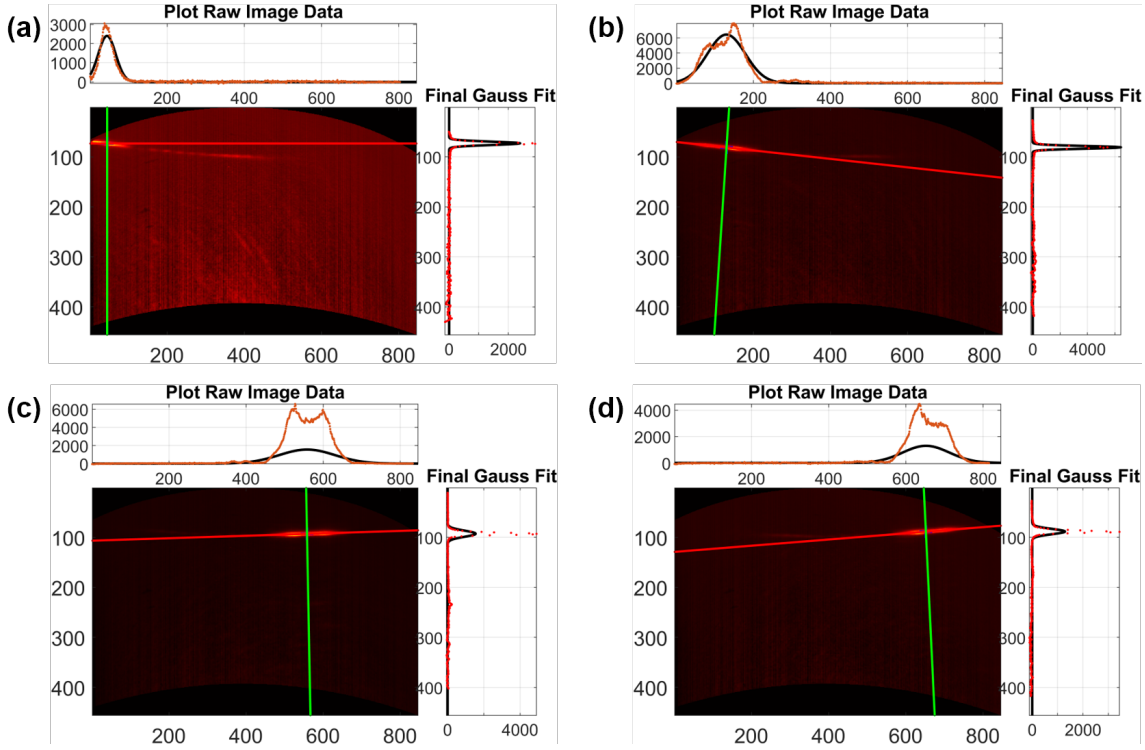

Figure 3-19: Grating with $\Lambda = 714$ nm and $ff = 0.789$. Least squares fits to a two-dimensional Gaussian for (a) Port 1, (b) Port 2, (c) Port 6, and (d) Port 7. The background in (a) is brighter since the beam hits the edge of the Lambertian screen, this creates more scattering and increases the background in different regions of the image. The Gaussian fitting has a difficult time fitting to multi-peaked and uniquely shaped distributions as seen in (c) and (d).

FWHM of Experimentally Measured Optical Beams

The FWHM measurements for the single-layer $\Lambda = 660$ nm grating were fitted for three distinct lambda at $\lambda = 1520$, 1550, and 1600 nm and are shown in Fig. 3-20. The FWHM were determined by fitting a rotated Gaussian along both the major and minor axis of the beams. As is observed from the images, the cross-section closest to the azimuthal (ϕ) direction is the major-axis while the cross-section closest to the polar (θ) direction is the minor-axis. Using this rotated Gaussian fitting, the average FWHM of the major axis at $\lambda = 1550$ nm is 7.00° and the average FWHM of the minor axis is 0.94°. The FWHM values are consistent regardless of port number or wavelength. The major axis of the beam is larger because of the diameter of the lens, D = 18.19 μm, is at least two times smaller than the effective length of the gratings.

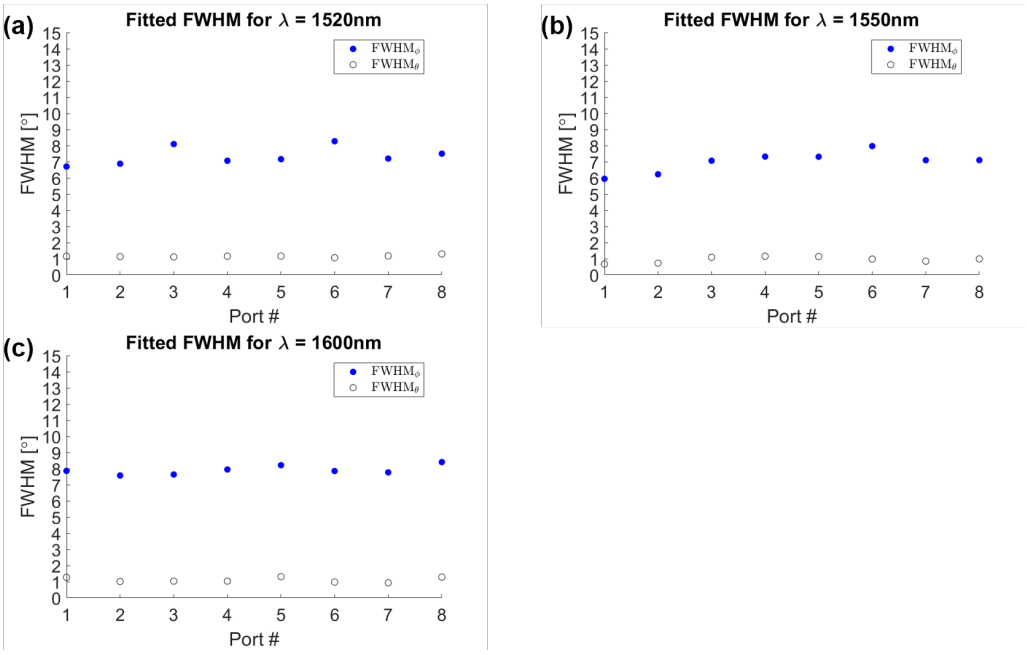

Figure 3-20: Extracted FWHM of $\Lambda = 660$ nm grating (eight most inner ports) at a variety of wavelengths. (a) $\lambda = 1520$ nm with a mean of 7.36° in the ϕ direction and 1.15° in the θ direction, (b) $\lambda = 1550$ nm with a mean of 7.00° in the ϕ direction and 0.94° in the θ direction, (c) $\lambda = 1600$ nm with a mean of 7.90° in the ϕ direction and 1.10° in the θ direction.

For the $\Lambda = 714$ nm grating, the average FWHM of the major axis at $\lambda = 1550$nm is 7.72° and the average FWHM of the minor axis is 1.10°, Fig. 3-21. Since the 714 nm grating has an emission angle that is closer to normal ($\theta = 0°$) for the wavelength range $\lambda = 1500$-1510 nm, the emission hits the top and side edges of the Lambertian screen. This makes it a greater challenge to fit the data for the 714 nm grating images compared to those for the 660 nm grating. Moreover, since the angle of emission is a function of the grating pitch and wavelength of the laser, the path length traveled between the bottom of the grating and silicon substrate will be different for each distinct wavelength. This will affect the (de)constructive interference and influence the shape of the optical beam and consequently the Gaussian fitting. One way to reduce the fringe pattern is to include the silicon subtrate in subsequent simulations and ensure that the emitted beam has a shape that is close to a single peak.

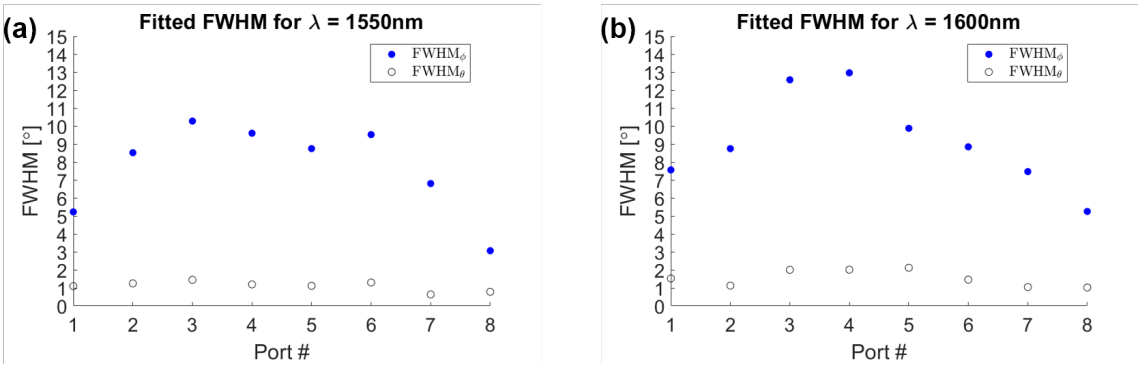

Figure 3-21: Extracted FWHM of $\Lambda = 714$ nm grating (eight most central ports) at two wavelengths. (a) $\lambda = 1550$ nm with a mean of 7.72° in the ϕ direction and 1.10° in the θ direction, and (b) $\lambda = 1600$ nm with a mean of 9.16° in the ϕ direction and 1.54° in the θ direction.

3.1.5 Optical Power Measurements

As discussed in Chapter 2, it is desirable to reduce on-chip photonic losses as much as possible so that the overall optical power required of the input laser is kept to below 100 mW since that is the range for readily available lasers [61, 62]. Moreover, as will be discussed in Chapter 4, for a lidar system the free space loss at 200 m is significant and unavoidable, and requires the mitigation of the on-chip photonic losses.

The power emitted in the far-field was measured for the four different grating designs using an integrating sphere approximately 1 cm away from the aperture. The first pair of devices were single-layer gratings with no apodization for the fill-fraction ($\Lambda = 714$ nm and $\Lambda = 660$ nm). The second pair were two double-layer apodized gratings with $\Lambda = 660$ nm with half-Gaussian and linear apodization for the fill-fraction (named GC1 and GC2 respectively). Both sets of gratings were paired with the same Luneburg lens design. The optical power loss measurements took into account propagation through (i) the waveguide, (ii) the Luneburg lens, and (iii) the emission out of the grating and into the far-field. The loss from the experimental setup, including loss from fiber-coupling into the chip via a lensed fiber is already taken into account and excluded from the tabluated values.

The first grating measured was designed with $\Lambda = 714$ nm and constant $ff = 0.789$. The power was measured for the two central ports of a 16-port device, Port

8 and Port 9 respectively. The loss was measured for three different input powers, 0.000, 3.000, and 6.990 dBm as seen in Fig. 3-22. On average, Port 8 had a loss of -10.55 dBm and Port 9 had a loss of -10.52 dBm. The three different input powers were used with a combined average loss of -10.53 dB at an input power of 0.000 dBm.

Port #	Input (dBm)	Input Power (µW)	Output Power (µW)	Loss (dBm)
8	0.000	1000	88.19	-10.546
8	3.000	1995	175.5	-10.557
8	6.990	5000	441.0	-10.546
9	0.000	1000	88.70	-10.521
9	3.000	1995	177.0	-10.521
9	6.990	5000	444.0	-10.516

Figure 3-22: Optical power measurements for $\Lambda = 714$ nm, Port 8 and Port 9. The combined average loss through the waveguide, lens, and grating was -10.53 dB.

The second grating measured was designed with $\Lambda = 660$ nm and constant $ff = 0.16$. The first series, Series 1, of optical power measurements for the $\Lambda = 660$ nm grating are shown in Fig. 3-23. Due to the over 1.50 dBm discrepancy measured between Port 8 and Port 9, a second series of measurements, Series 2, was taken to determine if either (i) there was something unique about the structure and ports, (ii) if the measurement conditions had been affected due to light polarization not being fully transverse electric (TE), or (iii) if there was mechanical misalignment of the lensed fiber.

Series 2 was measured nine days after Series 1. Since the measured loss for both the 660 nm and 714 nm grating was consistent across different laser powers, only the 0.000 dBm input power was remeasured for Series 2, Fig. 3-24. Note that the average loss for Series 1 is -6.808 dBm and for Series 2 is -5.624 dBm (measured nine days later). The delta between the two series is 1.184 dBm. This is most likely due to a combination of the strain on the optical fiber (affecting the TE polarization of light) and the alignment of the lensed fiber to the waveguide during coupling. Since the Series 2 provided a more consistent measurement between Port 8/9, these values were used as the baseline when compared to other grating designs. Comparing the measurements, it is notable that the 660 nm grating ($ff = 0.16$) has 3 dB lower loss

Port #	Input (dBm)	Input Power (μW)	Output Power (μW)	Loss (dBm)
8	0.000	1000	236.4	-6.264
8	3.000	1995	473.0	-6.251
8	6.990	5000	1184	-6.256
9	0.000	1000	162.5	-7.891
9	3.000	1995	323.9	-7.896
9	6.990	5000	814.7	-7.880

Figure 3-23: Series 1: First series of optical power measurements for $\Lambda = 660$ nm, Port 8 and Port 9. The average loss through the waveguide, lens, and grating is -6.26 dB and -7.89 dB respectively. The over 1 dB discrepancy between the two adjacent waveguides was not expected. This required an additional series of optical measurements, shown in Fig. 3-24

Port #	Input (dBm)	Input Power (μW)	Output Power (μW)	Loss (dBm)
8	0.000	1000	278.4	-5.553
9	0.000	1000	273.9	-5.624

Figure 3-24: Series 2: Second series of optical power measurements for $\Lambda = 660$ nm, Port 8 and Port 9. The measured loss through the waveguide, lens, and grating is -5.55 dB and -5.62 dB respectively. The relatively small Δ of ~ 0.1 dB between Port 8 and 9 demonstrates there were issues with the Series 1 measurements since the first series had a Δ of over 1dB between the two ports. Series 2 was taken as the baseline measurement for the $\Lambda = 660$ nm grating design.

than the 714 nm grating ($ff = 0.789$). This is likely due to the higher fill-fraction of the a:Si in the 714 nm grating which could create greater loss due to absorption.

Port #	Input (dBm)	Input Power (μW)	Output Power (μW)	Loss (dBm)
8	0.000	1000	258.4	-5.877
9	0.000	1000	261.6	-5.824

Figure 3-25: Optical power measurements for grating with half-Gaussian apodization, GC1.

Next, the power emitted from the apodized gratings, GC1 and GC2, was measured. The emission from Port 8 and Port 9 was measured with an input laser power of 0.000 dBm. The average loss from GC1 was -5.851 dB, Fig. 3-25, whereas the average loss from GC2 was -6.399 dB, Fig. 3-26. Note that the power delta of 0.548 dB between GC1 and GC2. The differences could be due to the measurement setup and/or the

intrinsic device performance.

Port #	Input (dBm)	Input Power (µW)	Output Power (µW)	Loss (dBm)
8	0.000	1000	231.1	-6.361
9	0.000	1000	227.2	-6.437

Figure 3-26: Optical power measurements for grating with linear apodization, GC2.

When comparing the power measurements to the transmission from the 1D grating simulations, it is clear that the apodized grating designs did not have any increase in optical power emission. Inspecting the simulation and experimental results, it became apparent that the silicon substrate at a distance of 2 μm from the grating needed to be included in the simulations because of the internal reflections between the grating and the silicon substrate. Moreover, for the double-layer grating, the (de)constructive interference between each optical path is even more complicated because both the top and bottom layer of the grating would have emission in the downward direction and have a series of reflections at each interface (including at the silicon substrate interface).

3.2 Conclusion

In summary, this chapter discussed the first experimental demonstration of a Luneburg lens and circular grating for two-dimensional optical beam steering with a field of view of 110.2° by 22.8° in the in-plane and out-of-plane directions respectively. Moreover, this was the first demonstration to leverage a wafer-scale fabrication platform based on optical lithography. Various grating designs aimed at improving the optical beam performance were discussed. Simulations demonstrated that a single-layer grating with a low fill-fraction is likely to provide an effective aperture length of approximately 1 mm. It was shown that the double-layer apodized gratings have the potential to emit up to 90 % in the upward direction. Lastly, optical power measurements demonstrated that it is necessary to include the underlying silicon substrate to take into account multiple reflections that can happen at each interface of the grating

and the substrate. These reflections not only affect the power emission but also the shape of the final emitted beam.

Chapter 4

Conclusion: Requirements for a Lidar-on-a-chip FMCW System

Even though the development of a fully solid-state optical beam steering architecture has gained the attention of the academic community and is the focus of this thesis, there are still several architecture challenges that need to be addressed before a practical and high performance FMCW lidar-on-a-chip system can be deployed into the real world. To conclude, I briefly discuss engineering challenges that affect the aperture size and beam resolution, the scanning frame rate, and laser requirements for long distance ranging.

4.1 Luneburg Lens Scaling

Using the approximation, λ/D, a high-resolution system with a beam divergence of 0.1° requires a Luneburg lens diameter (D) of 1.5 mm and a grating with an effective aperture of the same size. Considering the current performance of the measured gratings in the Luneburg lens architecture, the grating needs an aperture one order of magnitude larger.

To reduce the optical power losses, further simulation of double layer grating structures can be explored to optimize the constructive interference between the layers of the grating and the underlying Si substrate to obtain upward transmission close to

90% (reducing the loss by almost 3 dB). In conjunction, an approach to further improving the aperture size and emission uniformity is to implement an apodized grating coupler via a photonic crystal (PhC) grating as demonstrated by Ding et al. [80]. This will allow greater flexibility in the fill-fraction apodization by introducing a wide range of hole/pattern density and hole diameters to control the effective refractive index.

4.2 Increasing the Frame Rate and MZI Switch Speed

As the planar lens architecture is scaled, the 10 to 30 Hz frame rate for high-performance applications poses a challenge due to the number of pixels that need to be measured in a wide FOV. Due to the discrete nature of generating optical beams via the waveguides and the lens, a transmit/receive scheme would need to increase the number of pixels simultaneously measured by one to two orders of magnitude. By using the lidar requirements in Fig. 4-1(a) as a baseline, the number of pixels measured per frame can be calculated. Note that the following calculations must also be done and applied to other beam steering architectures. Using the horizontal and vertical FOV, we calculate 120 degrees/0.1 degrees = 1200 pixels in the horizontal direction and 20 degrees/0.1 degrees = 200 pixels in the vertical direction are required. Therefore, there are a total of 240,000 pixels in one full frame. Considering that a coherent measurement requires a dwell time of approx. $T_{meas} = 100$ μs for a distance of 200 m [7], it would take 24 seconds (0.042 Hz) to capture one complete frame. Note that the T_{meas} constraint applies to any coherent measurement at a range of 200 m. Considering that the desired framerates for lidar are between 10 to 30 Hz, the number of pixels and therefore optical beams being recorded at the same time would need to be increase by 240 times or more. Note that relaxing the resolution requirement by a factor of two will increase the possible frame rate by a factor of four since the resolution determines the area of the pixel in the resulting spatial map.

(a)

Metrics	Value
Range	200 m
Horizontal FOV	120º
Vertical FOV	20º
Beam Div.	1 mrad
Aperture	1.5 mm
Frame Rate	≥ 10 Hz

(b)

20 cm Beam @ 200 m *assuming 1 mrad	Optical Power (dBm)
Laser Power	+20.0
Loss Free Space (L_{FS})	-115.0
Total On-Chip Photonic Losses	-37.0
Signal at Photodetector	-132.0

Figure 4-1: (a) Lidar performance requirements for a high-performance system. The horizontal and vertical field of view (FOV) in conjunction with the resolution determines the number of individual pixels that need to be coherently measured. The beam divergence in the far-field is set by the optical aperture size. (b) Optical power requirements for long distance ranging. The free space loss (L_{FS}) is calculated at a distance of 200 m under ideal weather conditions. The laser power and photonic losses need to compensate for the L_{FS}.

Using the current planar lens architecture, the number of waveguides would require 11 layers for the MZI tree. Since the thermal phase shifters in the current MZIs have a switching speed of 10 KHz [15], and assuming that each layer can be switched simultaneously, then one line scan consisting of 1200 waveguides in the azimuthal direction would take 0.12 seconds. Therefore, the switching speed limitations and the T_{meas} constraint would require a multiplexing scheme to meet the scan rate requirements for the desired FOV and range.

4.3 Laser Requirements for Ranging and FMCW Detection

In addition to frame rate challenges, there are also challenges based on both the T_x/R_x loss, the frequency modulation, and the wavelength tuning range of the laser. For 200 m ranging, the L_{FS} of -115 dB must be overcome by either increasing the laser power and/or reducing the loss of the photonic integrated circuit (PIC) components. Note that for 100 m ranging the L_{FS} is approximately -110 dB.

Based on the 8 port MZI experiments in the previous chapter, the estimated loss

per MZI layer is 7 dB/3 layers = 2.333 dB. Therefore, the total estimated loss for 11 layers is 25 dB. In addition, the current measured losses for the combined lens and grating is 6 dB. This estimates a total one way on-chip loss of 31 dB. We compare this to the loss calculations presented by Kim [7]. Calculating a standard photodetector responsivity of 1 A/W [87], T_{meas} = 100 μs, and a signal to noise ratio of 30, the shot noise limit for a detectable signal is 0.48 pW $\approx$ -103 dBm. It may be possible to eliminate the MZI tree for the R_x by creating a large array of parallel photodetectors. This would lead to a loss of 31 dB for the T_x and an additional 6 dB on the R_x for a total path loss of 37 dB, Fig. 4-1(b). Assuming this scenario and the shot noise limit, a practical planar lens system would need to reduce the loss by 30 dB. It is realistic to assume that $\sim$ 6 dB can be gained via two apodized gratings with unidirectional transmission, while another 10 dB is possible via a high power 1 Watt laser. Regardless, the switching mechanism for the 11 layer tree would need a new design to reduce the loss by an additional 14 dB, requiring an improvement of slightly more than 1 dB per layer.

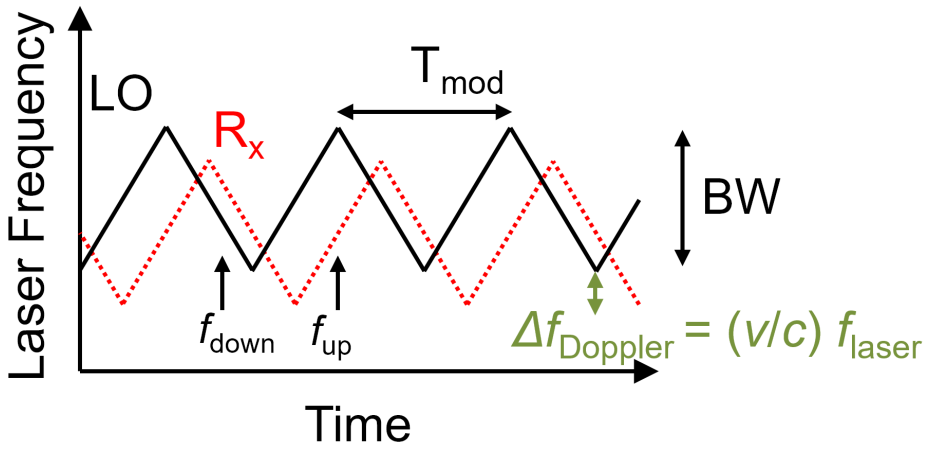

Figure 4-2: Plot demonstrating the frequency-modulated continuous wave (FMCW) signal processing scheme. The local oscillator signal, LO, is shown in black and the returned signal, R_x, is shown in red. A triangular modulation is applied over a time period, T_{mod}. The Doppler shift creates a difference between the f_{down} ramp and the f_{up} ramp of the signals. R_x is decreased by $\Delta f_{Doppler}$ and is a function of the velocity (v) of the detected object, the speed of light (c), and the frequency of the laser f_{laser}.

In addition to the frame rate and optical power, there are additional requirements

for the FMCW modulation scheme. For example, Kim calculated that a FMCW scheme with a coherent measurement time (T_{meas}) of 100 μs requires a laser modulation bandwidth ($f_{BW,laser}$) of 1 GHz and a corresponding analog to digital converter bandwidth ($f_{BW,ADC}$) of 60 MHz. The $f_{BW,laser}$ allows for the triangular waveform applied to the local oscillator (LO) and consequently permits the coherent detection by beating the LO with the R_x signal, Fig. 4-2.

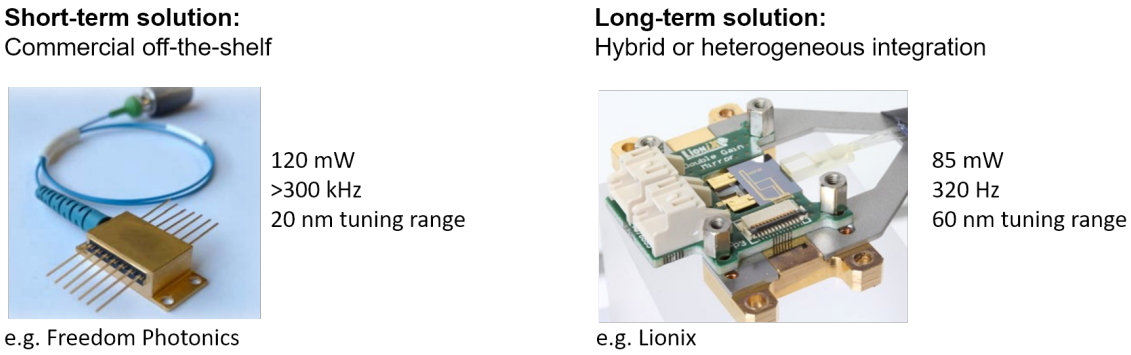

Figure 4-3: Examples of packaged tunable lasers produced by commercial entities Freedom Photonics and Lionix. A minimum optical power of 100 mW and a maximum line width of 240 kHz is required for 200 m ranging. The wavelength-based scanning in the vertical direction requires a tuning range of 100-160 nm. Adapted from Freedom Photonics [61] © 2022. Adapted from Epping et al. [62] © 2019.

There is usually a trade-off between the three main characteristics of a laser: peak optical power, line width, and tuning range. Using the 200 m ranging requirement, we assume a 100 mW = 20 dBm requirement as the baseline. Moreover, to have a 200 m range, a minimum coherence length ($L_{coherence}$) of 400 meters would be necessary, translating to a maximum linewidth of 240 kHz. Here the equation $L_{coherence} = \frac{c}{\pi \Delta \nu}$ is used to calculate the necessary coherence length where $\Delta\nu$ is the line width. Lastly, referring back to the high-performance requirements, the 20° vertical FOV would also require a laser tuning range of 160 nm.

A starting point for a compact lidar demonstration could use a separately packaged laser that is fiber-coupled onto the PIC. There are several emerging lasers produced by commercial entities including Freedom Photonics [61] and Lionix [62] as shown in Fig. 4-3. As can be seen by the performance metrics, the optical powers ranging between 85-120 mW and linewidths of $\sim$ 300 kHz are within the required ranges, but

the maximum 60 nm tuning range of the Lionix laser falls short by a factor of at least two. The most likely approach for grating-based beam steering would require using two to three different lasers with complimentary tuning ranges to cover the 20° vertical FOV. To address the tuning range and the frame rate requirements, it may be possible to multiplex at the same time, but the signal processing is beyond the scope of this thesis.

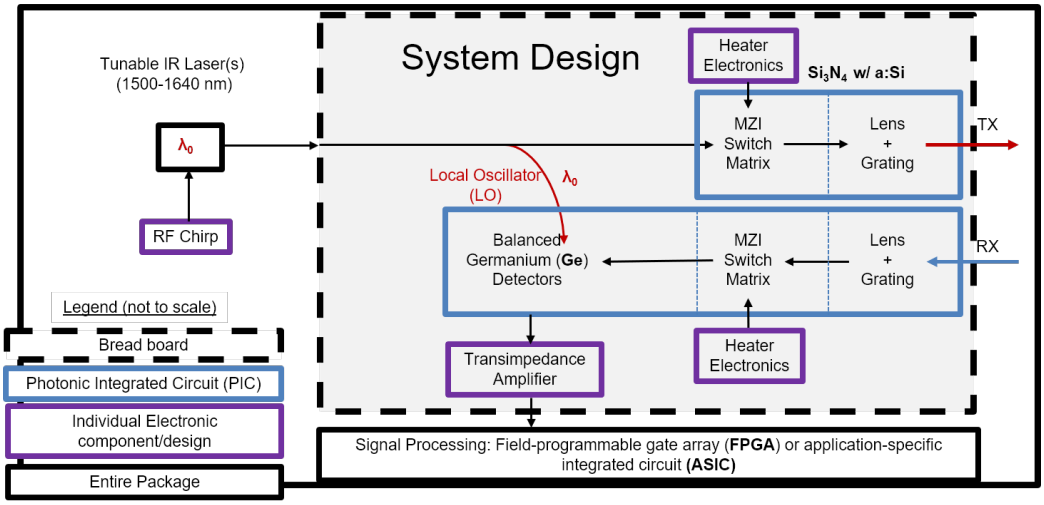

Figure 4-4: Overview of proposed lidar system. FPGA and RFSoC drive the frequency modulation of the LO. A separate MZI, lens, and grating is used for each path of the bistatic Tx/Rx setup. The balanced detectors beat the LO and Rx signals for the FMCW detection scheme. The TIA is used to convert the sinusoidal current to a voltage.

There are several requirements for the signal processing and electronic control of a lidar-on-a-chip system, Fig. 4-4. The RF chirp modulation of the laser can be performed by using a field programmable array (FPGA) integrated with a Xilinx Zynq RF System-on-a-chip (RFSoC) [88]. The proposed bistatic operation requires one path for the transmitted (T_x) signal and one path for the received (R_x) signal. A balanced detector consists of two photodetectors (usually germanium) that are used to beat the LO and R_x signal [87]. The photodetectors are connected in series so that the currents subtract at the transimpedance amplifier (TIA). The resulting current is a sinusoid and is a function of the optical frequencies corresponding to the LO and R_x signal. A TIA is used to convert the resulting current to a voltage.

4.4 Transitioning to a Commercial Foundry

One of the final steps necessary before the planar lens architecture can be used in a commercial product will be to transfer the fabrication process from MIT Lincoln Laboratory (MIT LL) to a commercial photonic foundry. The 90 nm node Si_3N_4/a:Si process at MIT LL has demonstrated the feasibility of depositing the dielectric stack necessary for the lens. However, it is important to note that depositing a:Si on top of Si_3N_4 is not used widely for current PIC designs. Therefore, any commercial foundry will need to optimize the planarization of the Si_3N_4 and the subsequent deposition of a:Si. In conjunction with optimizing the dielectric stack, a commercial lidar-on-a-chip system will require significant engineering of each photonic on-chip component including the grating, lens, switch tree, and tunable laser. Fortunately, many photonic foundries across the world are adding lasers and detectors to their process development kits (PDKs) [13, 14]. A summary of the integrated photonics ecosystem is shown in Fig. 4-5. Considering the improvement of lasers and other photonics components within PDKs, it is possible to overcome the challenges delineated above in the near future.

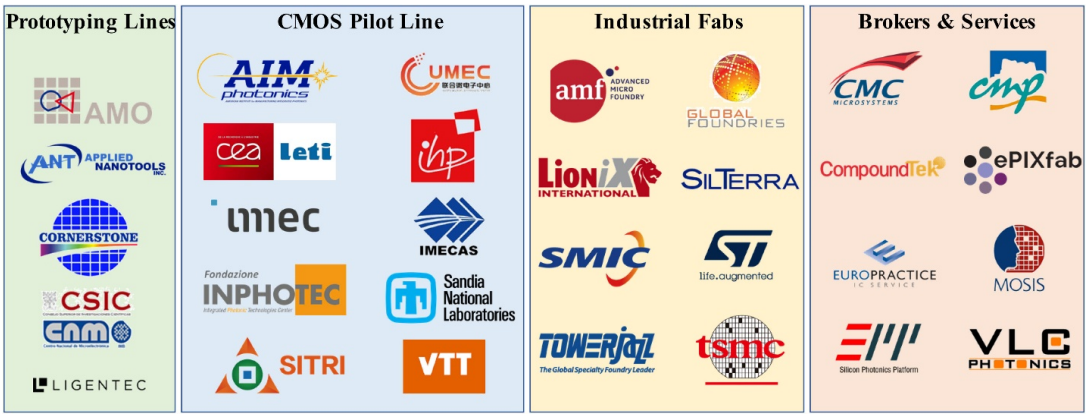

Figure 4-5: Silicon photonics foundries across the world that provide open access fabrication services. Adapted from © 2022 Siew et al., under a Creative Commons Attribution 4.0 International license.

4.5 Conclusion

In conclusion, this thesis has demonstrated two novel planar lens architectures that are suitable for solid-state optical beam steering that work in the near-infrared and are fabricated using a wafer-scale fabrication process. The first is an aplanatic lens design. The second is a circularly symmetric Luneburg lens and grating for uniform emission over a wide field of view. Both lens demonstrations are the first to use a 90 nm node wafer-scale process. Moreover, it was demonstrated for the first time that a planar lens architecture is operated electronically using a Mach–Zehnder interferometer switch tree. Future directions for the optimization of individual photonic components and of a frequency-modulated continuous wave lidar system were presented. The use of a wafer-scale fabrication process and well known dielectric materials makes it feasible that this planar lens architecture can be used for two-dimensional optical beam-steering with lower electronic complexity and a wider field of view than other state-of-the-art beam steering solutions.

Appendix A

Ray Tracing, Directivity, Number of Resolvable Points, and Index Error

In this Appendix, we detail an updated, corrected, and expanded version of the calculations presented by Skirlo [29]. These include theoretical aspects of the planar-lens optical beam steering architecture, including the grating design, analytical calculations of the far-field directivity, resolvable point estimation, and tolerances due to refractive index error in fabrication.

A.1 Grating

The aperture phase is the most important quantity for our planar lens design, and is completely determined by the initial ray tracing directions, the grating parameters, and the wavelength. Since we are propagating through a straight grating, the plane wave component k_y that is parallel to the grating interface and rulings will be conserved. On the other hand, k_x will be more complicated because it changes at each step of the grating. For these designs, the region with a:Si on top of Si_3N_4 has an effective index n_1 and the region with only Si_3N_4 has an effective index n_2. Assuming an initial in-plane angle of ϕ_{in}, an index of medium n_1, medium n_2, and grating duty cycle d, we find that k_y and $k_{x,avg}$ are:

$$
\begin{aligned}
k_y =& n_2 k_0 \sin(\phi_{in}) \\
k_{x,avg} =& n_2 k_0 (1-d)\cos(\phi_{in}) + n_1 k_0 (d)\sqrt{\left(1 - \frac{n_2^2}{n_1^2}\sin^2(\phi_{in})\right)}
\end{aligned}
\tag{A.1}
$$

The expression under the square also is consistent with Snell's law at the interface between the dielectric regions n_1 and n_2 along the x-direction of the grating coupler via $n_1 \sin(\alpha) = n_2 \sin(\phi_{in})$ and $\sqrt{\cos(\alpha)^2} = \sqrt{1-\sin(\alpha)^2}$ where α is the angle into n_1 . It is important to note that the effective indices for the grating n_1 and n_2 are also functions of the wavelength. To compute the emission angle of this aperture, we perform phase matching between these wave vectors and those of a free-space plane wave emitted from the grating with $\vec{k} = k_0[\sin(\theta_0)\cos(\phi_0), \sin(\theta_0)\sin(\phi_0), \cos(\theta_0)]$, where θ_0 is the polar/vertical direction (measured from the z-axis which is normal to the chip plane) and ϕ_0 is the azimuthal/horizontal direction (in the chip plane). We use momentum conservation as shown by Chrostowski et al[84].

$$
\begin{aligned}
k_0 \sin(\theta_0)\sin(\phi_0) =& n_2 k_0 \sin(\phi_{in}) \\
k_0 \sin(\theta_0)\cos(\phi_0) =& k_{x,avg}(\phi_{in}) - \frac{2\pi m}{\Lambda}
\end{aligned}
\tag{A.2}
$$

Here we have subtracted a crystal momentum $\frac{2\pi m}{\Lambda}$, which originates from the discrete and periodic sampling implemented by the scattering from each grating step. A.2 is rearranged to derive the following expressions for the far-field angles. The angle θ_0 is found by squaring both equations and then adding the results, and ϕ_0 is found by dividing the two equations.

$$
\begin{aligned}
\theta_0 =& \sin^{-1}\left(\frac{\sqrt{(k_{x,avg}(\phi_{in}) - \frac{2\pi m}{\Lambda})^2 + (n_2 k_0 \sin(\phi_{in}))^2}}{k_0}\right) \\
\phi_0 =& \tan^{-1}\left(\frac{n_2 k_0 \sin(\phi_{in})}{k_{x,avg}(\phi_{in}) - \frac{2\pi m}{\Lambda}}\right)
\end{aligned}
\tag{A.3}
$$

We want to understand how the far-field angles depend on the in-plane angle ϕ_{in} and the wavelength λ. We can immediately identify that ϕ_0 will be significantly greater than ϕ_{in}. This results from the grating momentum $\frac{2\pi m}{\Lambda}$ being subtracted from

$k_{x,avg}$ in the denominator. This means that relatively small variations in the input angle will greatly change the output in-plane angle ϕ_0, sweeping it across the field-of-view. This feature ultimately allows us to use the lens in a small angle, aplanatic regime. As we sweep ϕ_{in} we also expect variations in θ_0. The argument of arcsin increases with ϕ_{in}, and ultimately exceeds 1, confining the beam in-plane, the limit being $\sin(\theta_0) = 1$.

$$\begin{aligned} \frac{\left[k_{x,avg}(\phi_{in}) - \frac{2\pi m}{\Lambda}\right]^2 + \left[n_2 k_0 \sin(\phi_{in})\right]^2}{k_0^2} &= 1 \\ \left[\frac{k_{x,avg}(\phi_{in})}{k_0} - \frac{\frac{2\pi m}{\Lambda}}{\frac{2\pi}{\lambda}}\right]^2 + \left[n_2 \sin(\phi_{in})\right]^2 &= 1 \end{aligned} \tag{A.4}$$

By using A.1 and the approximation $\frac{n_2^2}{n_1^2} \approx 1$, the expression A.4 can be simplified using $k_{x,avg}(\phi_{in}) \approx n_{eff} k_0 cos(\phi_{in})$ where $n_{eff} = n_1 d + n_2(1-d)$. Even though n_{eff} is not truly constant, and its variations effect the far-field angles, qualitatively this description holds. We find that the cutoff angle ϕ_{cutoff} satisfies the following equation which can be rearranged into a quadratic equation to solve for ϕ_{cutoff}:

$$\begin{aligned} \left[n_{eff}\cos\left(\phi_{cutoff}\right) - \frac{\lambda m}{\Lambda}\right]^2 + n_2^2\left[1 - \cos\left(\phi_{cutoff}\right)^2\right] &= 1 \\ \cos\left(\phi_{cutoff}\right) &\approx \frac{1 - \frac{\lambda^2}{\Lambda^2} - n_{eff}^2}{-2n_{eff}\frac{\lambda}{\Lambda}} \end{aligned} \tag{A.5}$$

Overall, we can envision how $\vec{k}$ evolves as a function of ϕ_{in}. Starting from emission normal to the surface, as we adjust ϕ_{in} away from 0, $\vec{k}$ turns rapidly to one side and falls into the plane. We can further visualize this trajectory by rearranging A.2 and using the momentum matching conditions, $u_{x,0} = \sin(\theta_0)\cos(\phi_0) = \frac{k_{x,avg}(\phi_{in})}{k_0} - \frac{m2\pi}{\Lambda k_0}$ and $u_{y,0} = \sin(\theta_0)\sin(\phi_0) = n_2 sin(\phi_{in})$ to find:

$$\begin{aligned}
\left[\cos(\phi_{in})\right]^2 + \left[\sin(\phi_{in})\right]^2 &= 1 \\
\left[\frac{n_{eff}k_0\cos(\phi_{in})}{n_{eff}k_0} - \frac{m\lambda}{n_{eff}\Lambda} + \frac{m\lambda}{n_{eff}\Lambda}\right]^2 + \left[\frac{n_2\sin(\phi_{in})}{n_2}\right]^2 &= 1 \\
\left[\frac{u_{x,0} + \frac{m\lambda}{\Lambda}}{n_{eff}}\right]^2 + \left[\frac{u_{y,0}}{n_2}\right]^2 &= 1
\end{aligned} \tag{A.6}$$

This is an ellipse centered at $[-\frac{m\lambda}{\Lambda}, 0]$. As ϕ_{in} is varied, the emission direction will traverse an arc of this ellipse in u_x, u_y space. Tuning the wavelength λ will translate this ellipse forward and backward in the u_x direction. The total field-of-view in u_x, u_y space will have the form of a curved band whose thickness will be controlled by the total wavelength tuning range. We discuss the number of 3dB overlapped beams we can fit inside this field-of-view in the Number of Resolvable Points section.

A.2 Directivity Calculation

The far-field beam of the device is formed when the beam collimated by the lens propagates across the diffraction grating. Given the grating pitch Λ, the aperture width W, and relevant refractive indices, the far-field power and directivity of the device is calculated as a function of different wavelengths and incident angles from the planar lens. We begin by establishing the geometry of the aperture. The aperture is a parallelogram shaped region of the grating across which the wave from the lens propagates. The width of this beam is taken to be W, and the effective length is taken to be L. The inclination of the parallelogram is determined by the grating propagation angle (ϕ') and is equal to $\arctan\left(\frac{n_2\sin(\phi_{in})k_0}{k_{x,avg}}\right) \approx \arctan\left(\frac{n_2\sin(\phi_{in})}{n_{eff}\cos(\phi_{in})}\right)$ and is close in magnitude to ϕ_{in}, but not identical because of the refraction at the grating steps. The geometry of the aperture is then bounded by the conditions where $\tan(\phi')$ is the slope of the shear. :

$$0 \le x \le L, \;\; -\frac{W}{2} + x\tan\phi' \le y \le \frac{W}{2} + x\tan\phi' \tag{A.7}$$

To model the effect of attenuation as light propagates through the grating, the near field distribution is assumed to decay exponentially in the propagation direction as e^{-qx}. The exact value of the grating length L used in the calculation is inconsequential, provided that $L \gg 1/q$, ensuring that the majority of the field has been attenuated into the far-field after propagation to the end-point L. With this consideration, the near field $A(x, y)$ takes the form

$$A(x, y) = e^{-qx} e^{ik_0 u_{x0} x} e^{ik_0 u_{y0} y} \tag{A.8}$$

where k_0 is the wavevector magnitude, $(u_{x0}, u_{y0}) = (\sin\theta_0 \cos\phi_0, \sin\theta_0 \sin\phi_0)$ are direction cosines, ϕ_0 is the in-plane angle, and θ_0 is the out of plane angle.

To obtain the far-field $F(u_x - u_{x0}, u_y - u_{y0})$, we take the Fourier transform of the near field over the aperture region.

$$\begin{aligned} F(u_x - u_{x0}, u_y - u_{y0}) &= \int_0^L dx \int_{-W/2 + x\tan\phi'}^{W/2 + x\tan\phi'} dy\, A(x, y) e^{-ik_0 u_x x} e^{-ik_0 u_y y} \\ &= -\frac{1}{ik_0 \Delta u_y} \int_0^L dx\, e^{-qx} e^{-ik_0 \Delta u_x x} \\ &\quad \cdot \left(e^{-ik_0 \Delta u_y (W/2 + x\tan\phi')} - e^{-ik_0 \Delta u_y (-W/2 + x\tan\phi')} \right) \end{aligned} \tag{A.9}$$

where we have used the shorthand $(\Delta u_x, \Delta u_y) \equiv (u_x - u_{x0}, u_y - u_{y0})$. Similarly, performing the x integral gives

$$\begin{aligned} F(\Delta u_x, \Delta u_y) &= \frac{-1}{ik_0 \Delta u_y} \left(e^{-ik_0 \Delta u_y W/2} - e^{+ik_0 \Delta u_y W/2} \right) \int_0^L dx\, e^{-qx} e^{-ik_0 \Delta u_x x} e^{-ik_0 \Delta u_y \tan\phi' x} \\ &= \frac{2\sin(k_0 \Delta u_y W/2)}{k_0 \Delta u_y} \cdot \frac{1 - e^{-qL} e^{-ik_0 (\Delta u_x + \Delta u_y \tan\phi')L}}{q + ik_0 (\Delta u_x + \Delta u_y \tan\phi')} \end{aligned} \tag{A.10}$$

Assuming that all power from the grating is emitted into the upper hemisphere, the directivity $D(\theta, \phi)$ is defined as

$$D(\theta, \phi) = \frac{P(\theta, \phi)}{\frac{1}{2\pi} \int_0^{\pi/2} d\theta\, \sin\theta \int_0^{2\pi} d\phi\, P(\theta, \phi)} \tag{A.11}$$

We now switch to coordinates which center the angular directivity distribution around the peak power output. Assume that the far field spectrum has peak gain at (θ_0, ϕ_0). The coordinates we use are then the coordinates which represent deviation from the max, which we will denote $(\Delta\theta, \Delta\phi)$. Considering this approximation, we can then write

$$D(\Delta\theta, \Delta\phi) \approx \frac{P(\Delta\theta, \Delta\phi)}{\frac{\sin\theta_0}{2\pi}\int_{-\infty}^{\infty} d\Delta\phi \int_{-\infty}^{\infty} d\Delta\theta\, P(\Delta\theta, \Delta\phi)} \tag{A.12}$$

where we have also extended the limits of angular integration to infinity, which is justified since the directivities we consider are sharply peaked about the max, and then decay rapidly. We then make the coordinate transformation $(\Delta\theta, \Delta\phi) \to (\Delta u_x, \Delta u_y)$, which is explicitly given as

$$\begin{aligned} \Delta u_x &= \cos\theta_0 \sin\phi_0 \Delta\theta + \sin\theta_0 \cos\phi_0 \Delta\phi = u_x - u_{x0} \\ \Delta u_y &= \cos\theta_0 \cos\phi_0 \Delta\theta + \sin\theta_0 \sin\phi_0 \Delta\phi = u_y - u_{y0} \end{aligned} \tag{A.13}$$

Taking the Jacobian then gives the differential transformation
$d\Delta\theta d\Delta\phi \sin\theta_0 = d\Delta u_x d\Delta u_y / \cos\theta_0$. Thus the gain about the peak can be written as

$$D(\Delta u_x, \Delta u_y) = \frac{2\pi \cos\theta_0 P(\Delta u_x, \Delta u_y)}{\int_{-\infty}^{\infty} d\Delta u_x \int_{-\infty}^{\infty} d\Delta u_y P(\Delta u_x, \Delta u_y)} \tag{A.14}$$

The far-field power $P = |F|^2$ is then computed as

$$\begin{aligned} P = |F|^2 &= \left(\frac{2\sin(k_0 \Delta u_y W/2)}{k_0 \Delta u_y}\right)^2 \left|\frac{1 - e^{-qL} e^{-ik_0(\Delta u_x + \Delta u_y \tan\phi')L}}{q + ik_0(\Delta u_x + \Delta u_y \tan\phi')}\right|^2 \\ &= \frac{4\sin^2(k_0 \Delta u_y W/2)}{(k_0 \Delta u_y)^2} \cdot \frac{1}{q^2 + k_0^2(\Delta u_x + \Delta u_y \tan\phi')^2} \\ &\quad \cdot \left(1 + e^{-2qL} - 2e^{-qL}\cos\left(k_0 L(\Delta u_x + \Delta u_y \tan\phi')\right)\right) \\ &= \frac{W^2 \mathrm{sinc}^2(k_0 \Delta u_y W/2)}{q^2 + k_0^2(\Delta u_x + \Delta u_y \tan\phi')^2} \cdot \left(1 + e^{-2qL} - 2e^{-qL}\cos\left(k_0 L(\Delta u_x + \Delta u_y \tan\phi')\right)\right) \end{aligned} \tag{A.15}$$

where in the last step we have converted the sine function to a sinc using
$\mathrm{sinc}(k_0 \Delta u_y W/2) = \sin(k_0 \Delta u_y W/2)/(k_0 \Delta u_y W/2)$. The directivity normalization fac-

tor is given by

$$\int_{-\infty}^{\infty} d\Delta u_x \int_{-\infty}^{\infty} d\Delta u_y P(\Delta u_x, \Delta u_y) = \int_{-\infty}^{\infty} d\Delta u_x \int_{-\infty}^{\infty} d\Delta u_y \frac{\mathrm{sinc}^2(W k_0 \Delta u_y/2)}{1 + \frac{k_0^2}{q^2}(\Delta u_x + \Delta u_y \tan\phi')^2} \frac{W^2}{q^2} \cdot \left(1 + e^{-2qL} - 2e^{-qL}\cos\left(k_0 L(\Delta u_x + \Delta u_y \tan\phi')\right)\right) \tag{A.16}$$

To evaluate this, we perform the change of variables

$$\begin{aligned} x &= \frac{k_0}{q}(\Delta u_x + \tan\phi' \Delta u_y) \\ y &= \frac{W k_0}{2} \Delta u_y \end{aligned} \tag{A.17}$$

The Jacobian of this transformation is then $2q/Wk_0^2$, and after the change of variables, the integral is expressed as

$$\begin{aligned} \int_{-\infty}^{\infty} d\Delta u_x \int_{-\infty}^{\infty} d\Delta u_y P(\Delta u_x, \Delta u_y) &= \frac{2q}{W k_0^2} \int_{-\infty}^{\infty} dx \left(\frac{1 + e^{-2qL}}{1 + x^2} - \frac{2\cos(qLx)e^{-qL}}{1 + x^2}\right) \\ &\quad \cdot \int_{-\infty}^{\infty} dy\, \mathrm{sinc}^2(y) \frac{W^2}{q^2} \\ &= \frac{2W}{q k_0^2}\left(\pi(1 + e^{-2qL}) - 2e^{-2qL}\right)\pi \\ &= \frac{2W}{q k_0^2}\pi^2(1 - e^{-2qL}) \end{aligned} \tag{A.18}$$

where we have made use of the integrals $\int_{-\infty}^{\infty} dx/(1+x^2) = \pi$, $\int_{-\infty}^{\infty} dx\, \cos(qLx)/(1+x^2) = \pi e^{-qL}$, and $\int_{-\infty}^{\infty} \mathrm{sinc}^2(y)\, dy = \pi$.

Assembling the final expression for the directivity, we have

$$\begin{aligned} D(\Delta u_x, \Delta u_y) &= \frac{2\pi \cos\theta_0 P(\Delta u_x, \Delta u_y)}{\iint P(\Delta u_x, \Delta u_y)} \\ &= 2\pi \cos\theta_0 \cdot \frac{W^2}{q^2} \frac{\operatorname{sinc}^2(W k_0 \Delta u_y/2)}{1 + \frac{k_0^2}{q^2}(\Delta u_x + \Delta u_y \tan\phi')^2} \\ &\quad \cdot \frac{(1 - 2\cos(k_0 L(\Delta u_x + \Delta u_y \tan\phi'))e^{-qL} + e^{-2qL})}{\frac{2W\pi^2}{q k_0^2}(1 - e^{-2qL})} \\ &= \frac{W k_0^2 \cos\theta_0}{\pi q(1 - e^{-2qL})} \cdot \frac{\operatorname{sinc}^2(k_0 \Delta u_y W/2)}{1 + \frac{k_0^2}{q^2}\left(\Delta u_x + \Delta u_y \tan\phi'\right)^2} \\ &\quad \cdot (1 - 2\cos(k_0 L(\Delta u_x + \Delta u_y \tan\phi'))e^{-qL} + e^{-2qL}) \end{aligned} \tag{A.19}$$

The maximum directivity is given as

$$D_{\max} = D(0,0) = \cos\theta_0 \frac{W k_0^2}{\pi q} \frac{(1 - e^{-qL})^2}{(1 - e^{-2qL})} \tag{A.20}$$

To improve the analytical insight from these expressions, we consider two opposing limiting cases: $L \ll 1/q$ and $L \gg 1/q$:

1. For $L \ll \frac{1}{q}$, using the substitutions $u = k_0 L(\Delta u_x + \tan(\phi')\Delta u_y)$, $\beta = \frac{W}{2} k_0 \Delta u_y$, and L'Hopital's Rule we obtain:

$$\lim_{qL \to 0} D(\Delta u_x, \Delta u_y) = \frac{LW k_0^2 \cos\theta_0}{L\pi q(1 - e^{-2qL})} \frac{\operatorname{sinc}^2(\beta)}{1 + \left(\frac{u}{qL}\right)^2} \cdot (1 - 2\cos(u)e^{-qL} + e^{-2qL}) \tag{A.21}$$

$$= \frac{LW k_0^2 \cos\theta_0}{2\pi} \operatorname{sinc}^2(\beta) \operatorname{sinc}^2(u/2) \tag{A.22}$$

$$= \frac{LW k_0^2 \cos\theta_0}{2\pi} \operatorname{sinc}^2\left(\frac{W}{2} k_0 \Delta u_y\right) \operatorname{sinc}^2\left(\frac{k_0 L}{2}(\Delta u_x + \tan(\phi')\Delta u_y)\right) \tag{A.23}$$

   This is just the directivity from a sheared rectangular aperture of length L and width W, note that the peak gain is $\frac{LW k_0^2 \cos(\theta_0)}{2\pi}$, which is directly proportional to the projected area $LW\cos(\theta_0)$.

2. Taking the opposite limit, $L \gg \frac{1}{q}$, we find:

$$\lim_{qL\to\infty} D(\Delta u_x, \Delta u_y) = \frac{W k_0^2 \cos(\theta_0)}{q\pi} \frac{\operatorname{sinc}^2(\frac{W}{2} k_0 \Delta u_y)}{1 + \frac{k_0^2}{q^2}(\Delta u_x + \tan(\phi')\Delta u_y)^2} \tag{A.24}$$

Here the peak directivity scales as $\frac{W}{q}\cos(\theta_0)$, where $\frac{1}{q}$ becomes the effective length of the aperture. Even if the aperture is several decay lengths long, the effect of the finite length of the directivity is significant and properly modeling it requires the full expression. An example of this is in computing the number of far-field resolvable points.

A.3 Number of Resolvable Points

A.3.1 Horizontal

The number of resolvable points in-plane can be estimated by dividing the expected horizontal field of view (FOV) $\Delta\theta_h$ by the divergence of the outgoing beam. Assuming a uniformly lit aperture of size W (i.e., the size of the lens), the angle of the first minimum of the outgoing beam in the far-field is approximately $\theta_{\min} \approx 1.22\frac{\lambda}{W}$. We can assume this to be the minimum resolvable angle through the Rayleigh criterion. Thus, the in-plane number of resolvable points is

$$N_{\text{horizontal}} \approx \frac{W\Delta\theta_h}{1.22\lambda} \tag{A.25}$$

With the parameters $\lambda = 1.55\,\mu\text{m}$, $W = 100\,\mu\text{m}$, and $\Delta\theta_h = 40°$, we get 37 resolvable points. This means that the system would need to be scaled up to centimeter-sized apertures to hit thousands of resolvable points for a camera-like image.

A.3.2 Vertical

We shall take the same approach as in Section A.3.1 to derive the number of resolvable points in the vertical direction by dividing the total vertical range by the expected

vertical resolution from the grating. We will look at these quantities as a function of both the x-component of the unit wavevector $u_x = \sin\theta$ and the angle θ as they offer different insights into the problem.

The total FOV in the vertical direction can be estimated by the bandwidth of the laser $\Delta\lambda = \lambda_1 - \lambda_2$ and the grating equation

$$\Lambda = \frac{m\lambda}{n_{\text{eff}} - \sin\theta} \tag{A.26}$$

where n_{eff} is the averaged effective index of the grating, m is the diffraction order, and Λ is the grating period. Taking just the first diffraction order such that $m = 1$, we have the total range:

$$\Delta u_x = \frac{\Delta\lambda}{\Lambda} \tag{A.27}$$

$$\Delta\theta = \arcsin\left(n_{\text{eff}} - \frac{\lambda_1}{\Lambda}\right) - \arcsin\left(n_{\text{eff}} - \frac{\lambda_2}{\Lambda}\right) \tag{A.28}$$

While Equation A.28 unfortunately does not have a simple linear dependence on $\Delta\lambda$, it can be easily calculated numerically from the physical parameters of the grating and is more practical for systems analysis.

While we have derived a full expression for the 2-D directivity in Section A.2, we shall assume a 1D grating (which can be interpreted as a cross-section of our full 2-D grating) for simplicity. The near-field for a grating that emits at angle θ_0 is given by:

$$f(x) = e^{-qx}e^{ik_0 \sin\theta_0 x} \tag{A.29}$$

where q is the decay constant of the near-field along the grating (which is related to the scattering strength of the grating) and $k_0 = \frac{2\pi}{\lambda}$ is the wavenumber in the background medium. We ignore multiplicative constant factors as these do not affect the beam-width in the far-field. Taking the Fourier transform gives us the far-field of

the grating as a function of the wavenumber $k = k_0 \sin\theta$:

$$F(k) = \frac{1}{2\pi(q + i(k - k_0 \sin\theta_0))} \tag{A.30}$$

which we can take the squared magnitude to get the far-field intensity:

$$S(k) = \frac{1}{(2\pi)^2(q^2 + (k - k_0 \sin\theta_0)^2)} \tag{A.31}$$

Note that this is a Lorentzian function, which has a simple, analytical expression for the full-width half-max (FWHM). However, Equation A.31 is a Lorentzian as a function of k whereas we wish to find the FWHM in terms of θ. Thus, reparameterizing the far-field intensity gives us:

$$S(\theta) = \frac{\frac{1}{k_0}}{(2\pi)^2((\frac{q}{k_0})^2 + (\sin\theta - \sin\theta_0)^2)} \tag{A.32}$$

As expected, we can see that the peak of the far-field intensity occurs at $\theta = \theta_0$. We can see from the Lorentzian form that the FWHM as a function of $u_x = \sin\theta$ is

$$\Delta u_{x,\mathrm{FWHM}} = \Delta \sin\theta_{\mathrm{FWHM}} = \frac{2q}{k_0} \tag{A.33}$$

Combining Equations A.27 and A.33 gives us a simple analytical form for the number of resolvable points in the vertical direction:

$$N_{\mathrm{vertical}} = \frac{\Delta\lambda k_0}{2\Lambda q} \tag{A.34}$$

We see that the number of resolvable points is proportional to the wavelength range of the laser, as expected. Additionally, we see that strategies to increase the number of resolvable points is by either decreasing Λ (which pushes the beam closer to the normal angle) or by decreasing q (which leads to a larger effective aperture.

To get a better intuition for the angular resolution, we can rearrange Equation

A.33 to get an expression for the angular FWHM:

$$u_{x,\text{FWHM}\pm} = \sin\theta_{\text{FWHM}\pm} = \sin\theta_0 \pm \frac{q}{k_0} \tag{A.35}$$

$$\Delta\theta = \theta_{\text{FWHM+}} - \theta_{\text{FWHM-}} = \arcsin\left(\sin\theta_0 + \frac{q}{k_0}\right) - \arcsin\left(\sin\theta_0 - \frac{q}{k_0}\right) \tag{A.36}$$

Equation A.36 is a closed-form analytical expression for the FWHM, which can then be used to calculate the number of resolvable points. To gain further intuition, we shall make approximations by assuming that $\frac{q}{k_0} = \frac{\lambda}{\pi\beta}$ (where $\beta = \frac{1}{q}$ is the effective length of the grating aperture) is a small quantity, allowing us to take the Taylor expansion of the arcsin term around $\sin\theta_0$.

$$\Delta\theta_{\text{FWHM}} \approx \left(\arcsin(\sin\theta_0) + \frac{q}{k_0\sqrt{1-\sin^2\theta_0}}\right) - \left(\arcsin(\sin\theta_0) - \frac{q}{k_0\sqrt{1-\sin^2\theta_0}}\right) \tag{A.37}$$

$$= \frac{2q}{k_0\cos\theta_0} \tag{A.38}$$

$$= \frac{\lambda}{\pi\beta\cos\theta_0} \tag{A.39}$$

Equation A.39 is approximately the same FWHM as a uniform aperture of size $\pi\beta$ with a $\cos\theta_0$ term to correct for the effective aperture at off-normal incident angles. We can also see that the assumption of a small $\frac{q}{k_0}$ term is equivalent to the assumption of a small $\Delta\theta_{\text{FWHM}}$, which we would expect in practice for realistic long-range optical beam steering systems.

A.4 Index Error

We now consider how changes in the refractive index impact the focusing ability of the planar lens. The effective index ratio $n = n_1/n_2$ of the fabricated device will differ from the desired index due to factors such as fabrication tolerances, wavelength dispersion, and temperature variations. A thick spherical lens with thickness d and radii of curvature R_1 and R_2 can be described by the lensmaker's equation. In particular,

we take the limit of $R_2 \to \infty$ to look at the case of a plano-convex lens and take the derivative with respect to n to see the sensitivity of the lens to index variations Δn.

$$\begin{aligned}
\frac{1}{f} &= \frac{(n-1)}{R_1} - \frac{(n-1)}{R_2} + \frac{(n-1)d}{nR_1R_2} \\
\frac{\partial}{\partial n}\left[\lim_{R_2\to\infty}\left(\frac{1}{f}\right)\right] &= \frac{\partial}{\partial n}\left[\lim_{R_2\to\infty}\left(\frac{(n-1)}{R_1} - \frac{(n-1)}{R_2} + \frac{(n-1)d}{nR_1R_2}\right)\right] \\
-f^{-2}\frac{\partial f}{\partial n} &= \frac{1}{R_1}
\end{aligned}$$

Dropping the negative sign for convenience (since we just care about magnitudes of sensitivity), we linearize the relation:

$$\Delta f = \frac{f^2}{R_1}\Delta n \tag{A.40}$$

Here Δf can be interpreted as the depth of focus, which is defined as

$$\Delta f = \frac{4\lambda f^2}{D^2} \tag{A.41}$$

for a telescope, where W is the lens aperture. The lensmaker's equation for a plano-convex lens gives us $R_1 \approx f$. Assuming a fixed field-of-view and an angular resolution limit that can be approximated as $\theta \approx \lambda/W$, we have the relation $N \approx W/\lambda$ where N is the number of resolvable points. Thus, plugging in these relations into Equation A.40, the effective index tolerance Δn is:

$$\Delta n = \frac{4\lambda f^2}{W^2}\frac{f}{f^2} \tag{A.42}$$

$$= \frac{4\lambda f}{W^2} \tag{A.43}$$

$$= \frac{4\lambda F\#}{W} \tag{A.44}$$

$$= \frac{4f}{DN} \tag{A.45}$$

where $F\# = f/W$ is the F-number of the lens. Equations A.43, A.44, and A.45 are different interpretations of the same relation with various factors made explicit.

From this analysis, we can see challenges with scaling up the lens to a realistic system. First, the effective index tolerance scales inversely with N, which is problematic as realistic imaging systems may require thousands of resolvable points. Second, the effective index tolerance also scales inversely with W, which corresponds to a more collimated beam on the transmit side and more light collection (and thus a larger signal for detection) on the receive side. Strategies to abate these challenges include introducing a form of active tuning that can adjust the realized index in a feedback loop, or designing a lens with a larger F-number.

Bibliography

[1] Jingwen He, Tao Dong, and Yue Xu. Review of Photonic Integrated Optical Phased Arrays for Space Optical Communication. *IEEE Access*, 8:188284–188298, 2020. Conference Name: IEEE Access.

[2] C. V. Poulton, M. J. Byrd, P. Russo, E. Timurdogan, M. Khandaker, D. Vermeulen, and M. R. Watts. Long-Range LiDAR and Free-Space Data Communication With High-Performance Optical Phased Arrays. *IEEE Journal of Selected Topics in Quantum Electronics*, 25(5):1–8, September 2019.

[3] Ching-Pai Hsu, Boda Li, Braulio Solano-Rivas, Amar R. Gohil, Pak Hung Chan, Andrew D. Moore, and Valentina Donzella. A Review and Perspective on Optical Phased Array for Automotive LiDAR. *IEEE Journal of Selected Topics in Quantum Electronics*, 27(1):1–16, January 2021.

[4] Ying Li, Lingfei Ma, Zilong Zhong, Fei Liu, Dongpu Cao, Jonathan Li, and Michael A. Chapman. Deep Learning for LiDAR Point Clouds in Autonomous Driving: A Review. *arXiv:2005.09830 [cs]*, May 2020. arXiv: 2005.09830.

[5] Jonathan K. Doylend and Sanjeev Gupta. An overview of silicon photonics for LIDAR. In Graham T. Reed and Andrew P. Knights, editors, *Silicon Photonics XV*, page 17, San Francisco, United States, February 2020. SPIE.

[6] Christopher V. Poulton, Ami Yaacobi, Zhan Su, Matthew J. Byrd, and Michael R. Watts. Optical Phased Array with Small Spot Size, High Steering Range and Grouped Cascaded Phase Shifters. In *Advanced Photonics 2016 (IPR, NOMA, Sensors, Networks, SPPCom, SOF) (2016), paper IW1B.2*, page IW1B.2. Optical Society of America, July 2016.

[7] Taehwan Kim. *Realization of Integrated Coherent LiDAR*. PhD thesis, UC Berkeley, 2019.

[8] Customer Discovery Interview for Lidar Sensors: Conversations w/ Automotive Experts, 2020.

[9] Ross, Philip E. Lumotive Says It's Got a Solid-State Lidar That Really Works, March 2019. Section: Transportation.

[10] Dingkang Wang, Connor Watkins, and Huikai Xie. MEMS Mirrors for LiDAR: A Review. *Micromachines*, 11(5):456, April 2020.

[11] Ross, Philip E. Velodyne Will Sell a Lidar for $100 - IEEE Spectrum, 2020.

[12] Near Margalit, Chao Xiang, Steven M. Bowers, Alexis Bjorlin, Robert Blum, and John E. Bowers. Perspective on the future of silicon photonics and electronics. *Applied Physics Letters*, 118(22):220501, May 2021. Publisher: American Institute of Physics.

[13] Ramsey Selim, Romano Hoofman, Mulham Khoder, Adil Masood, Callum Littlejohns, Douwe Geuzebroek, Robert Grootjans, Thomas Drischel, and Kholdoun Torki. Silicon photonics open access foundry services review for emerging technology. In *Emerging Applications in Silicon Photonics II*, volume 11880, pages 15–23. SPIE, December 2021.

[14] S. Y. Siew, B. Li, F. Gao, H. Y. Zheng, W. Zhang, P. Guo, S. W. Xie, A. Song, B. Dong, L. W. Luo, C. Li, X. Luo, and G.-Q. Lo. Review of Silicon Photonics Technology and Platform Development. *Journal of Lightwave Technology*, 39(13):4374–4389, July 2021. Publisher: IEEE.

[15] Cheryl Sorace-Agaskar, Dave Kharas, Siva Yegnanarayanan, Ryan T. Maxson, Gavin N. West, William Loh, Suraj Bramhavar, Rajeev J. Ram, John Chiaverini, Jeremy Sage, and Paul Juodawlkis. Versatile Silicon Nitride and Alumina Integrated Photonic Platforms for the Ultraviolet to Short-Wave Infrared. *IEEE Journal of Selected Topics in Quantum Electronics*, 25(5):1–15, September 2019.

[16] Sven T. S. Holmström, Utku Baran, and Hakan Urey. MEMS Laser Scanners: A Review. *Journal of Microelectromechanical Systems*, 23(2):259–275, April 2014.

[17] Han Woong Yoo, Norbert Druml, David Brunner, Christian Schwarzl, Thomas Thurner, Marcus Hennecke, and Georg Schitter. MEMS-based lidar for autonomous driving. *e & i Elektrotechnik und Informationstechnik*, 135(6):408–415, October 2018.

[18] Gleb M. Akselrod, Yuanmu Yang, and Patrick Bowen. Tunable liquid crystal metasurfaces, September 2020.

[19] Gleb M. Akselrod. Waveguide-integrated tunable liquid crystal metasurface devices, November 2020.

[20] Karel Van Acoleyen, Wim Bogaerts, Jana Jágerská, Nicolas Le Thomas, Romuald Houdré, and Roel Baets. Off-chip beam steering with a one-dimensional optical phased array on silicon-on-insulator. *Optics Letters*, 34(9):1477–1479, May 2009. Publisher: Optical Society of America.

[21] SungWon Chung, Hooman Abediasl, and Hossein Hashemi. A Monolithically Integrated Large-Scale Optical Phased Array in Silicon-on-Insulator CMOS. *IEEE Journal of Solid-State Circuits*, 53(1):275–296, January 2018. Conference Name: IEEE Journal of Solid-State Circuits.

[22] David N. Hutchison, Jie Sun, Jonathan K. Doylend, Ranjeet Kumar, John Heck, Woosung Kim, Christopher T. Phare, Avi Feshali, and Haisheng Rong. High-resolution aliasing-free optical beam steering. *Optica*, 3(8):887–890, August 2016.

[23] Tin Komljenovic, Roger Helkey, Larry Coldren, and John E Bowers. Sparse aperiodic arrays for optical beam forming and lidar. *Optics Express*, 25(3):2511–2528, 2017.

[24] Christopher T. Phare, Christopher T. Phare, Min Chul Shin, Jahnavi Sharma, Sohail Ahasan, Harish Krishnaswamy, and Michal Lipson. Silicon Optical Phased Array with Grating Lobe-Free Beam Formation Over 180 Degree Field of View. In *Conference on Lasers and Electro-Optics (2018), paper SM3I.2*, page SM3I.2. Optical Society of America, May 2018.

[25] Josue J Lopez. MIT Spinoff Building New Solid-State Lidar-on-a-Chip System, December 2020. Section: Semiconductors.

[26] W. Rotman and R. Turner. Wide-angle microwave lens for line source applications. *IEEE Transactions on Antennas and Propagation*, 11(6):623–632, November 1963.

[27] Jar Jueh Lee. Lens Antennas. In Y. T. Lo and S. W. Lee, editors, *Antenna Handbook: Theory, Applications, and Design*, pages 1073–1131. Springer US, Boston, MA, 1988.

[28] Samuel Silver and Institution of Electrical Engineers. *Microwave Antenna Theory and Design*. IET, 1984. Google-Books-ID: Aex6dlKreHEC.

[29] Scott Alexander Skirlo. *Photonics for technology : circuits, chip-scale LIDAR, and optical neural networks*. Thesis, Massachusetts Institute of Technology, 2017.

[30] Samuel Kim, Jamison Sloan, Josué J. López, Dave Kharas, Jeffrey Herd, Suraj Bramhavar, Paul Juodawlkis, George Barbastathis, Steven Johnson, Cheryl Sorace-Agaskar, and Marin Soljačić. Luneburg Lens for Wide-Angle Chip-Scale Optical Beam Steering. In *Conference on Lasers and Electro-Optics (2019), paper SF3N.7*, page SF3N.7. Optical Society of America, May 2019.

[31] Jie Sun, Erman Timurdogan, Ami Yaacobi, Ehsan Shah Hosseini, and Michael R Watts. Large-scale nanophotonic phased array. *Nature*, 493(7431):195–199, 2013.

[32] J. C. Hulme, J. K. Doylend, M. J. R. Heck, J. D. Peters, M. L. Davenport, J. T. Bovington, L. A. Coldren, and J. E. Bowers. Fully integrated hybrid silicon two dimensional beam scanner. *Optics Express*, 23(5):5861, March 2015.

[33] Steven A. Miller, You-Chia Chang, Christopher T. Phare, Min Chul Shin, Moshe Zadka, Samantha P. Roberts, Brian Stern, Xingchen Ji, Aseema Mohanty, Oscar A. Jimenez Gordillo, Utsav D. Dave, and Michal Lipson. Large-scale optical phased array using a low-power multi-pass silicon photonic platform. *Optica*, 7(1):3–6, January 2020. Publisher: Optical Society of America.

[34] Haiyang Zhang, Zixuan Zhang, Chao Peng, and Weiwei Hu. Phase Calibration of On-Chip Optical Phased Arrays via Interference Technique. *IEEE Photonics Journal*, 12(2):1–10, April 2020. Conference Name: IEEE Photonics Journal.

[35] Min Tan, Kaixuan Ye, Da Ming, Yuhang Wang, Zhicheng Wang, Li Jin, and Junbo Feng. Towards electronic-photonic-converged thermo-optic feedback tuning. 42(2):023104, February 2021. Publisher: IOP Publishing.

[36] John Ruze. Wide-angle metal-plate optics. *Proceedings of the IRE*, 38(1):53–59, 1950.

[37] Ann Lee Peebles. A dielectric bifocal lens for multibeam antenna applications. *IEEE Transactions on Antennas and Propagation*, 36(5):599–606, 1988.

[38] Bernhard Schoenlinner, Xidong Wu, Jim P Ebling, George V Eleftheriades, and Gabriel M Rebeiz. Wide-scan spherical-lens antennas for automotive radars. *IEEE Transactions on microwave theory and techniques*, 50(9):2166–2175, 2002.

[39] Joerg Schoebel and Pablo Herrero. *Planar antenna technology for mm-wave automotive radar, sensing, and communications*. INTECH Open Access Publisher, 2010.

[40] Yousuke Tajima and Yoshihide Yamada. Design of shaped dielectric lens antenna for wide angle beam steering. *Electronics and Communications in Japan (Part III: Fundamental Electronic Science)*, 89(2):1–12, 2006.

[41] Yuen T Lo and SW Lee. *Antenna Handbook: theory, applications, and design*. Springer Science & Business Media, 2013.

[42] Masud Mansuripur. Abbe's Sine Condition. *Optics and Photonics News*, 9(2):56, February 1998.

[43] Josué J. López, Scott A. Skirlo, Dave Kharas, Jamison Sloan, Jeffrey Herd, Paul Juodawlkis, Marin Soljačić, and Cheryl Sorace-Agaskar. Planar-lens Enabled Beam Steering for Chip-scale LIDAR. In *Conference on Lasers and Electro-Optics (2018), paper SM3I.1*, page SM3I.1. Optical Society of America, May 2018.

[44] D. T. Pierce and W. E. Spicer. Electronic Structure of Amorphous Si from Photoemission and Optical Studies. *Physical Review B*, 5(8):3017–3029, April 1972. Publisher: American Physical Society.

[45] Kevin Luke, Yoshitomo Okawachi, Michael R. E. Lamont, Alexander L. Gaeta, and Michal Lipson. Broadband mid-infrared frequency comb generation in a Si_3N_4 microresonator. *Optics Letters*, 40(21):4823–4826, November 2015. Publisher: Optica Publishing Group.

[46] Young-Jin Park and Werner Wiesbeck. Offset cylindrical reflector antenna fed by a parallel-plate luneburg lens for automotive radar applications in millimeter-wave. *IEEE Transactions on Antennas and Propagation*, 51(9):2481–2483, 2003.

[47] John Sanford. A luneberg-lens update. *IEEE Antennas and Propagation Magazine*, 37(1):76–79, 1995.

[48] J Rao. Multifocal three-dimensional bootlace lenses. *IEEE Transactions on Antennas and Propagation*, 30(6):1050–1056, 1982.

[49] FG Friedlander. A dielectric-lens aerial for wide-angle beam scanning. *Journal of the Institution of Electrical Engineers-Part IIIA: Radiolocation*, 93(4):658–662, 1946.

[50] R Ulrich and RJ Martin. Geometrical optics in thin film light guides. *Applied Optics*, 10(9):2077–2085, 1971.

[51] Shogo Ura, Toshiaki Suhara, Hiroshi Nishihara, and Jiro Koyama. An integrated-optic disk pickup device. *Journal of lightwave technology*, 4(7):913–918, 1986.

[52] David K. How do I compute the solid angle of a square in space in spherical coordinates?, January 2020.

[53] Gero Nootz. Fit 2D gaussian function to data, 2021. MATLAB Central File Exchange.

[54] Manuel A. Diaz. Fit 1D and 2D gaussian to noisy data, 2021. MATLAB Central File Exchange.

[55] Eric W. Weisstein. Gaussian Function, 2021. Publisher: Wolfram Research, Inc.

[56] J Komma, C Schwarz, G Hofmann, D Heinert, and R Nawrodt. Thermo-optic coefficient of silicon at 1550 nm and cryogenic temperatures. *Applied Physics Letters*, 101(4):041905, 2012.

[57] Amir Arbabi and Lynford L Goddard. Measurements of the refractive indices and thermo-optic coefficients of si 3 n 4 and sio x using microring resonances. *Optics letters*, 38(19):3878–3881, 2013.

[58] Hani Nejadriahi, Alex Friedman, Rajat Sharma, Steve Pappert, Yeshaiahu Fainman, and Paul Yu. Thermo-optic properties of silicon-rich silicon nitride for on-chip applications. *Optics Express*, 28(17):24951–24960, August 2020. Publisher: Optical Society of America.

[59] Alan D. Bristow, Nir Rotenberg, and Henry M. van Driel. Two-photon absorption and Kerr coefficients of silicon for 850–2200nm. *Applied Physics Letters*, 90(19):191104, May 2007.

[60] Christopher V Poulton, Matthew J Byrd, Manan Raval, Zhan Su, Nanxi Li, Erman Timurdogan, Douglas Coolbaugh, Diedrik Vermeulen, and Michael R Watts. Large-scale silicon nitride nanophotonic phased arrays at infrared and visible wavelengths. *Optics Letters*, 42(1):21–24, 2017.

[61] Freedom Photonics. Tunable Laser Products, 2022.

[62] Jörn P. Epping, Ruud M. Oldenbeuving, Dimitri Geskus, Ilka Visscher, Robert Grootjans, Chris G.H. Roeloffzen, and René G. Heideman. High power, tunable, narrow linewidth dual gain hybrid laser. In *Laser Congress 2019 (ASSL, LAC, LS&C)*, page ATu1A.4, Vienna, 2019. OSA.

[63] Yang Deng, Xi Wang, Zilun Gong, Kaichen Dong, Shuai Lou, Nicolas Pégard, Kyle B. Tom, Fuyi Yang, Zheng You, Laura Waller, and Jie Yao. All-Silicon Broadband Ultraviolet Metasurfaces. *Advanced Materials*, 30(38):1802632, September 2018.

[64] W. Bogaerts, P. De Heyn, T. Van Vaerenbergh, K. De Vos, S. Kumar Selvaraja, T. Claes, P. Dumon, P. Bienstman, D. Van Thourhout, and R. Baets. Silicon microring resonators. *Laser & Photonics Reviews*, 6(1):47–73, January 2012.

[65] Gavin N. West, William Loh, Dave Kharas, Cheryl Sorace-Agaskar, Karan K. Mehta, Jeremy Sage, John Chiaverini, and Rajeev J. Ram. Low-loss integrated photonics for the blue and ultraviolet regime. *APL Photonics*, 4(2):026101, February 2019. Publisher: American Institute of Physics.

[66] Far field projections in FDTD overview.

[67] Allen Taflove, Susan C. Hagness, and Melinda Piket-May. Computational Electromagnetics: The Finite-Difference Time-Domain Method. In *The Electrical Engineering Handbook*, pages 629–670. Elsevier, 2005.

[68] Varun Jain, Mark C. Biesinger, and Matthew R. Linford. The Gaussian-Lorentzian Sum, Product, and Convolution (Voigt) functions in the context of peak fitting X-ray photoelectron spectroscopy (XPS) narrow scans. *Applied Surface Science*, 447:548–553, July 2018.

[69] Wells, Jered. lorentzfit(x,y,varargin), June 2020.

[70] Lucas H Gabrielli and Michal Lipson. Integrated luneburg lens via ultra-strong index gradient on silicon. *Optics express*, 19(21):20122–20127, 2011.

[71] Andrea Di Falco, Susanne C Kehr, and Ulf Leonhardt. Luneburg lens in silicon photonics. *Optics express*, 19(6):5156–5162, 2011.

[72] Christopher Doerr, Li Chen, Long Chen, and Dinh Ton. Linear 2D Beam Steering with a Large Focusing Grating via Focal Point Movement and Wavelength. *IEEE Photonics Technology Letters*, pages 1–1, 2021. Conference Name: IEEE Photonics Technology Letters.

[73] R. K. Luneburg. University of California Press, 1964. Publication Title: Mathematical Theory of Optics Type: doi:10.1525/9780520328266.

[74] Borislav Vasić, Goran Isić, Radoš Gajić, and Kurt Hingerl. Controlling electromagnetic fields with graded photonic crystals in metamaterial regime. *Optics Express*, 18(19):20321–20333, September 2010.

[75] Andrea Di Falco, Susanne C. Kehr, and Ulf Leonhardt. Luneburg lens in silicon photonics. *Optics Express*, 19(6):5156–5162, March 2011.

[76] Hanhong Gao, Baile Zhang, Steven G. Johnson, and George Barbastathis. Design of thin–film photonic metamaterial Lüneburg lens using analytical approach. *Optics Express*, 20(2):1617–1628, January 2012.

[77] S. Takahashi, C. Chang, S. Y. Yang, and G. Barbastathis. Design and fabrication of dielectric nanostructured Luneburg lens in optical frequencies. In *2010 International Conference on Optical MEMS and Nanophotonics*, pages 179–180, August 2010.

[78] Samuel Kim and B A Physics. Design of a Photonic Crystal Planar Luneburg Lens for Optical Beam Steering. page 61, 2019.

[79] A. Mekis, S. Gloeckner, G. Masini, A. Narasimha, T. Pinguet, S. Sahni, and P. De Dobbelaere. A Grating-Coupler-Enabled CMOS Photonics Platform. *IEEE Journal of Selected Topics in Quantum Electronics*, 17(3):597–608, May 2011.

[80] Yunhong Ding, Haiyan Ou, and Christophe Peucheret. Ultrahigh-efficiency apodized grating coupler using fully etched photonic crystals. *Optics Letters*, 38(15):2732, August 2013.

[81] R. Halir, P. Cheben, J. H. Schmid, R. Ma, D. Bedard, S. Janz, D.-X. Xu, A. Densmore, J. Lapointe, and Í. Molina-Fernández. Continuously apodized fiber-to-chip surface grating coupler with refractive index engineered subwavelength structure. *Optics Letters*, 35(19):3243, October 2010.

[82] Manan Raval, Christopher V. Poulton, and Michael R. Watts. Unidirectional waveguide grating antennas with uniform emission for optical phased arrays. *Optics Letters*, 42(13):2563–2566, July 2017.

[83] Mingyan Fan, Miloš A. Popović, and Franz X. Kärtner. High Directivity, Vertical Fiber-to-Chip Coupler with Anisotropically Radiating Grating Teeth.

[84] Lukas Chrostowski and Michael Hochberg. *Silicon Photonics Design: From Devices to Systems*. Cambridge University Press, Cambridge, 2015.

[85] C.A. Flory. Analysis of directional grating-coupled radiation in waveguide structures. *IEEE Journal of Quantum Electronics*, 40(7):949–957, July 2004. Conference Name: IEEE Journal of Quantum Electronics.

[86] Ralf Waldhäusl, Bernd Schnabel, Peter Dannberg, Ernst-Bernhard Kley, Andreas Bräuer, and Wolfgang Karthe. Efficient Coupling into Polymer Waveguides by Gratings. *Applied Optics*, 36(36):9383–9390, December 1997. Publisher: Optica Publishing Group.

[87] Christopher Vincent Poulton. *Integrated LIDAR with optical phased arrays in silicon photonics*. Thesis, Massachusetts Institute of Technology, 2016. Accepted: 2017-08-01T13:02:33Z Journal Abbreviation: Integrated light detection and ranging with optical phased arrays in silicon photonic.

[88] Christopher Rogers, Alexander Y. Piggott, David J. Thomson, Robert F. Wiser, Ion E. Opris, Steven A. Fortune, Andrew J. Compston, Alexander Gondarenko, Fanfan Meng, Xia Chen, Graham T. Reed, and Remus Nicolaescu. A universal 3D imaging sensor on a silicon photonics platform. *Nature*, 590(7845):256–261, February 2021. Number: 7845 Publisher: Nature Publishing Group.